Kernel Based Model Parametrization and Adaptation with Applications to Battery Management Systems

by

Caihao Weng

A dissertation submitted in partial fulfillment
of the requirements for the degree of
Doctor of Philosophy
(Naval Architecture and Marine Engineering)
in The University of Michigan
2015

Doctoral Committee:

Professor Jing Sun, Co-Chair
Professor Huei Peng, Co-Chair
Associate Professor Ryan M. Eustice
Professor Anna G. Stefanopoulou

To my parents, for their unconditional love and support.

ACKNOWLEDGEMENTS

Even though people always say that time flies when you are having fun, it is hard to believe my life as a Ph.D. student has finally come to its end. It has been a truly tremendous experience and suddenly I realize how much I am going to miss Ann Arbor and the time I spent here. Without the help of many people, it would have not been possible for me to make it to this point.

I would first like to thank my advisors, Professors Jing Sun and Huei Peng, for their instructions and guidance as well as support and patience. It is a great honor and privilege for me to have the opportunity to learn from and work with them. They have been both great academic and life mentors for me. As Professor Sun often says, what she enjoys the most in mentoring students is to see one grows and becomes a more mature person. All her teachings are invaluable treasures to me and will always be remembered for the rest of my life. And, although Professor Peng often says his role as a co-advisor is to play the "bad cop", he has been incredibly encouraging and inspiring during my entire Ph.D. life. He always asks the critical questions from a bigger picture and leads my research into the right direction.

I would also like to thank my committee members, Professors Anna Stefanopoulou and Ryan Eustice. In addition to serving on my committee and giving me feedbacks, Professor Stefanopoulou's battery course was indeed the first building block of my research, and leaded me into this exciting and challenging area. Professor Eustice is one of the best teachers at Michigan, and I have always enjoyed his lectures.

I wish to extend my special thanks to Mr. Xunning Feng from Tsinghua University.

I am truly moved and inspired by his passion about engineering research. The year we spent together at Michigan was unforgettable. I learned and benefitted not only from his deep knowledge about batteries and cars, but his optimistic and caring characters. It is my great pleasure and fortune to work and study with him.

I am very thankful to all my labmates in the RACE lab: Yujia Cui, Jacob Faust, Zhenzhong jia, Hyeongjun Park, Zeng Qiu, Jun Hou, Esteban L. Castro, Richard Choroszucha, Hao Wang, Dave Reed and Kai Wu, and my friends at Michigan: Hong Yoon Kim, Heng Kuang, Shiyang Chen, Kangwei Mao, Chengwei Dai, Yang Chen, Yuxi Zhang and many others (this list could really go on forever without an end). None of my works would have been accomplished without the support of all my friends.

Finally I would like to express the greatest gratitude to my parents for their continuous and unconditional love and support. There will never be enough words to describe how important they are to me. They are always the most integral parts of my life. And to Cindy, managing a long distance relationship is almost as difficult as finishing the Ph.D. study and I am glad that we are able to go through so many things together even though we are separated by space. I look forward to our future days.

TABLE OF CONTENTS

LIST OF FIGURES

Figure

LIST OF TABLES

Table

LIST OF ABBREVIATIONS

OCV open circuit voltage

SOC state of charge

SOH state of health

BMSs battery management systems

EVs electric vehicles

HEVs hybrid electric vehicles

SEI solid electrolyte interphase

EIS electrochemical impedance spectroscopy

IC incremental capacity

ICA incremental capacity analysis

DVA differential voltage analysis

SVM support vector machine

SVR support vector regression

SVs support vectors

RSVM reduced support vector regression

LS-SVM least-squares support vector machines

VVT variable valve timing

EKF extended Kalman filter

QP quadratic programming

LP linear programming

LSM least squares method

ABSTRACT

Kernel Based Model Parametrization and Adaptation with Applications to Battery Management Systems

by

Caihao Weng

Co-Chairs: Jing Sun and Huei Peng

With the wide spread use of energy storage systems, battery state of health (SOH) monitoring has become one of the most crucial challenges in power and energy research, as SOH significantly affects the performance and life cycle of batteries as well as the systems they are interacting with. Identifying the SOH and adapting of the battery energy/power management system accordingly are thus two important challenges for applications such as electric vehicles, smart buildings and hybrid power systems.

This dissertation focuses on the identification of lithium ion battery capacity fading, and proposes an on-board implementable model parametrization and adaptation framework for SOH monitoring. Both parametric and non-parametric approaches that are based on kernel functions are explored for the modeling of battery charging data and aging signature extraction. A unified parametric open circuit voltage model is first developed to improve the accuracy of battery state estimation. Several analytical and numerical methods are then investigated for the non-parametric modeling of battery data, among which the support vector regression (SVR) algorithm is shown

to be the most robust and consistent approach with respect to data sizes and ranges. For data collected on $LiFePO_4$ cells, it is shown that the model developed with the SVR approach is able to predict the battery capacity fading with less than 2% error.

Moreover, motivated by the initial success of applying kernel based modeling methods for battery SOH monitoring, this dissertation further exploits the parametric SVR representation for real-time battery characterization supported by test data. Through the study of the invariant properties of the support vectors, a kernel based model parametrization and adaptation framework is developed. The high dimensional optimization problem in the learning algorithm could be reformulated as a parameter estimation problem, that can be solved by standard estimation algorithms such as the least-squares method, using a SVR special parametrization. The resulting framework uses the advantages of both parametric and non-parametric methods to model nonlinear dynamics, and greatly reduces the required effort in model development and on-board computation. The robustness and effectiveness of the developed methods are validated using both single cell and multi-cell module data.

CHAPTER I

Introduction

1.1 Motivation

The world's increasing prosperity and rapid economic growth continue to place additional demands on energy supply [1]. The International Energy Agency has projected that the world's energy demand and carbon-dioxide emissions will grow by 37% and 20%, respectively, from now to 2040, based on planned policies [2]. At the same time, the growing concern over oil shortage and environmental issues has greatly accelerated the development of alternative power and energy solutions to displace fossil fuels in recent years [3, 4]. It is essentially a new industrial revolution in which our energy sources need to be more affordable and sustainable, and our energy utilization should become more effective and efficient [1, 5].

As a key component in this revolution, energy storage systems are critical enablers for the next generation power/energy technologies [6–9]. In particular, the integration of energy sources with storage systems is crucial to the improvement of energy efficiency and conservation, for energy conversion systems as well as for new and renewable energy sources [1, 7]. Among the various choices of energy storage technologies, it is well recognized that lithium ion battery systems can offer a number of high-value opportunities given their advantages in portability and superior efficiency (See Fig. 1.1 for comparisons [10]). Lithium ion batteries have been used to power

an increasingly diverse range of applications, from cell phone and medical equipment to electric vehicles (EVs). The development of more reliable and efficient battery management systems (BMSs) have become vitally important [4, 11, 12].

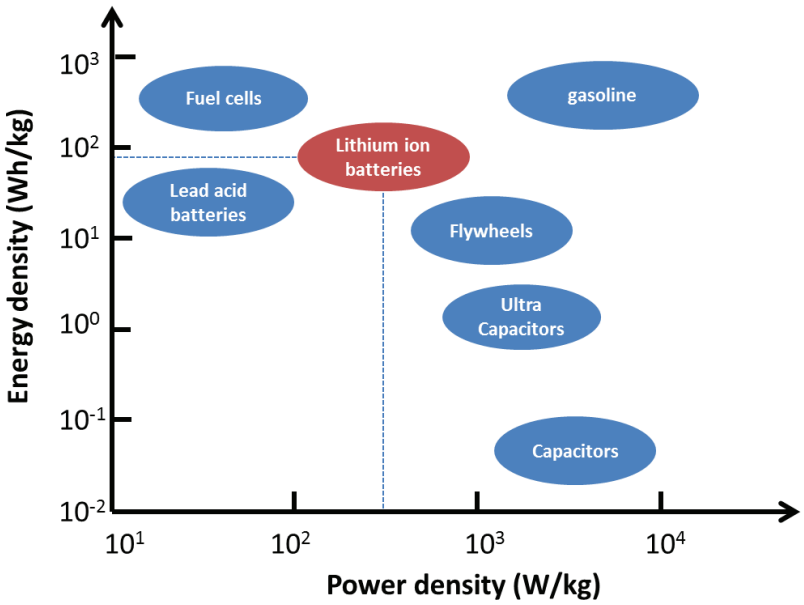

Figure 1.1: Ragone plot of common energy storage systems.

A BMS is an integration of hardware and software that monitors and controls the battery systems [13, 14]. The primary task of a BMS is to ensure safe and reliable battery operation in performing its function as a power source/sink [15]. By controlling the charging and discharging process, a BMS handles important functions such as limiting battery overcharge and preventing cell imbalance [11]. The complexity of a BMS design depends on the application. For most portable devices such as laptops and cell phones, the battery cells are slowly discharged and then recharged periodically [11]. The main responsibility of a BMS in this case is to recharge the batteries to full state of charge (SOC) with a safe charging protocol. Because of the easiness of battery replacement, longevity and service life extension are usually less concerned for those devices. For other applications such as the EVs and hybrid electric vehicles (HEVs), which operate large battery systems in dynamic environments,

the design of the BMS is a lot more sophisticated. For instance, the BMS of a HEV must coordinate with other vehicle components and power sources to ensure efficient operation while satisfying the driver's demand. The SOC and power capability of the battery also needs to be estimated continuously by the BMS to guarantee performance and safety. Moreover, due to the expected long service life and relatively large size of the battery system, battery aging and degradation become a much more influential factor for those applications. The state of health (SOH) management of battery systems thereby becomes one of the most important tasks for the BMS.

SOH is a measure that reflects the current condition of a battery in comparison with its fresh status [15, 16]. Battery SOH continuously deteriorates due to irreversible physical and chemical change during a life time. Batteries are complex systems that are not fully understood. The aging process is typically associated with multiple mechanisms that affect both capacity and resistance of the battery, leading to the reduction of the battery's energy and power density. In the case of lithium ion cells, the performance degradation could be caused by many phenomena such as the growth of solid electrolyte interphase (SEI) layers, loss of active materials, electrolyte decomposition, and electrode structural disordering [17, 18]. Most of those mechanisms are coupled during the aging process and cannot be isolated and studied independently, thereby making the investigation of battery aging mechanism more complicated [17]. On the other hand, inability to understand battery aging mechanism could lead to poorly designed battery management strategies, and cause severe loss of performance, shortened life, or even safety issues to the battery systems. Therefore, in order to achieve longer and more efficient battery operations, it is crucial (and extremely challenging) to study the aging phenomenon, and mitigate the aging effects by designing and implementing effective energy as well as SOH management strategies through the BMS.

One critical step in achieving effective battery energy management is the obser-

vation and tracking of battery states, namely SOC estimation and SOH monitoring, during the system operation. Many methods for on-line SOC estimation have been studied including coulomb counting [19], use of relation between open circuit voltage (OCV) versus SOC [20], and other model-based approaches with extended Kalman filters [21–24]. In contrast, the development of on-line SOH monitoring techniques is more difficult because of the lack of understanding of those complicated electrochemical mechanisms involved in battery aging, as mentioned above. Whereas it is possible to assess the resistance growth by both off-line tests such as electrochemical impedance spectroscopy (EIS) [25, 26] and on-line identification algorithms such as the use of least squares method [27–30], the detection of capacity fading still largely relies on laboratory measurements and off-line analysis [12, 31, 32].

The conventional method in determining battery capacity fading is by fully charging or discharging the battery, and computing the total charges transferred in the process [31, 33, 34]. However, the method requires time-consuming tests and additional energy cost, thus making it not suitable for on-board implementation with real-life operating constraints. An alternative approach of studying capacity loss is the so-called incremental capacity analysis (ICA) method [35]. ICA transforms voltage plateaus on charging/discharging voltage (V-Q) curves into clearly identifiable $\mathrm{d}Q/\mathrm{d}V$ peaks on incremental capacity (IC) curves [35]. ICA has the advantage to detect a gradual change in cell behavior during an aging process, with greater sensitivity than those based on conventional charge/discharge curves and yield key information on the cell behavior associated with its electrochemical properties [12, 36]. Another popular way of extracting battery aging signature and analyzing battery SOH from the voltage curve is the differential voltage analysis (DVA), which is based on the $\mathrm{d}V/\mathrm{d}Q$ curve. The accuracy of DVA-based capacity fading prediction has also been shown in many studies [37, 38].

Although ICA was shown to be an effective tool for analyzing battery capacity

fading, most studies using the tool have focused on understanding the electrochemical aging mechanism and few studies have been reported based on the on-board application of ICA. Meanwhile, since all the peaks on an IC curve lie within the voltage plateau region of the V-Q curve, which is relatively flat and more sensitive to measurement noise, calculating dQ/dV directly from the measured data without noise influence is difficult. Hence, effective and robust algorithms of obtaining the IC curve need to be developed.

This dissertation aims at developing a modeling and identification framework that can apply ICA for battery SOH monitoring with battery charging data that are normally available during operation. Several methods, including parametric models and numerical procedures, were developed and evaluated for extracting the IC peaks and associating them with capacity fading. The applicability of such frameworks to both individual cells and multi-cell battery modules/packs are investigated. Among the approaches that are explored in this work, a kernel-based method, namely support vector regression (SVR), is shown to be most robust and effective in extracting an aging signature experimental data. Moreover, the results delivered by the SVR approach motivate a study on the further improvement of the algorithm by taking advantages of the SVR model sparsity and adapting the kernel parameters.

1.2 Background

1.2.1 Aging Process of Lithium Ion Batteries

Understanding battery aging mechanisms is one of the most important steps toward effective battery energy and SOH management. Battery aging is a complex physical-chemical process, which is influenced by various operating conditions such as the SOC levels and the environmental temperatures [39–41]. The different aging mechanisms are usually coupled and occur at similar time scales [17, 42, 43]. There-

fore the performance degradation, typically reflected as capacity loss and increase of internal resistance, is often a result of a combination of different processes and their interactions [44, 45]. In general, the aging mechanisms of lithium ion batteries can be categorized as electrochemical and mechanical degradation.

The main electrochemical degradation processes include the growth of solid electrolyte interphase (SEI) layer, the lithium ion plating and the gas evolution due to oxidation of positive electrode material. A SEI film is a protecting layer formed on the negative electrode during first cycle [46]. It is generated to prevent electrolyte degradation by blocking electron passing through the layer. The initial formation of SEI consumes cyclable lithium ion, thereby leading to an irreversible loss of capacity[32, 42]. Moreover, due to instability of SEI, the layer continues to grow as battery ages. Because the SEI growth involves consumption of active lithium ions, consumption of electrolyte and exfoliation of the active electrode material, the process could further reduce the effective life of the battery [47]. SEI growth has been identified as the determining factor on the performance of lithium ion batteries. The formation of metallic lithium on the surface of the negative electrode is called lithium ion plating. The phenomenon occurs mostly when the battery cell is charged/discharged at low temperature or with high current rate [48]. Under both conditions, lithium ion is transported more rapidly than the intercalation rate and therefore deposited in metallic form on the anode surface. Lithium plating could result in a rapid capacity loss. The conductive lithium metal may become isolated from anode surface and accumulate in the separator. A metallic path through the separator can eventually be formed due to the continued lithium plating and cause a internal short circuit in the cell [49]. The gas evolution results from the decomposition of electrolyte and reactions with impurities in lithium ion batteries [50]. It is usually detected at high temperature or when battery cell is overcharged. The accumulation of gas could increase the cell internal pressure and lead to battery swelling, which

may eventually damage the cell enclosure [32, 50]. The mechanism could also reduce the active area of porous electrode structure and lower the cell conductivity.

The mechanical degradation is mainly related to the cyclic expansion and contraction during battery operation. Such deformation induces mechanical stress to the cell structure and causes fracture of the electrode material [51]. The formation of microcracks could develop into spanning cracks and break pieces of active material from the electrode, causing capacity loss [52, 53]. In addition, the cracks could expose the surfaces of the active material to the electrolyte, which eventually degrades the chemical stability and safety of the battery [54]. Therefore, the mechanical degradation, especially that associated with structural changes, also affects the battery performance significantly.

While the aging processes are found to be in those general areas, the exact mechanisms that lead to the aging, the operating conditions that slow or accelerate the aging are not well understood. For the SOH management, one common approach is to focus on the chief or dominant mechanisms (for instance, the SEI growth) that contribute to capacity or power fade, and develop simplified or reduced-order models to capture the aging behavior [18, 42, 55, 56]. The models could then be used to optimize the battery management strategy that may mitigate the aging effects and prolong the service life. The research on lithium-ion battery aging mechanism is still a fast evolving area and continues to attract more attentions in the battery research community.

1.2.2 Estimation of Battery States

The estimation of battery states, especially SOC and SOH, is an integral part of on-board battery energy management [57]. SOC is commonly defined as "the percentage of the maximum possible charge that is present inside a rechargeable battery", and the estimation of SOC serves as the "fuel gauge" for batteries. SOH is

"a 'measure' that reflects the general condition of a battery and its ability to deliver the specified performance in comparison with a fresh battery" [15]. Typically, the quantitative definition of SOH is based on either the battery capacity or the internal resistance, depending on specific applications [16].

Many studies of battery SOC estimation have been reported in the literature [14, 19, 58]. The most popular way for calculating SOC is the Coulomb counting method, which is based on the continuous integration of charge/dicharge current. It is commonly used due to its simplicity. However, the estimation accuracy is limited due to current measurement error and uncertain energy losses during operation. Another popular method is based on the OCV function [20]. Because the OCV of a battery is monotonic with respect to its SOC, the corresponding relationship between the two values can be used as a look-up table for SOC estimation. In order to accurately represent the OCV, the battery cell needs to be tested for a long time with slow charging and long relaxation intervals [35]. Therefore this method is not readily applicable for dynamic application such as EVs and HEVs. Moreover, for batteries that have flat OCV-SOC function (e.g., $LiFePO_4$ cells), the effectiveness of the method would be greatly reduced. Kalman filter based SOC estimation is the most promising technique at the moment [21–24]. Despite a relatively higher computational cost compared to Coulomb counting and OCV-based methods, this type of method can capture the system dynamics in real-time and use the closed-loop structure for self-correction, thereby limiting the estimation error range [58]. There are also learning based algorithms such as using the artificial neural network and fuzzy-logic [59–62]. The reliability and robustness of those methods heavily depend on the quality of the training data [58].

The SOH determination of battery is usually associated with two factors: resistance growth and capacity degradation [41, 63]. For the detection of resistance growth, both off-line and online methods have been reported in literature. EIS is

the most commonly used method for evaluating resistance growth off-line. In a laboratory setting, electrochemical impedance is usually determined by applying an AC potential to the battery cell and measuring the current through the cell [64]. Instead of one frequency, EIS measures the impedance change for a wide frequency range, thereby allowing the characterization of many aging effects [25]. On the other hand, for on-board applications, the resistance is typically measured by applying an equivalent circuit model together with a parameter estimation algorithm such as the least squares method [27–30]. Due to the rich dynamics of vehicle driving cycles, persistent excitation is usually guaranteed for the estimation of battery resistance [65]. The online estimation result could help the prediction of vehicle power capability and the development of optimal energy management strategies [66–71].

The conventional methods in determining battery capacity fading are mostly based on the measurement of the fully charging and discharging data [31, 33, 34]. For lithium ion batteries, one can either measure the usable capacity by computing total charge transferred during the charging and discharging, or apply techniques such as ICA and DVA to quantify the capacity loss through certain aging signature. In particular, the ICA technique differentiates the battery charged capacity data (Q) with respect to the terminal voltage (V), and transforms the plateaus of the voltage curve into clearly identifiable $\mathrm{d}Q/\mathrm{d}V$ peaks on the incremental capacity (IC) curve (See Fig. 1.2) [32, 35]. Those signatures are related to first-order phase transformations and formations of solid solution during the intercalation process. The concept of ICA originally came from the intercalation process of lithium and the corresponding staging phenomenon at the graphite anode [32, 72–74]. It helps to detect gradual changes in cell behavior with greater sensitivity [12]. ICA is applicable to lithium ion batteries that use graphite as the negative electrode material since it originates from the study of the lithium intercalation process [32, 72–74]. The efficacy of ICA has been shown with various lithium ion batteries ($LiFePO_4$, LiNMC, LNCAO, $LiMn_2O_4$, etc.) [35, 36, 75–

77]. In Ref. [77], the aging signature extracted using ICA is further amplified through the delta differential capacity analysis technique, which enables people to detect small battery degradation in a shorter time interval [32, 39, 78]. In contrast to the ICA, the DVA is based on differentiation of voltage with respect to the charged capacity (i.e., $\mathrm{d}V/\mathrm{d}Q$). Similar to ICA, DVA quantifies the battery capacity loss by analyzing the peak changes on the $\mathrm{d}V/\mathrm{d}Q$ curve [37, 38].

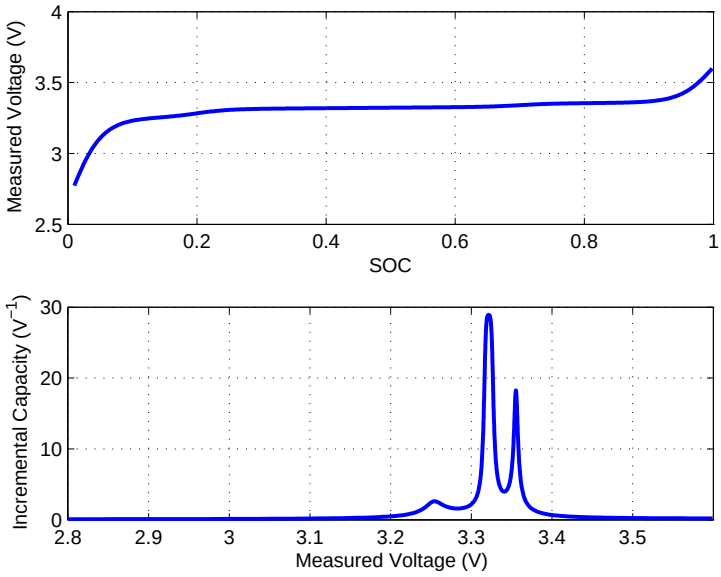

Figure 1.2: ICA performed on charging voltage curve at $\frac{1}{20}$ C rate.

One major difficulty in performing ICA and DVA is the sensitivity to noise in battery voltage measurement [16, 75, 77]. Since all the peaks on an IC curve lie within the flat region of the voltage curve, computing the derivatives directly from the data could lead to inaccurate and undesirable results, even after careful data filtering. This issue could be addressed by implementing specially designed high precision testing equipment [39, 77]. However, for on-board application, the measurement precision is usually limited and appropriate data processing is required.

1.2.3 Modeling of Open Circuit Voltage

The modeling of OCV is found to be critical in both SOC estimation and SOH determination for lithium ion batteries. Most SOC estimation methods are model-based approaches and require an accurate model that relates OCV to SOC [19–21, 33]. The OCV-SOC function is implemented in the BMS either as a look-up table or an analytical expression, while the latter has several advantages including computational efficiency (since no interpolation is needed) as well as the convenience for analysis. However, for batteries that have a wide flat region on the OCV-SOC curve (e.g., $LiFePO_4$ batteries), a small mismatch in OCV fitting may cause a large deviation in SOC estimation. Therefore, improving OCV models can contribute significantly to increasing the accuracy of SOC estimation. The importance of OCV modeling is also shown in SOH monitoring, as OCV data often reflect battery aging and performance degradation [31, 79, 80]. ICA and DVA both originate from the analysis of OCV data.

In Ref. [81], several phenomenological OCV models, which are built with curve fitting without considering the complex battery physical behavior during the lithium-ion intercalaction/deintercalation process [3, 82], are summarized. Although those models represent part of the nonlinear characteristics of battery OCV, they fail to capture the voltage plateaus and transitions (please see Fig. 1.2) that correspond to the staging phenomenon at the graphite anode [32, 35, 72–74].

By constructing an OCV model that represents the underlying physical phenomenon of lithium-ion intercalaction/deintercalation process and therefore captures the subtle transitions over the flat region, one can take advantage of the analytical form of the model to extract useful information associated with battery electrochemical properties and aging status using ICA [12, 36]. The effect of measurement noise could also be mitigated by fitting the raw data with a specially structured parametric model. For both SOC estimation and ICA-based SOH monitoring, an OCV model

that can capture the physical process over the flat region of the OCV-SOC curve is needed for lithium ion battery .

1.2.4 Non-Parametric Modeling Using the Support Vector Machines for Regression

In the statistics and machine learning communities, parametric models are defined as the ones whose functional structures are given and can be parametrized by a finite number of parameters, while the nonparametric models have an indefinite number of parameters depending upon the given data set. Examples of non-parametric models include the histogram, the k-Nearest Neighbors model and the decision tree model. The main advantage of non-parametric modeling methods is that they require less or no prior knowledge about the system or the data, so that the application of such methods are particularly effective for systems with unknown nonlinear dynamics.

For the non-parametric identification of nonlinear dynamic systems such as the battery system, the support vector machine (SVM) algorithm is an ideal candidate due to its excellent approximation and generalization capability [83]. The SVM algorithm was initially developed by Vapnik et al. at the AT&T Bell Laboratories, for data classification [84]. It has been an active area of research and played a significant role in solving problems such as data classification and function estimation over the last two decades [85–87]. The method relies on the use of the kernel trick, which maps data points to a higher dimensional feature space through an inner product to make the data linearly separable, so that a nonlinear separating surface can be represented with a linear model in the feature space [85, 88]. Consequently, the nonlinear data can be estimated and classified using linear methods as long as the problem is formulated in terms of kernel evaluations [89, 90]. As a nonlinear generalization and extension of the Generalized Portrait algorithm, the SVM algorithm is firmly grounded in the framework of statistical learning theory [83, 91]. Therefore, it has attracted signifi-

cant interests not only inside the field of machine learning but also from the statistics and mathematics community due to its advantages in both theoretical insights and practical usefulness [89, 90].

The support vector regression (SVR) method is the application of SVM algorithm for regression [84]. Different from the SVM algorithm for data classification (e.g., output $y \in \{\pm 1\}$ in a two-classes case), the SVR problem is concerned with estimating real-valued functions (i.e., output $y \in \mathbb{R}$) [88]. By incorporating the ε-insensitive loss function, a regression problem is constructed such that a function $f(x)$ that has at most ε deviation from the target values y can be found[83, 88, 92]. In this case, estimation errors less than ε are treated as zero and only the losses greater than ε are concerned in the objective function. It has been shown that the use of ε-insensitive loss functions yield sparse and thus generalizable solutions [93].

Despite the simple structure, the standard SVR algorithm involves solving an optimization problem whose dimension depends on the size of the training data set, and therefore requires non-trivial computational efforts to determine the model parameters. Since the resulting high dimensional optimization process is often computationally expensive, the potential applications are limited, particularly for on-board and real-time estimation problems. Moreover, unlike most SVR problems where the optimization is only performed once, for applications such as the SOH monitoring of a multiple-cell battery system, the algorithm needs to be applied to every cell individually and repeatedly to capture the effects of aging and cell-to-cell variations. The need for repeated optimization can dramatically increase the computational burden and make the real-time implementation on resource limited platforms difficult or impossible. An alternative algorithm, known as the reduced support vector regression (RSVM), was developed to address the issue of high dimensions by reducing the number of constraints in the optimization [87]. Other methods such as the least-squares support vector machines (LS-SVM), the Chunking method and the sequential

minimization optimization have also been discussed in the literatures [83, 87]. However, none of those approaches is applicable to our problem to meet the real-time computational requirements.

1.2.5 Model Parametrization Based on the Invariance of Support Vectors

The simple and sparse structure of the SVR representation, resulting from the optimization process, provides a natural choice of parametric model for on-board adaptation. If the SVs remain invariant from the SVR model of one data set to another, then only the coefficients of the SVR model need to be updated for model identification. By fixing the kernel functions and the values of the SVs, the SVR model could be treated as a linear parametric model whose weighting parameters can be directly identified using estimation algorithms such as the least squares method. The iterative optimization procedure could thereby be dramatically simplified. The parametric structure could also help to better understand the physical properties of the underlying problems and take advantage of the knowledge one has about the systems [94]. As an example, the study reported in Ref. [95] exploits the parametric SVR model for the real-time adaptation of gasoline engine air systems. It is shown that the SVR model identified from a reference engine data could be applied for the modeling of a different four-cylinder engine with intake variable valve timing (VVT). For the application of battery SOH monitoring, since the aging data sets all have common features, it is conjectured that the optimization only needs to be applied to one of the data sets as a starting point, and the resulting SVR model structure and SVs can be used as a basis for the derivation of parametric models for other data sets. With the development of the parametrization framework based on the the invariance of SVs, the computational complexity may be greatly reduced by limiting the high dimensional optimization to the baseline data sets.

1.3 Dissertation Work Scope and Contributions

This dissertation aims at developing an on-board implementable model parametrization and adaptation framework, that utilizes the kernel functions used in learning algorithms, for battery energy management. Through the study of both parametric and non-parametric modeling approaches, an ICA based on-board battery SOH monitoring framework is proposed, and its efficacy is demonstrated through on data sets collected through battery aging experiments.

The main contributions are summarized as follows:

1. Developed an SOH monitoring strategy that combines data-driven and electrochemical-based approaches, demonstrated that the capacity estimation model built upon the data from one cell is able to predict the capacity fading of multiple different cells with less than 2% error.

2. Established ICA as an useful tool for battery on-board SOH monitoring. Investigated the use of SVR for effective ICA signature extraction. Identified the correlation between peaks on IC curve and battery capacity fading, through which battery capacity can now be estimated with partial charging data.

3. Developed an ICA motivated OCV model with special parametrization that considers the staging phenomenon for lithium-ion batteries, and demonstrated its utility in SOC estimation and SOH monitoring. The model is shown to be capable of reflecting battery cell's electrochemical properties at different operating temperature conditions and aging stages.

4. Exploited the invariance of the SVs using parametric linear programming and sensitivity analysis. Explored the variation feature of battery aging data. Established a model parametrization and adaptation framework. Demonstrated computational efficiency improvement.

5. Extended the battery SOH monitoring framework from single cells to battery modules that have multiple cells connected in parallel. Showed the robustness of ICA with respect to both cell capacity and resistance non-uniformity inside the modules.

6. Designed and conducted long-term battery aging tests on $LiFePO_4$ cells and modules. Built a database that consists of battery aging test data under various load and environmental conditions. The data sets have been shared with collaborating universities and institutions.

1.4 Dissertation Outline

This dissertation is organized as follows:

In Chapter II, the effectiveness of ICA for battery SOH monitoring is illusrtated. ICA is applied to OCV data that are identified off-line with a simplified parametric model. The monotonic characteristic of IC peaks as battery ages is verified, and a correlation between capacity and IC peak is established.

In Chapter III, a unified OCV-SOC model motivated by the ICA application is proposed. The development and parametrization of the new OCV model is presented, with comparisons to other existing models in terms of OCV data fitting and SOC estimation accuracy. The application of the OCV model for SOH monitoring is elucidated. Parametric analysis and model simplification are also discussed.

In Chapter IV, the extraction of IC peaks using non-parametric approaches is investigated. Several numerical procedures are applied and evaluated. The implementation of SVR for ICA is discussed in detail. The associated results for on-board battery capacity estimation are presented.

Chapter V reports the findings of exploiting the parametric SVR model for real-time battery system characterization, and proposes a framework for on-line battery

SOH monitoring. The LP-SVR problem for the identification of V-Q curve is extended into a parametric LP problem with sensitivity study. The effects of characterization of battery aging are illustrated through simulation and actual test data. The parametric LP problem is solved using Monte Carlo simulations and the parametric V-Q curve model based on the invariance of the SVs is established.

Chapter VI extends the ICA based SOH monitoring framework from single cells to battery modules. The application of ICA for battery pack is analyzed using a module simulation model with physical aging mechanism. The sensitivity of ICA with respect to cell non-uniformity is investigated. Experimental results of the model SOH monitoring framework applied to a inventory of about 30 battery cells are presented.

The conclusions and suggested future work are given in Chapter VII.

CHAPTER II

Battery State-of-Health Monitoring Using Incremental Capacity Analysis

The battery state-of-health (SOH) monitoring framework proposed in this dissertation is established on the basis of the electrochemical characterization method, known as incremental capacity analysis (ICA). The ICA method differentiates the battery charged capacity (Q) versus the terminal voltage (V) and transforms voltage plateaus on the charging/discharging voltage (V-Q) curve into clearly identifiable $\mathrm{d}Q/\mathrm{d}V$ peaks on the IC curve [32, 35]. In this chapter, the effectiveness of ICA for battery SOH monitoring is demonstrated through the off-line identification of the open circuit voltage (OCV) data.

2.1 Introduction of Incremental Capacity Analysis

The concept of ICA originates from the study of the lithium intercalation process and the corresponding staging phenomenon [72, 73, 96, 97]. Using graphite based cell as an example, during the charging (or discharging) process, when the lithium ions are intercalated into (or de-intercalated from) the carbon electrode, the graphene sheets together with the solid phase lithium ions are arranged periodically to form different stage structures [98]. Those stages are associated with different energy levels in the

negative electrode, and reflected as multiple voltage plateaus on the battery OCV curve. The ICA technique can be used to characterize the electrochemical properties related to the intercalation process by computing the IC curve as,

$$IC = \frac{dQ}{dOCV} \tag{2.1}$$

and transforming the voltage plateaus into clearly identifiable peaks, where Q represents the charged capacity. In practice, the OCV data are often substituted with slow charging/discharging (for instance, 1/25 C rate) voltage data (V) under constant current. The voltage obtained in this way is sometimes referred as close to equilibrium OCV data [35]. The dQ/dV based ICA curve could accurately reflect the characteristics of the underlying battery, given that the results are properly computed, due to the following equivalence,

$$\frac{dQ}{dV} = \frac{dQ}{d(OCV + IR)} \approx \frac{dQ}{dOCV} = IC \tag{2.2}$$

where V, I, R are the battery voltage, current and internal resistance, and $dIR \ll dOCV$ when dI is small.

ICA has the advantage to detect a gradual change in cell behavior during the aging process [35, 76]. It is useful particularly for battery SOH monitoring as the extracted peak intensities and their change pattern are closely related to the battery capacity fading.

2.2 Battery Testing Systems and Data Collection

The efficacy of ICA for SOH monitoring will be illustrated using experimental data obtained from a battery life cycle test. Most of the studies reported in this dissertation are based on data sets collected from A123 APR18650 cells, which use $LiFePO_4$ as

the positive electrode material and graphite as the negative electrode, over a period of 24 months [16, 99]. The details of our multi-cell module tests, which share most of the set ups for the single cell test, will be presented in a later chapter. The test data are acquired through a battery test bench (shown in Fig. 2.1), which includes an Arbin BT2000 tester, a thermal chamber for environment control, a computer for user-machine interface and data storage, a switch board for cable connection, and battery cells [16, 99]. The data acquisition system has a logging frequency of 10Hz, and the measurement precision of both current and voltage is 0.02% (i.e., $1mV$ for voltage measurement).

Table 2.1: Main Specifications of the $LiFePO_4$ Cell

Nominal capacity (Ah)	Nominal voltage (V)	Upper cut-off voltage (V)	Lower cut-off voltage (V)
1.10	3.30	3.60	2.00

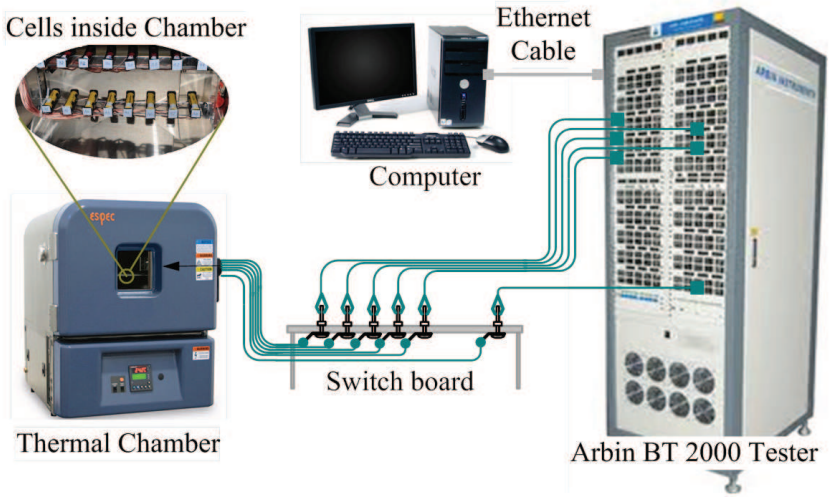

Figure 2.1: Experimental set up of the battery tests.

The batteries used for this test are lithium ion phosphate ($LiFePO_4$) cells from A123 (APR18650M1A) with the specifications listed in Table 2.1. Eight cells are tested with the same load profile for comparison and validation. As shown in Fig. 2.2, the experiment procedure starts with a series of characterization tests (which

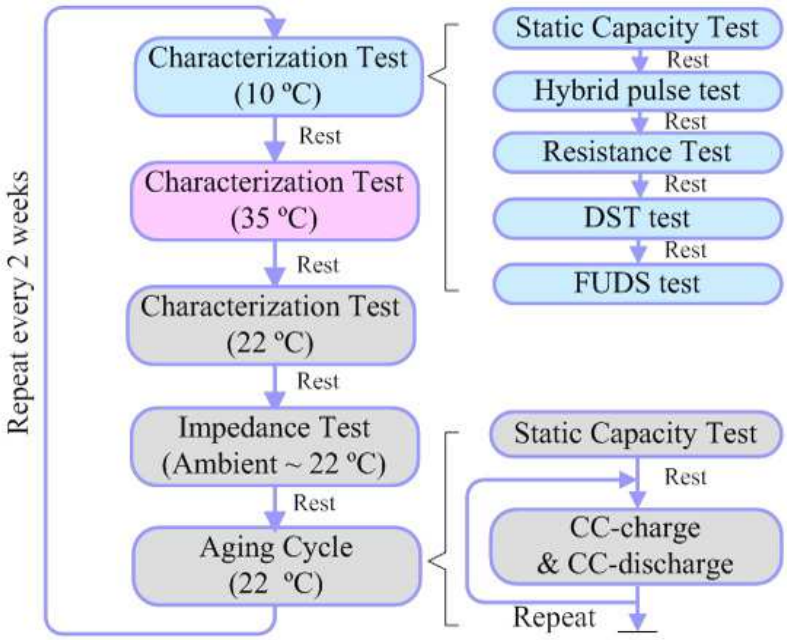

Figure 2.2: Battery test schedule.

consist of a static capacity test, a hybrid pulse test, a DC resistance test, a dynamic stress test (DST) and a Federal Urban Driving Schedule (FUDS) test) conducted at three different temperatures (in the order of 10^{o}C, 35^{o}C and 22^{o}C). After these tests, 100 aging cycles are conducted at 22^{o}C. In each aging cycle, the cells are charged and discharged at a constant rate until the cut-off voltage is detected [81]. For this study, the data sets from the static capacity test are mainly used. More detailed discussion of the battery testing systems and schedules can be found in [81]. The data collected through this set up will be used in the rest of this dissertation.

2.3 Off-line Application of Incremental Capacity Analysis Results

The ICA technique employs the IC ($\mathrm{d}Q/\mathrm{d}V$) curves to detect gradual changes in the electrochemical behaviors of lithium ion batteries. The analysis associates the evolution of the IC peaks with the battery aging process and serves as an effective

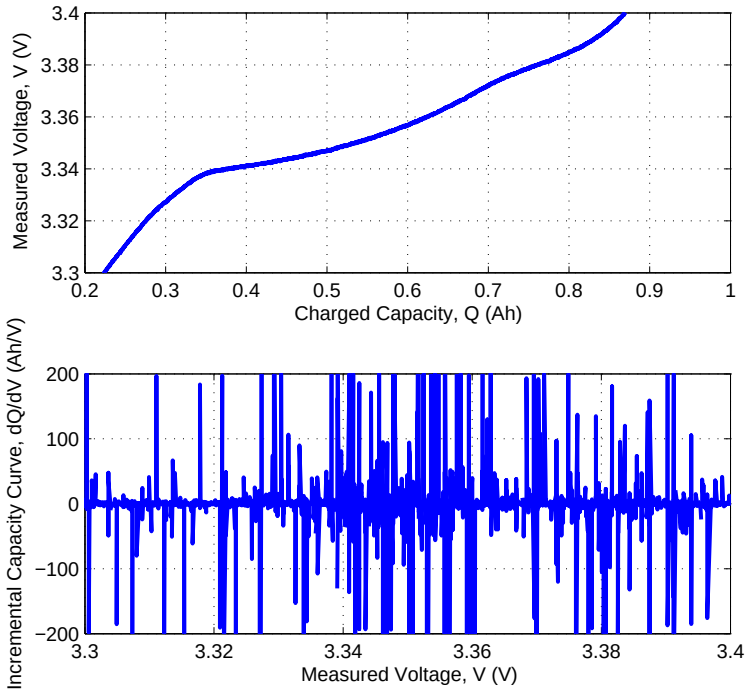

Figure 2.3: Sensitivity of the numerically derived $\mathrm{d}Q/\mathrm{d}V$ curve to measurement noise.

tool for SOH monitoring. Ideally, one can just take the voltage and current data from charging or discharging process and compute the $\mathrm{d}Q/\mathrm{d}V$ curves. However, because of measurement noise, performing the ICA directly from the measured V-Q curve has proven to be not a viable option [16, 39, 75, 77], especially for on-board BMS, where the measurement precision is limited. Fig. 2.3 shows how sensitive numerical differentiation is to the measurement noise. Therefore, it is required to develop appropriate data processing methods so that ICA can be applied. For this study, both parametric and non-parametric approaches are considered to solve this problem. The former rely on the development of a parametric model with determined structure whereas the latter typically use numerical and learning procedure to identify the model parameters as well as the model structure.

To quickly illustrate the effectiveness of applying ICA for battery SOH monitoring, we start by identifying OCV curves from the experiment data set using a simplified

parametric model developed in [22–24]. The selected model has linear parameters so that their values could be directly computed. The identification of such OCV curves requires test data that span the entire SOC range and therefore is only applicable during off-line study. The model is not developed for the purpose of SOH monitoring and therefore it does not capture all the features embedded in the test data. Nevertheless, this model could bring useful insights on the development of methodologies for the application of ICA.

The model of the OCV curve is expressed as

$$OCV(z) = K_0 - \frac{K_1}{z} - K_2 z + K_3 ln(z) + K_4 ln(1-z) \tag{2.3}$$

where $K_{0\sim4}$ are the model parameters and z is the normalized SOC, and the discrete battery model used for charging/discharging process is formulated as

$$\begin{aligned} z_{k+1} &= z_k - (\frac{\eta_i \Delta t}{C}) i_k, \\ y_k &= OCV(z_k) - R i_k \\ &= K_0 - \frac{K_1}{z_k} - K_2 z_k + K_3 ln(z_k) + K_4 ln(1-z_k) - R i_k \end{aligned} \tag{2.4}$$

where η_i is the charging/discharging efficiency, Δt is the time step, C is the battery capacity, i_k is the input current, y_k is the model output (terminal voltage), z_k is the SOC and R is the parameter that represents battery internal resistance [81].

Because the battery model is linear in parameters, we could thus formulate the estimation problem as the following

$$\begin{aligned} y_k &= \theta_V^T \phi_{Vk}, \\ \theta_V &= [K_0, K_1, K_2, K_3, K_4, R]^T, \\ \phi_{Vk} &= [1, -\frac{1}{z_k}, -z_k, ln(z_k), ln(1-z_k), i_k]^T. \end{aligned} \tag{2.5}$$

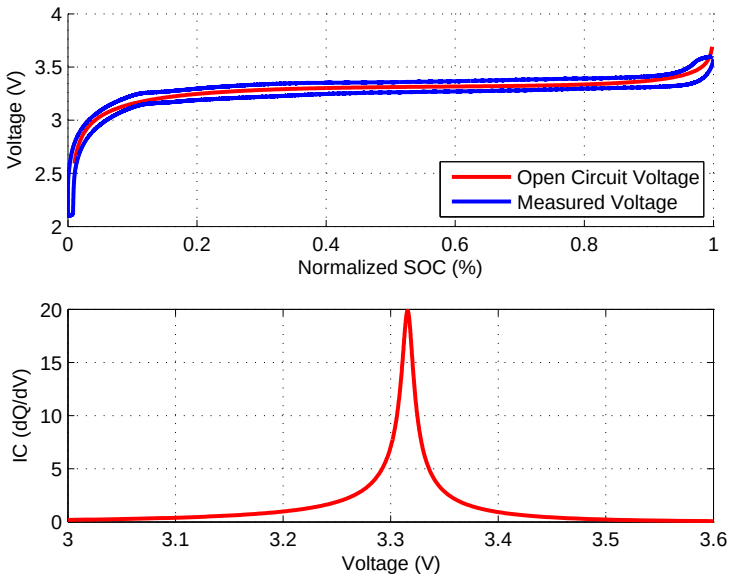

Figure 2.4: OCV and IC curve identified from static capacity test.

The parameters θ_V can be solved by the standard least squares method,

$$\begin{aligned} \theta_V &= (\Phi_V^T \Phi_V)^{-1} \Phi_V^T Y, \\ \text{where } Y &= [y_1, y_2, ..., y_n]^T, \\ \Phi_V &= [\phi_{V1}, \phi_{V2}, ..., \phi_{Vn}]^T. \end{aligned} \tag{2.6}$$

An example of the OCV identification results and the corresponding IC curve is shown in Fig. 2.4. With the parametric OCV model identified, the IC curve is obtained by taking analytic derivative of the mathematic expression (2.3). One single peak can be observed from the IC curve. It should be noted, according to [35], there are three identifiable peaks on the IC curve. However, the number of peaks that can be extracted numerically from the experimental data depends on the OCV model and the numerical approach. Using the simplified parametric model (2.3) and analytic derivative calculation, only one peak is identified. Nevertheless, the purpose of using this parametric OCV model is to reveal and validate that the aging signature can indeed be extracted from battery data through ICA. In later chapters, however,

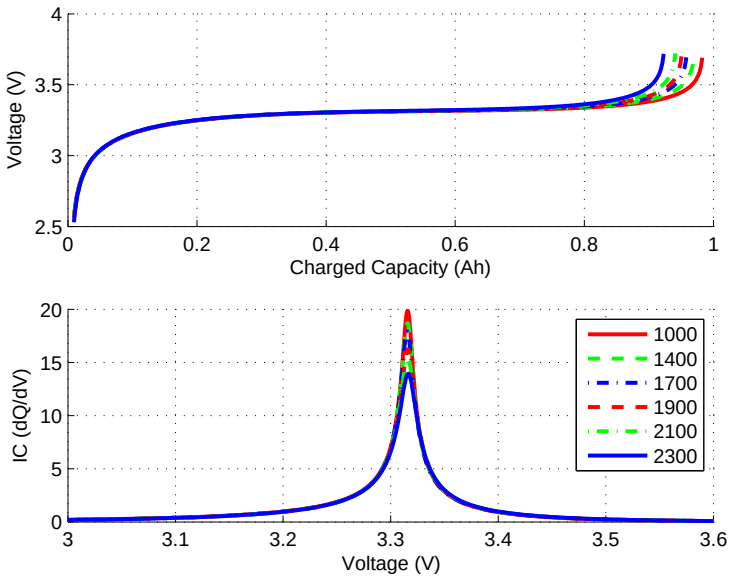

Figure 2.5: Comparison of OCV and IC curve at different battery aging cycles.

we will discuss how ICA can be applied directly to battery charging data with both parametric and non-parametric approaches, and show results where all three peaks are identified.

Applying the identification procedure to different data sets collected at different aging cycles, the results shown in Fig. 2.5 represent the change in OCV and IC curve for the first 2300 cycles of one battery under testing. Compared with the other cells, the battery #7 in Fig. 2.6 shows the most consistent aging behavior and is therefore used as the reference battery cell in our study. The numerical values in the plot legends represent the aging cycle number. Monotonic trends in the peaks, as the battery ages, can be clearly identified on both OCV and IC curves. However, notice that the IC curve provides not only greater sensitivity than the OCV curve, but also does so in the normal range of voltage operation (around 3.3V) rather than at high voltage range.

The same trend can be observed from all eight cells at all temperatures. Fig. 2.6 shows the normalized IC peak values for all battery cells during the aging process.

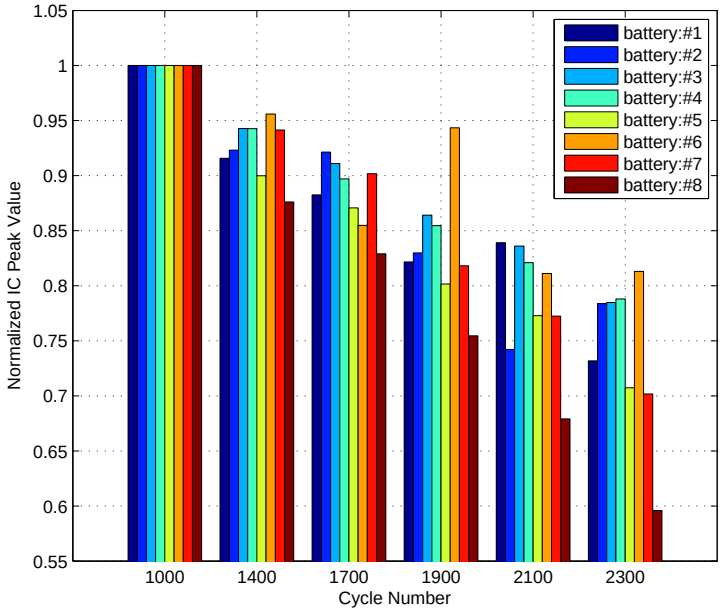

Figure 2.6: IC peak value comparison for all eight cells.

With the exception of 4 outliers out of 48 data sets, the eight cells give consistent decreasing IC peaks, which confirms the validity of using IC peaks as the signature for battery capacity fading.

At last, the battery capacity is plotted versus the IC peak in Fig. 2.7 and a linear correlation can be observed between the two values.

In this chapter, the monotonic characteristic of IC peaks as batteries degrade is verified through the off-line identification, and a correlation between capacity and IC peak is established. Therefore ICA is shown to be a useful tool for battery SOH assessment. However, the major difficulty in implementing ICA is the computation of the IC curve directly from the measured data on-board. For on-line SOH monitoring, OCV curves change as batteries age, and the updated OCV curves are not available for conducting ICA. Moreover, most real-life charging data does not span the entire SOC range, thus the off-line identification method discussed in this Chapter cannot be directly applied. On the other hand, since the peak of IC curve appears around the nominal voltage of $3.3V$, we believe that this signature can be extracted from normal

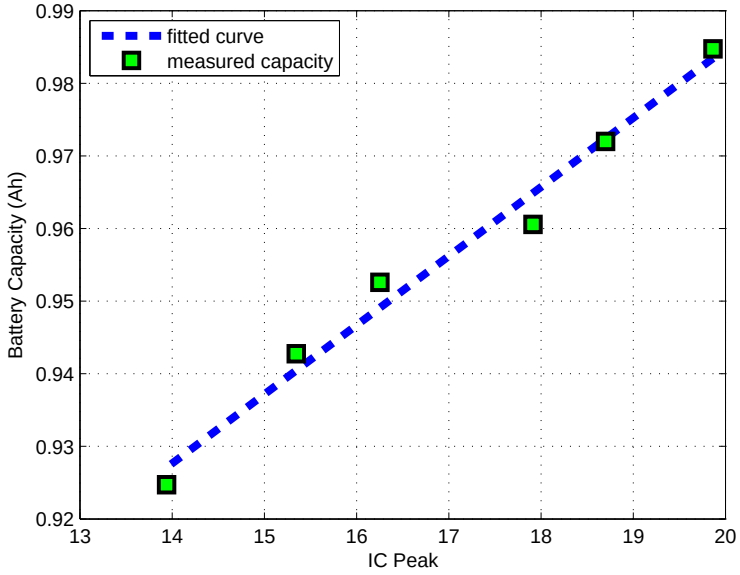

Figure 2.7: Correlation between battery faded capacity and IC peak.

EV charging data (which is limited in its SOC range) with appropriate algorithms.

In the following chapters, both parametric and non-parametric approaches are developed for the on-board implementation of ICA, with partial battery charging data that are obtainable during real-life vehicle operations.

CHAPTER III

A Unified Parametric Open-Circuit-Voltage Model for State-of-Charge Estimation and State-of-Health Monitoring

The study reported in the previous chapter shows promising results on applying incremental capacity analysis (ICA) for battery state-of-health (SOH) monitoring. However, the implementation replies on the availability of charging voltage and discharging voltage data that span the entire state-of-charge (SOC) range. On the other hand, the simplified open circuit voltage (OCV) model only captures part of the aging features from the voltage data. In this chapter, we propose a unified OCV model that can be applied for both SOC estimation and SOH monitoring. In particular, it is shown that the proposed OCV model can be used to perform battery SOH monitoring as it effectively extracts aging information based on ICA. Parametric analysis and model complexity reduction are addressed, and experimental data is used to illustrate the effectiveness of the model and its simplified version in the application context of SOC estimation and SOH monitoring.

3.1 A New Open-Circuit-Voltage Model

OCV models and data are widely used for characterizing battery properties under different conditions. They contain important information that can help to identify battery SOC and SOH. While various OCV models have been developed for battery SOC estimation, few have been designed for SOH monitoring. In this chapter, a new OCV model structure, that can capture the phenomenological characteristics associated with the lithium-ion intercalaction/deintercalation process while fitting the OCV-SOC data, is proposed here. A specific model structure is chosen to enforce the model to exhibit plateaus on the OCV curve. These plateaus are results from the lithium-ion staging phenomena, and have been irrefutably observed from experimental data. The parameters of the proposed model will be identified with experiment data. Instead of measuring the OCV after a long relaxation period at different SOC levels that span the entire range, the data used are collected by charging/discharging a $LiFePO_4$ battery cell at low rate of $\frac{1}{20}$ C under room temperature. The voltage data obtained by this slow charging/discharging process reflects the OCV at a close-to-equilibrium status [35]. Although the close-to-equilibrium OCV curve shown in Fig. 3.1 may be affected by hysteresis and diffusion voltage due to lack of relaxation, it can sufficiently represent the generic electrochemical properties for ICA and quantifying capacity fading as presented in Ref. [35]. The upper and lower cut-off voltage limits are set to be 3.6 V and 2.1 V respectively. The total charge stored between the upper and lower limits is defined as the battery capacity.

3.1.1 Open-Circuit-Voltage Parametric Model

Based on the studies presented in Refs. [16, 32, 35], there are generally three observable voltage plateaus and two transitions, which are important in characterizing the OCV and battery capacity, over the flat area on the OCV curve of $LiFePO_4$ battery cells. In our model, those plateaus and transitions are represented by the sigmoid

functions as follows,

$$\begin{aligned} OCV(z) =& K_0 + K_1 \frac{1}{1+e^{\alpha_1(z-\beta_1)}} + K_2 \frac{1}{1+e^{\alpha_2(z-\beta_2)}} \\ &+ K_3 \frac{1}{1+e^{\alpha_3(z-1)}} + K_4 \frac{1}{1+e^{\alpha_4 z}} + K_5 z \end{aligned} \tag{3.1}$$

where z is the SOC, $K_{0\sim5}$ are the linear parameters, and $\alpha_{1\sim4}$ and $\beta_{1\sim2}$ are parameters in the nonlinear functions. This parametrization shares features with some of the electrochemical model of $LiFePO_4$ proposed in Ref. [3]. More specifically, our model can be interpreted as a simplified composition and generalization of the cathode and anode OCV functions in Ref. [3] (where hyperbolic and exponential functions are used).

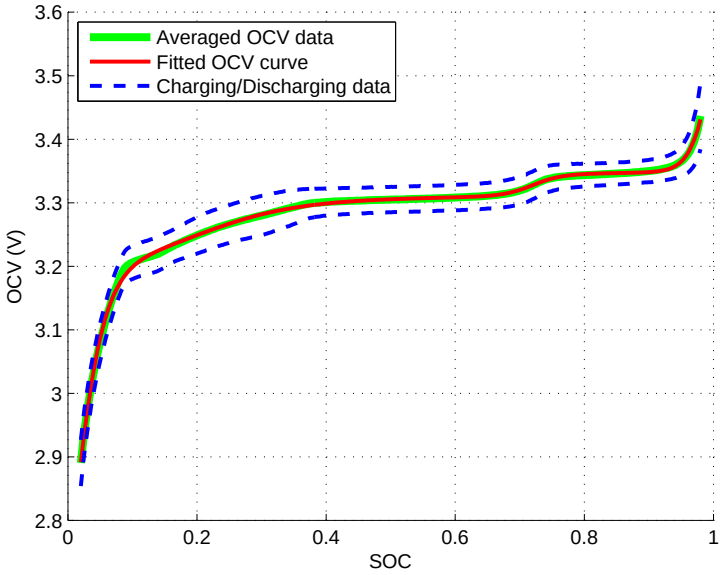

Figure 3.1: Fitting result with the proposed OCV model.

An example of a complete data set for model identification is shown in Fig. 3.1, where the collected charging/discharging data are averaged to yield OCV data. The parameters in Eq. (3.1) are determined using the Matlab curve fitting toolbox. We focus on fitting the data in the middle SOC range, namely 10%-90% SOC, given that in practice only data in the middle SOC range are available. Moreover, this allows

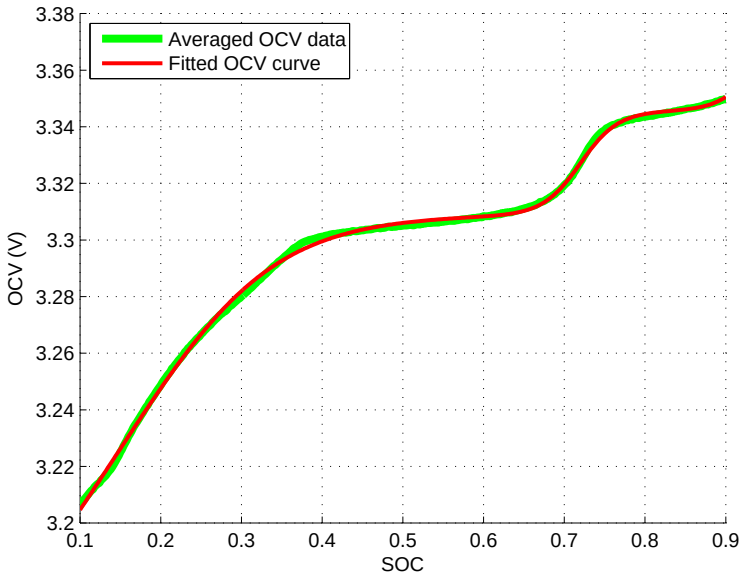

Figure 3.2: OCV model fitted over SOC from 10% to 90%.

us to achieve higher accuracy in the range where the model will be most useful. The fitted OCV-SOC curve is plotted in Fig. 3.2, with a reference made to the averaged measured OCV data. The rms and maximum values of fitting error is 1 mV and 2.5 mV, reduced from 2.3 mV (rms)and 7 mV (maximum) that were obtained when the full SOC range is used.

3.1.2 Model Comparison and Analysis

Table 3.1: OCV models from literatures together with the new model

#		OCV Models	Ref.
1	$OCV(z) =$	$K_0 - \frac{K_1}{z} - K_2 z + K_3 \ln(z) + K_4 \ln(1-z)$	[23]
2	$OCV(z) =$	$K_0 + K_1(1 - e^{-\alpha_1 z}) + K_2(1 - e^{-\frac{\alpha_2}{1-z}}) + K_3 z$	[100]
3	$OCV(z) =$	$K_0 + K_1 e^{-\alpha_1(1-z)} - \frac{K_2}{z}$	[101]
4	$OCV(z) =$	$K_0 + K_1 e^{-\alpha_1 z} + K_2 z + K_3 z^2 + K_4 z^3$	[102]
5	$OCV(z) =$	$K_0 + K_1 z + K_2 z^2 + K_3 z^3 + K_4 z^4 + K_5 z^5 + K_6 z^6$	[103]
6	$OCV(z) =$	$K_0 + K_1 \frac{1}{1+e^{\alpha_1(z-\beta_1)}} + K_2 \frac{1}{1+e^{\alpha_2(z-\beta_2)}}$	Proposed
		$+K_3 \frac{1}{1+e^{\alpha_3(z-1)}} + K_4 \frac{1}{1+e^{\alpha_4 z}} + K_5 z$	Model

The new OCV model is compared in this section with the five different models

summarized in Ref. [81], where the polynomial model is reported to be the most accurate. All the parameters in those five OCV models are refitted for the data presented in Fig. 3.1 using Matlab curve fitting toolbox, the results with their rms and maximum errors are shown and summarized in Fig. 3.3 and Tab. 3.2. It should be noted that none of the five OCV models is suitable for IC analysis, as their model structures do not take into account the staging mechanism in intercalation/deintercalation process. One can see that the new OCV model proposed in Eq. 3.1 has better fitting accuracy than all those five models. Consequently, improvement in the SOC estimation results may also be expected when the new OCV model is incorporated.

Table 3.2: Fitting results of OCV models from Tab. 3.1

Model #	RMS Error (mV)	Max Error (mV)
1	5.2	12.6
2	3.1	8.9
3	5.6	21.3
4	4.7	12.7
5	2.1	7.3
6	1.0	2.5

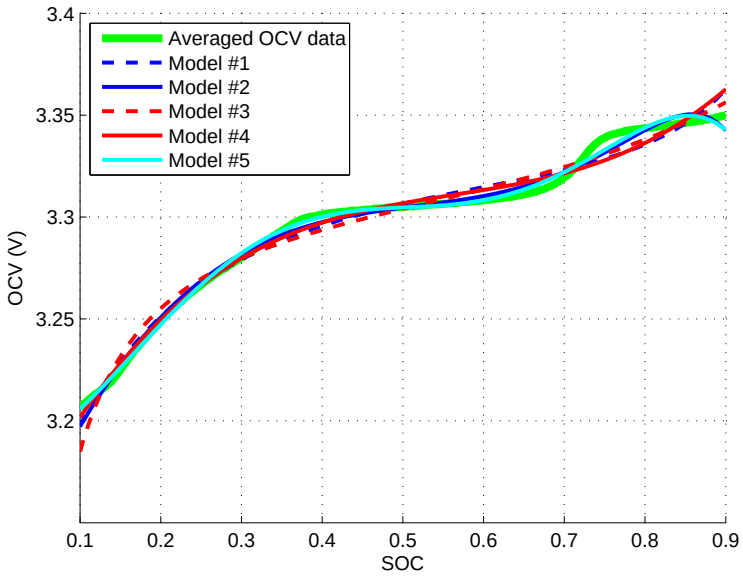

Figure 3.3: Comparison of OCV fitting results.

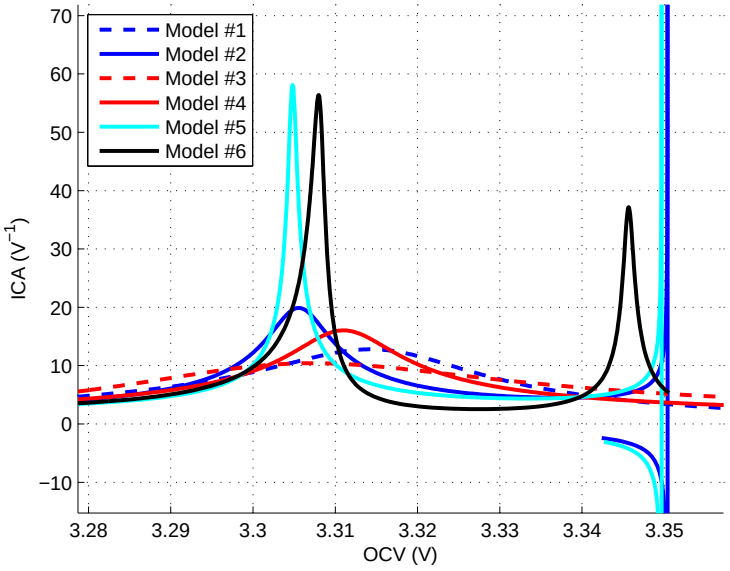

Figure 3.4: Comparison of IC curves from fitted OCV.

The IC curves based on different OCV models are shown in Fig. 3.4. It can be observed that the new model (model #6) captures the two IC peaks associated with staging, whereas all other models only show one peak on the IC curves. Since the signature of different peaks are associated with different aging mechanism, model #6 can extract more aging information from the OCV data compared to other models and will be used for further analysis in SOH monitoring. For models #2 and #5, $\mathrm{d}Q/\mathrm{d}V$ is not defined at 3.35 volt because of a singularity in the math expression. Consequently, spikes in both directions are shown in Figure 5 for the two IC curves, corresponding to models #2 and #5.

3.2 State-of-Charge Estimation Based on Extended Kalman Filter

The extended Kalman filter (EKF) based approach discussed in Ref. [24] is used to illustrate the implementation of the new OCV model for SOC estimation. The battery test data for this study is collected through the experimental set-up introduced in

Ref. [99] and the first-order RC model [104] is used for calculating the SOC with the following algorithm:

$$
\begin{aligned}
&\text{RC Model:}\\
&z_{k+1} = f(z_k, I_k) + w_k,\\
&V_k = g(z_k, I_k) + v_k,\\
&\text{EKF Algorithm:}\\
&A_{k-1} = \left.\frac{\partial f(z_{k-1}, I_{k-1})}{\partial z_{k-1}}\right|_{z_{k-1}=\hat{z}_{k-1}},\\
&C_k = \left.\frac{\partial g(z_k, I_k)}{\partial z_k}\right|_{z_k=\hat{z}_{k|k-1}},\\
&\hat{z}_{k|k-1} = f(\hat{z}_{k-1}, I_{k-1}),\\
&P_{k|k-1} = A_{k-1}P_{k-1}A_{k-1}^T + Q,\\
&G_k = P_{k|k-1}C_k^T\left[C_kP_{k|k-1}C_k^T + V\right]^{-1},\\
&\hat{z}_k = \hat{z}_{k|k-1} + G_k\left[V_k - g(\hat{z}_{k|k-1}, I_k)\right],\\
&P_k = \left[\mathbf{I} - G_kC_k\right]P_{k|k-1},\\
&\text{where}\\
&f(z_k, I_k) = z_k - (\frac{\eta_i\Delta t}{Q_c})I_k,\\
&g(z_k, I_k) = OCV(z_k) + V_{rc,k} + R_0I_k,\\
&V_{rc,k+1} = \exp(\frac{-\Delta t}{R_1C})V_{rc,k} + R_1[1 - \exp(\frac{-\Delta t}{R_1C})]I_k,
\end{aligned}
\tag{3.2}
$$

z_k is the SOC, η_i is the charging/discharing efficiency, Δt is the time step, Q_c is the battery capacity, I_k is the input current, V_k is the total terminal voltage, $V_{rc,k}$ is voltage of the RC circuit, R_0, R_1 and C are battery internal resistance and capacitance, Q is the error covariance of process noises, and V is the error covariance of observation noises [99]. The OCV function is represented by the model given by Eq. (3.1).

In this study, all the parameters in the RC model are set to be constants without

performing iterative optimizations as discussed in Ref. [81].

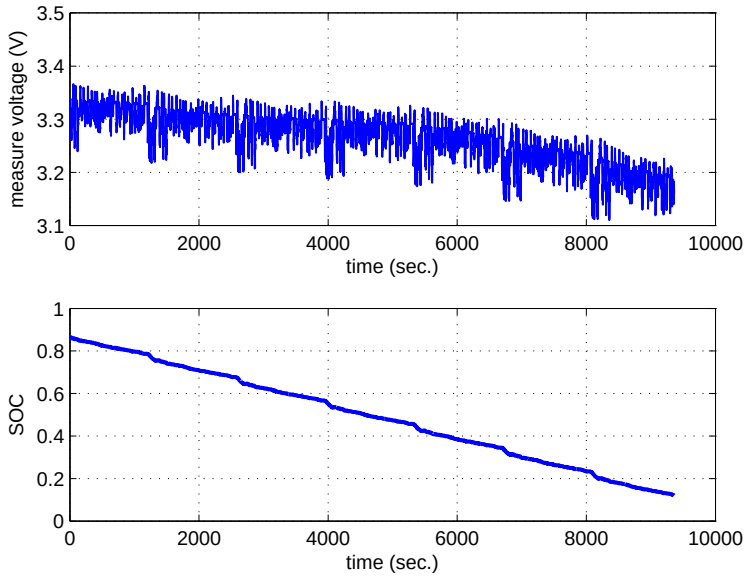

Figure 3.5: Battery data tested under FUDS.

The battery data collected under the Federal Urban Driving Schedule (FUDS) is shown in Fig. 3.5. As in Ref. [24], the SOC data obtained by Coulomb counting in the Arbin battery test bench, where high precision current sensor is used, is assumed to be the "true" SOC and used as a reference for performance evaluation. Therefore the SOC estimation error is defined as,

$$e_{SOC,k} = \hat{z}_k - z_k \tag{3.3}$$

where $e_{SOC,k}$ is the SOC estimation error, $\hat{z}_k$ is the SOC estimated by the EKF algorithm and z_k is the reference SOC calculated from the measured data. Please note that the SOC from Arbin Coulomb counting, while representing the best reference that we can get, is only approximately accurate due to the unavoidable error and integral accumulation of the error in the current measurement [24].

The model parameters used in the EKF-based SOC estimation are shown in Tab. 3.3.

Table 3.3: Parameters of models #5 and #6 used in SOC estimation

Model Parameters	Model #5	Model #6
K_0	3.0896	3.4002
K_1	1.1627	0.0080
K_2	-2.3821	0.0785
K_3	2.1870	-0.2150
K_4	-0.5444	-1.3032
K_5	-0.1939	0.0891
K_6	0.0582	N/A
α_1	N/A	-14
α_2	N/A	-18
α_3	N/A	28
α_4	N/A	40

Table 3.4: Parameters of EKF based SOC estimator

Parameters	Values
Error covariance of process noises, Q	$\begin{pmatrix} 0.15 & 0 \\ 0 & 1 \end{pmatrix}$
Error covariance of observation noises, V	0.01

A detailed description of the EKF algorithm can be found in both Refs. [24] and [81]. The parameters of the EKF (i.e., V and Q used in Eq. 3.2) are calibrated using the data collected in our aging tests, and the same parameters (listed in Tab. 3.4) are used in the performance evaluation for the new model (#6) and the polynomial model (#5).

Figure 3.6 displays the EKF based SOC estimation results. The two plots represent two cases with different initial SOC error (+10% and -10%, respectively). One can see that the estimated SOC converge into the 5% estimation error bound when either model #5 or #6 is used. In particular, with positive initial error, the SOC estimated with model #6 converges much faster than the SOC estimated with model #5. This difference in convergence rate with positive initial error can be explained by the curve fitting results shown in Figs. 3.2 and 3.3, where model #6 has better accuracy than #5 in the high SOC region. On the other hand, both models have

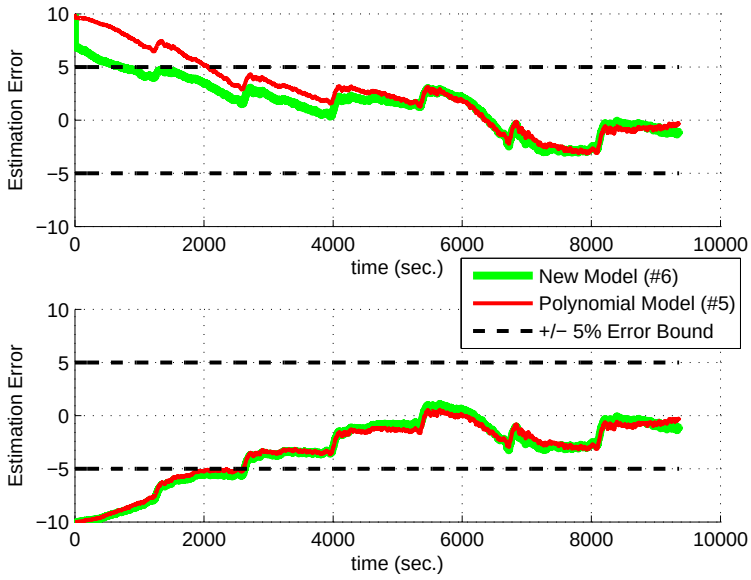

Figure 3.6: SOC estimation with OCV model #6.

approximately the same accuracy when SOC is below 70% and therefore have similar convergence rate with negative initial error. The 5% error bound can be achieved with other initial error (e.g., 20% or 30%).

In summary, the new OCV model, when used for EKF-based SOC estimation, outperforms other OCV models under the conditions we tested. The model delivers accurate estimation results with less than 5% errors without extensive calibration and training. The results presented in this section demonstrates the potential of implementing this new OCV model for SOC estimation problems.

3.3 State-of-Health Monitoring Based on Incremental Capacity Analysis

Even though ICA was originally proposed for "close-to-equilibrium" conditions, it was shown in Ref. [16] that, for normal charging data, the peaks on the IC curve can also be identified and they reveal significant information about battery SOH. Hence, the results presented in this section for ICA are all based on 0.5C battery charging

data (same as in Ref. [16]). It will be shown that the proposed parametrization is applicable to both OCV data and normal charging data (i.e., charged at 0.5C).

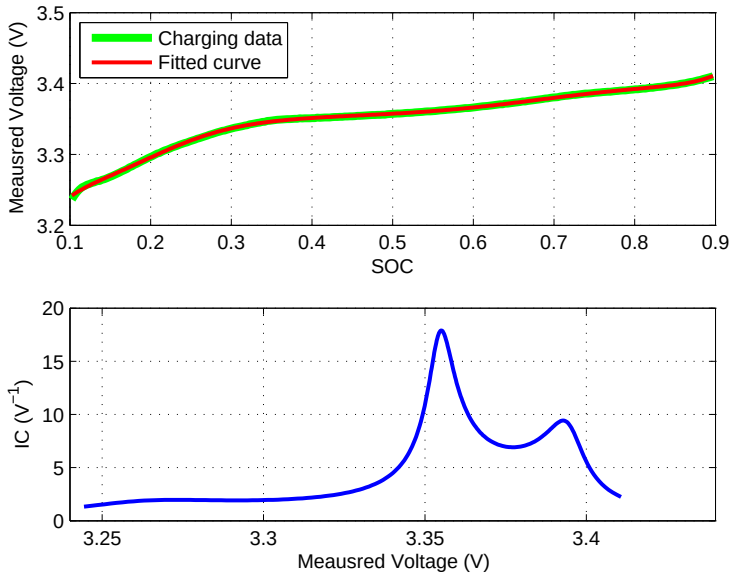

Figure 3.7: V-SOC and IC curve from 0.5C charging data.

As shown in Fig. 3.7, we can obtain the IC curve directly by differentiating the analytical V-SOC function and then taking the reciprocal.

3.3.1 Incremental Capacity Analysis Results at Different Aging Stages

The IC curves of battery charging data collected at different aging cycles under 35^oC environment condition are shown in Fig. 3.8. The numerical values in the plot legends represent the aging cycle number. The IC peaks highlighted by the circle in Fig. 3.8 clearly shows a monotonic decreasing trend as a battery ages, which implies a battery degradation that is mainly related to the loss of active material at the graphite anode [32, 35].

The IC curves from four different cells are plotted in Fig. 3.9, where the plots focus on the second peak on the IC curve and depict a consistent trend in capacity fading as reflected by the decreasing IC peaks.

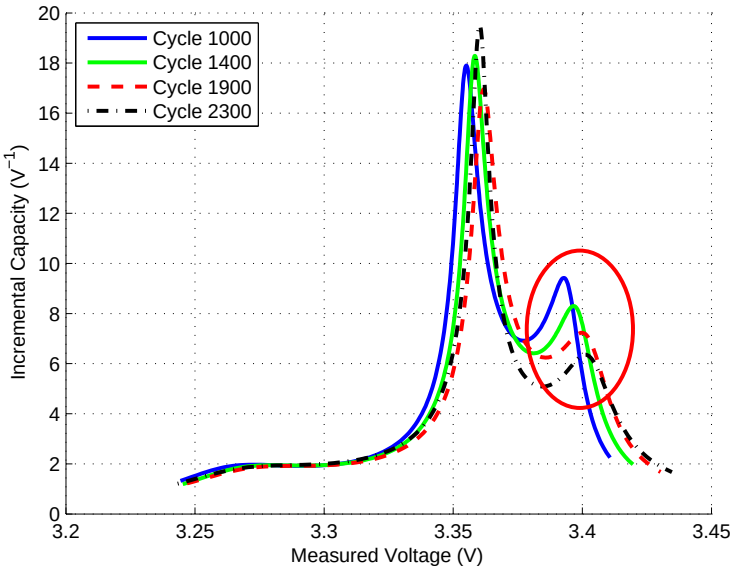

Figure 3.8: IC curves of data at different aging stages at 35^{o}C.

To obtain the correlation between the cell capacity fading and IC peak, the peak values of eight cells at different aging stages are identified. The normalized peak values of one of the cells (red dots in Fig. 3.10) are correlated with the faded cell capacities, and used to construct the battery capacity estimation curve (red dashed curve in Fig. 3.10) as done in Ref. [16]. The data from other cells are also plotted to verify the prediction capability of the estimation curve. The result shows the new parametric model in the form of Eq. (3.1) can be used for capacity based battery SOH monitoring with good accuracy.

3.3.2 Incremental Capacity Analysis Results at Different Temperature

Test data were also collected at different temperatures throughout the battery aging process. ICA was performed with respect to different temperatures to evaluate and confirm the sensitivity to temperature and results are presented in Fig. 3.11. The intensities of the IC peaks reduce as temperature drops, which could be attributed to the slow lithium-ion diffusion or lithium plating phenomenon at low temperature as elucidated in Ref. [17]. When the temperature is too low, say at 10^oC, the second

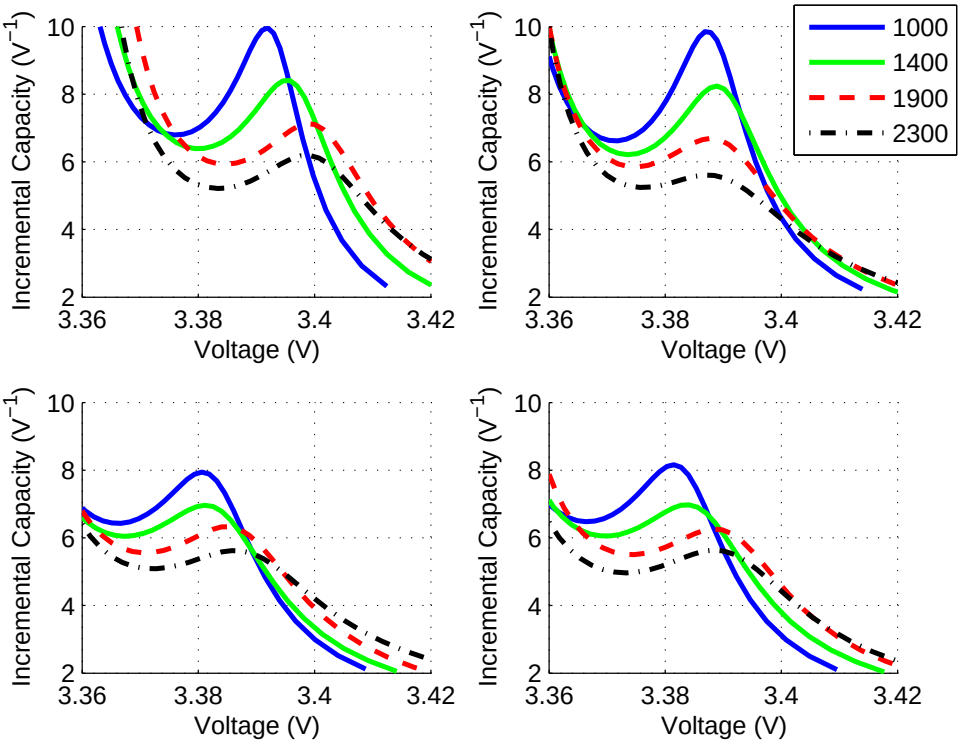

Figure 3.9: IC curves comparison from four different cells at 35^{o}C.

peak could disappear from the IC curve. However, since the operating temperature of battery systems are usually maintained through integrated thermal control in the BMS, the disappearance of IC peaks at low temperature should not be a concern.

Figure 3.12 presents the IC curves at different temperature at different aging stages. A temperature dependence of the IC peaks and the model parameters may be evaluated. The first peak on these four plots shows consistent temperature sensitivity while the second peak shows the aging status. It suggests that the test data corresponding to higher temperature will be more reliable for ICA and capacity fading identification. Therefore, even though the temperature dependence is not parametrized explicitly, the proposed model is capable of capturing the influence of temperature difference by adapting all parameters.

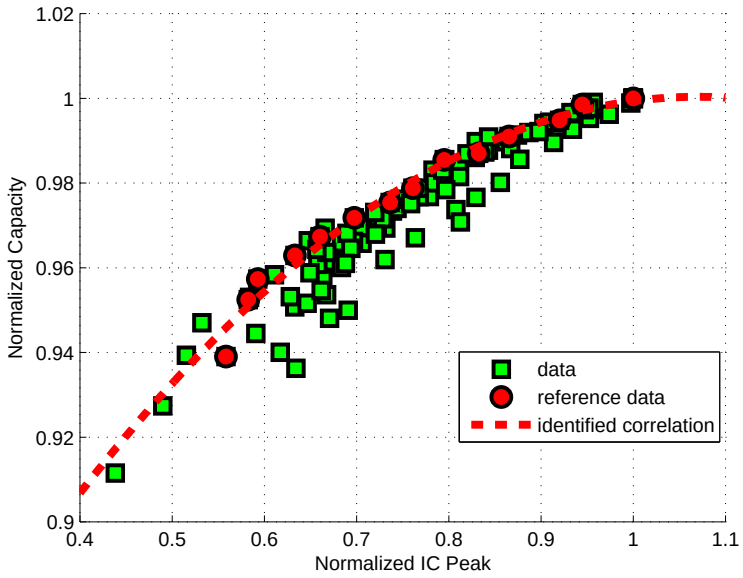

Figure 3.10: Correlation between faded battery capacity and IC peak values at 35^{o}C.

3.4 Other Signatures on the Incremental Capacity Curve and Their Correlation with Capacity Fading

Other than using the IC peak value decreasing as the indication of battery capacity fading, we also explore a different approach that uses the IC peak locations to evaluate the degradation. Since the IC peaks represent the phase transitions during the intercalaction/deintercalation process and this electrochemical reaction is affected by battery capacity loss, the locations of the peaks might also have a correlation with the faded capacity and can give a good estimation of the loss.

Consider the IC as a function of SOC (rather than measured voltage), as shown in Fig. 3.13. Note that the first IC peak stays at approximately the same location whereas the second peak is moving toward the left as the battery ages and capacity decreases. By normalizing both the second IC peak location and battery capacity, we obtain the correlation between the two values in Fig. 3.14 , which confirms that the location of the second IC peak could also be a indication of battery capacity fading.

However, in order to accurately measure this peak location in terms of charged

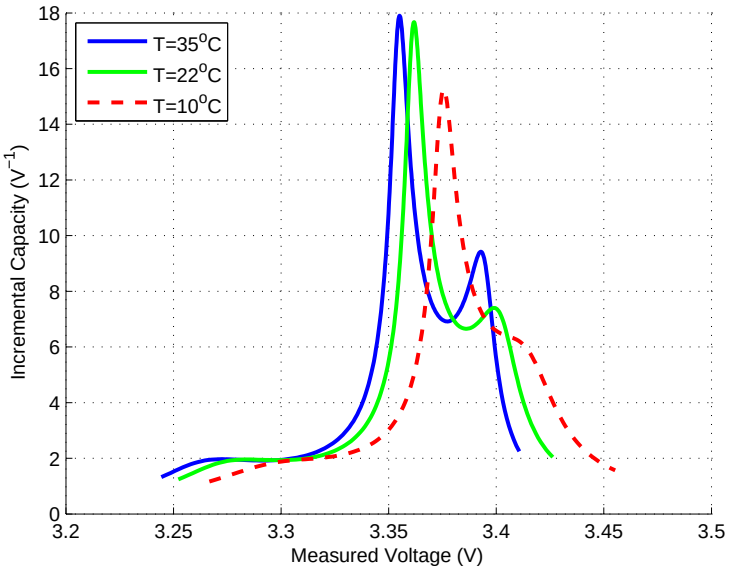

Figure 3.11: IC curves of data at different temperature.

capacity, it is required to start the battery charging from zero SOC, which is not always practical in real operation. This problem can be addressed by using the SOC span between the two consecutive IC peaks,

$$d_{IC} = P_2 - P_1 \tag{3.4}$$

where d_{IC} is the SOC interval between two consecutive peaks, and P_1 and P_2 are the locations of the two IC peaks, respectively. The value of d_{IC} is more easily obtainable as long as the charging starts below the SOC value that corresponds to the first IC peak. Typically, the first peak on the IC curve appears around SOC=0.45. Therefore, for all the data we have, this condition is satisfied as long as the charging covers 40% to 85% SOC. The plot with normalized d_{IC} and battery capacity is shown in Fig. 3.15. This correlation obtained using d_{IC} is looser than using P_2 only, as the values of both P_1 and P_2 are affected by measurement noise and the value of d_{IC} is more susceptible to noise and modeling error.

The analysis suggests that the signatures on the IC curves, namely the second

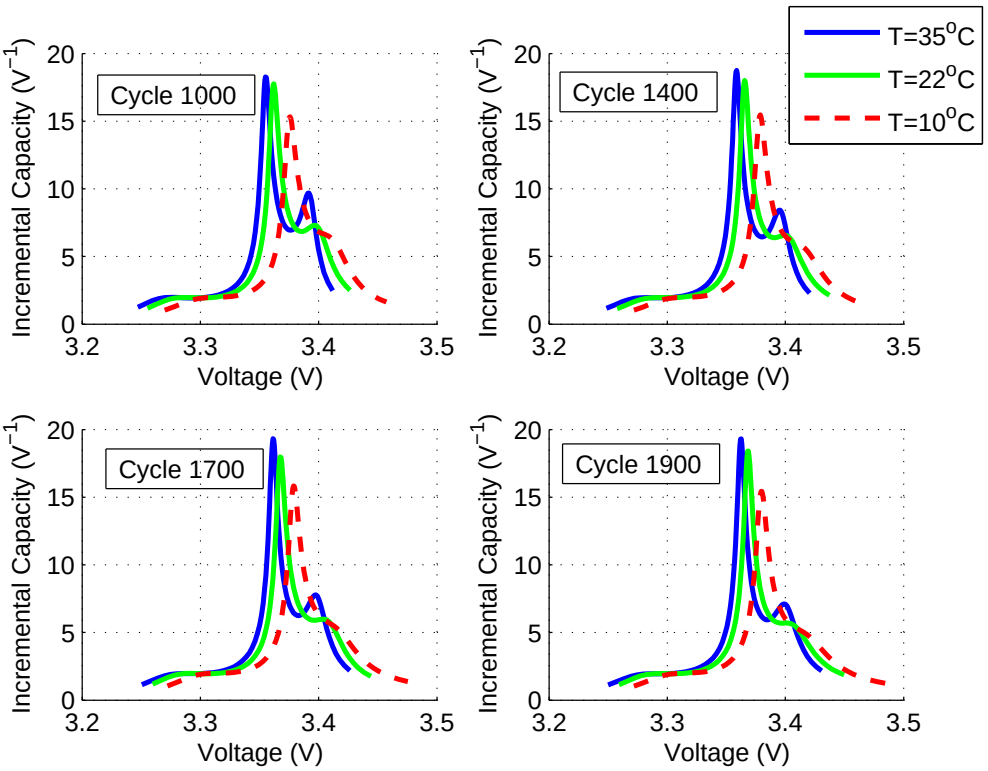

Figure 3.12: IC curves of data at different temperature and ages.

IC peak and the distance between two peaks, can be used as indicators for battery aging. The two correlations based on IC peak locations are not as strong and robust compared to the results based on peak values shown in Fig. 3.10. Nevertheless, we believe that those correlations can provide useful information for battery SOH monitoring from different perspectives. It is also possible to improve the peak location based results when more accurate current sensors are available.

3.5 Parametric Analysis and Model Simplification

Although the identification results using the new OCV model has shown its effectiveness, the high number of parameters and nonlinearity of the model may present a challenge for on-board implementation. A parametric analysis is performed to characterize the correlations between model parameters and battery aging, evaluate the

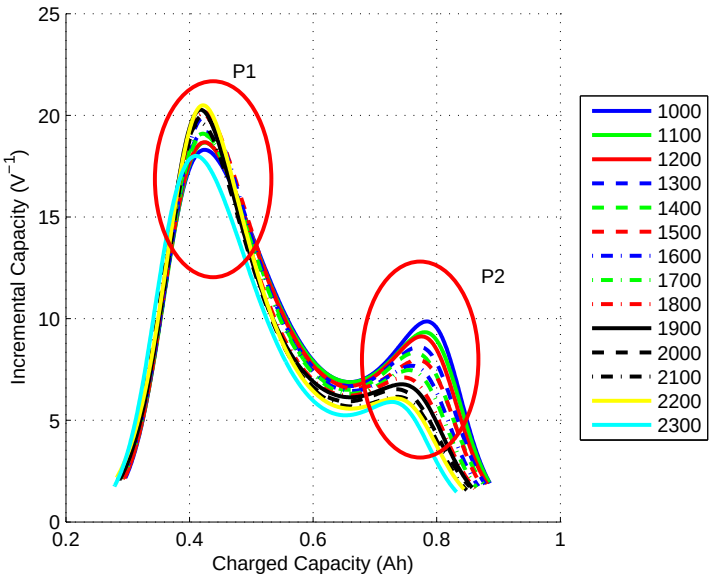

Figure 3.13: IC curve plotted versus charged capacity data at 35^{o}C.

sensitivity and robustness of the model structure, and better understand the utility of the proposed model. Moreover, the analysis results may help to identify the significance of each parameter and simplify the model, so that the computational efficiency in estimation can be improved.

Consider the following function, which is derived by differentiating OCV with respect to the battery SOC,

$$\begin{aligned} G(z) =& \frac{d}{dz}OCV(z) = -K_1\frac{\alpha_1 e^{\alpha_1(z-\beta_1)}}{(1+e^{\alpha_1(z-\beta_1)})^2} \\ & - K_2\frac{\alpha_2 e^{\alpha_2(z-\beta_2)}}{(1+e^{\alpha_2(z-\beta_2)})^2} - K_3\frac{\alpha_3 e^{\alpha_3(z-\beta_3)}}{(1+e^{\alpha_3(z-1)})^2} \\ & - K_4\frac{\alpha_4 e^{\alpha_4(z-\beta_4)}}{(1+e^{\alpha_4 z})^2} + K_5. \end{aligned} \tag{3.5}$$

Note that the IC curve is the inverse of $G(z)$, the locations and values of IC peaks may be calculated by letting the derivative of $G(z)$ equal to zero and solving the resulting algebraic equation. The resulting equation, however, is highly nonlinear and cannot be easily solved analytically in general. Here, an alternative approach that

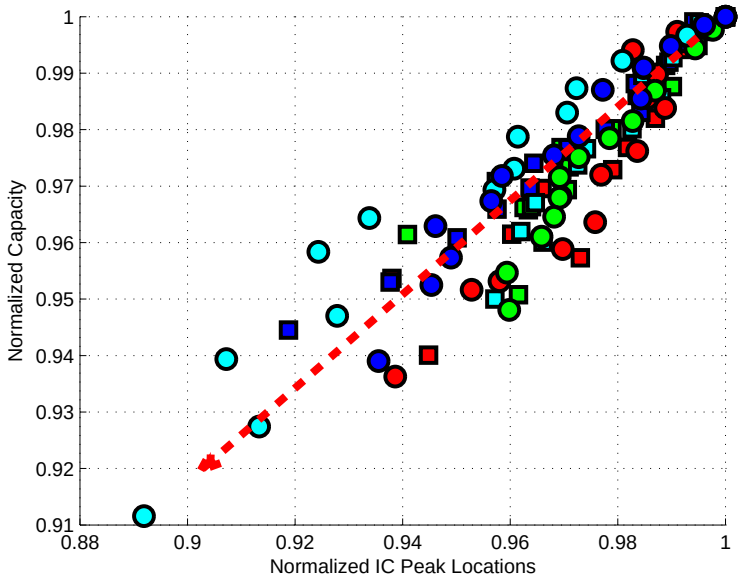

Figure 3.14: Correlation between IC peak locations and battery faded capacities (data from different cells are color coded differently).

separates and analyzes the terms in the Eq. (3.5) individually is used to correlate the model parameters and the solution of $G(z)$.

To understand the contribution of each term of (3.5), we first define the following,

$$\begin{aligned} f_1(z) &= -K_1 \frac{\alpha_1 e^{\alpha_1(z-\beta_1)}}{(1+e^{\alpha_1(z-\beta_1)})^2}, \\ f_2(z) &= -K_2 \frac{\alpha_2 e^{\alpha_2(z-\beta_2)}}{(1+e^{\alpha_2(z-\beta_2)})^2}, \\ f_3(z) &= -K_3 \frac{\alpha_3 e^{\alpha_3(z-1)}}{(1+e^{\alpha_3(z-1)})^2}, \\ f_4(z) &= -K_4 \frac{\alpha_4 e^{\alpha_4(z)}}{(1+e^{\alpha_4 z})^2}. \end{aligned} \tag{3.6}$$

Through analytical and numerical analysis, we have the following observations:

- f_2 and f_4 decay to zero at the high SOC range, where the IC peak of interest occurs. Therefore, they do not contribute to the IC peaks and their locations. Our analysis will be focused on f_1 and f_3;

- The parameter K_5 is a constant and therefore it does not need to be considered

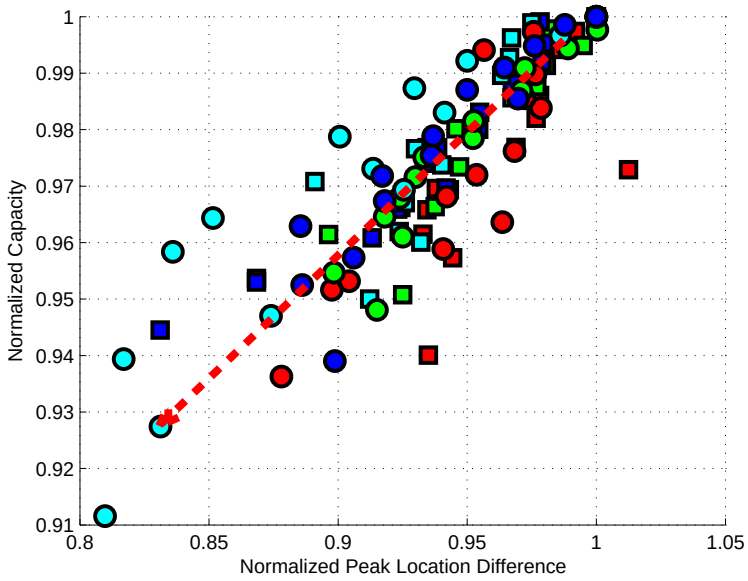

Figure 3.15: Correlation between IC peak location difference and battery faded capacities (data from different cells are color coded differently).

here;

- Numerical results show that K_1 and K_3 do not vary much compared to α_1 and α_3;

- Our analysis show that the IC peak has about equal sensitivity to α_1 and α_3. The sensitivity analysis is performed by numerically evaluating the partial derivative of the IC function, defined by $\frac{1}{G(z)}$ with $G(z)$ given by (3.5), with respect to the parameters α_1 and α_3 at the z value where the second IC peak is located.

With the above observations, we identified a simplified model in the following form:

$$\begin{aligned} OCV(z) =& K_1 \frac{1}{1+e^{\alpha_1(z-\bar{\beta}_1)}} + K_3 \frac{1}{1+e^{\alpha_3(z-1)}} \\ &+ \bar{K}_0 + \bar{K}_2 \frac{1}{1+e^{\bar{\alpha}_2(z-\bar{\beta}_2)}} + \bar{K}_4 \frac{1}{1+e^{\bar{\alpha}_4 z}} + \bar{K}_5 z. \end{aligned} \tag{3.7}$$

where the model structure contains only 4 changing parameters (i.e., K_1, K_3, α_1 and α_3), and other parameters can be estimated only once when the batteries are fresh and kept constants as batteries age.

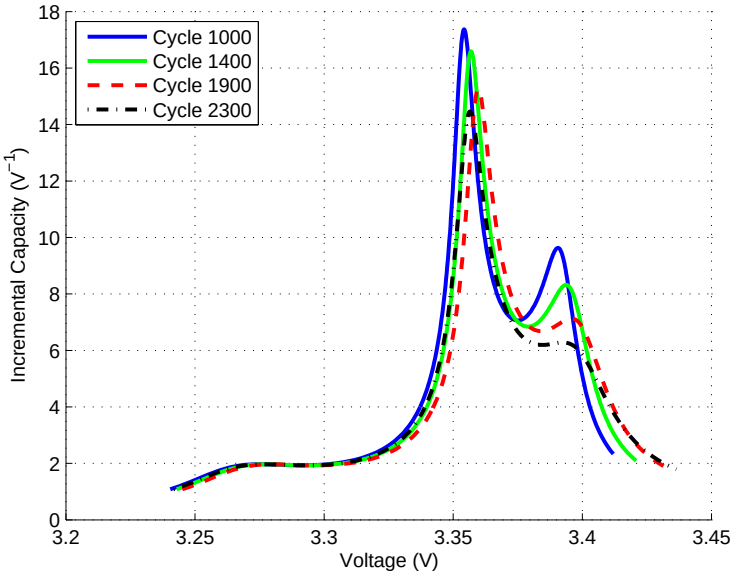

Figure 3.16: IC curves obtained using simplified OCV model at 35^{o}C.

Table 3.5: Comparison of fitting accuracy measured by RMS error between full and simplified model

Cycle #	Full Model (mV)	Simplified Model (mV)
1000	0.760	0.805
1400	0.925	0.980
1900	0.946	1.247
2300	1.024	1.559

In Fig. 3.16, one can see that the IC curves obtained using the simplified OCV model show qualitatively the same trend as the ones obtained by the full model (see Fig. 3.8) when the battery ages. Table 3.5 shows the comparison of fitting accuracy between the full and the simplified model. In the worst case, the rms error is less than 2 mV. Therefore, the simplification preserves the high fitting accuracy provided by the full model.

Table 3.6: Parameters of the simplified OCV model

Cycle #	α_1	K_1	α_3	K_3
1000	-12.57	0.0446	25.9352	-0.2459
1400	-12.29	0.0467	23.2749	-0.2435
1900	-11.57	0.0497	20.4778	-0.2413
2300	-11.4	0.0531	18.5991	-0.2447

The parameters for the simplified model are listed in Tab. 3.6, where one can see the variations in α_1 and α_3 agree with our parametric analysis. Moreover, it suggests that the values of the deteriorating peaks in the IC curves might be estimated directly from the parameters with the following relationship,

$$q = \theta_0 + \theta_1\alpha_1 + \theta_2 K_1 + \theta_3\alpha_3, \tag{3.8}$$

where q, defined as $q = \frac{p-p_0}{p_0}$, represents the amount of degradation, p represents the IC peak values, and p_0 is the initial peak value. $\theta_{0\sim3}$ are the identification parameters in this equation. K_3 is not included in this equation as it is insensitive to the variation of IC peak values. Same as our analysis in subsection 3.3.2, the values of parameters $\theta_{0\sim3}$ depend on the operating temperature. For on-board battery SOH diagnosis, thermal control should be integrated as part of the BMS. Therefore, consistent temperature could be expected when the SOH monitoring is performed.

Given a set of n data points, p_i, α_{1i}, K_{1i}, α_{3i}, $i = 1, ..., n$, from one battery cell at different aging stages, the values of $\theta_{0\sim3}$ can be easily calculated from the least

squares method,

$$\theta = (\Phi^T \Phi)^{-1} \Phi^T q,$$

where

$$\begin{aligned} \theta &= [\theta_0, \theta_1, \theta_2, \theta_3], \\ \Phi &= [\phi_1, \phi_2, ..., \phi_n]^T, \\ q &= [q_1, q_2, ..., q_n]^T, \\ \phi_i &= [1, \alpha_{1i}, K_{1i}, \alpha_{3i}]^T. \end{aligned} \tag{3.9}$$

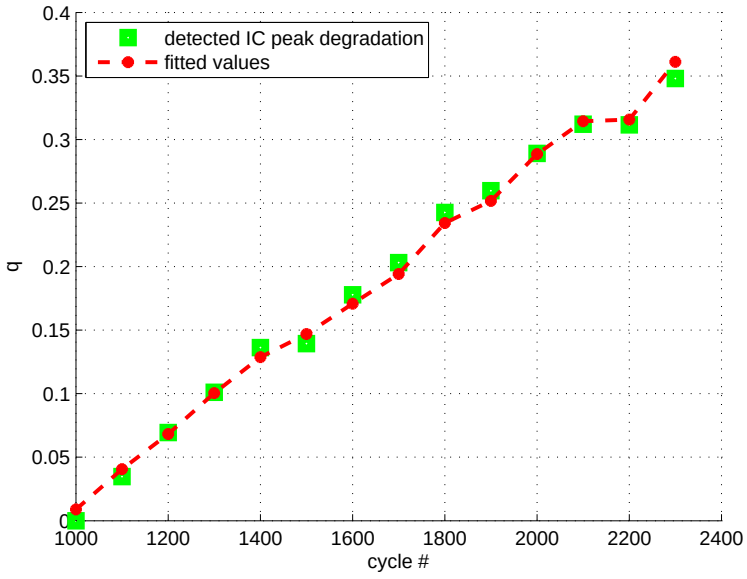

Figure 3.17: Identification results of (3.8) using battery testing data from one single cell.

The identification results of (3.8) are very accurate as shown in Fig. 3.17, where the battery testing data of one single cell (denoted as cell A) at all different ages are included.

To use the model (3.8) identified from cell A to 7 other cells, one can use $\theta_{1\sim3}$ directly while adjusting θ_0 such that the value of q given by (3.8) at the initial stage is zero. Figure 3.18 show that the data from two other cells, as an example, can

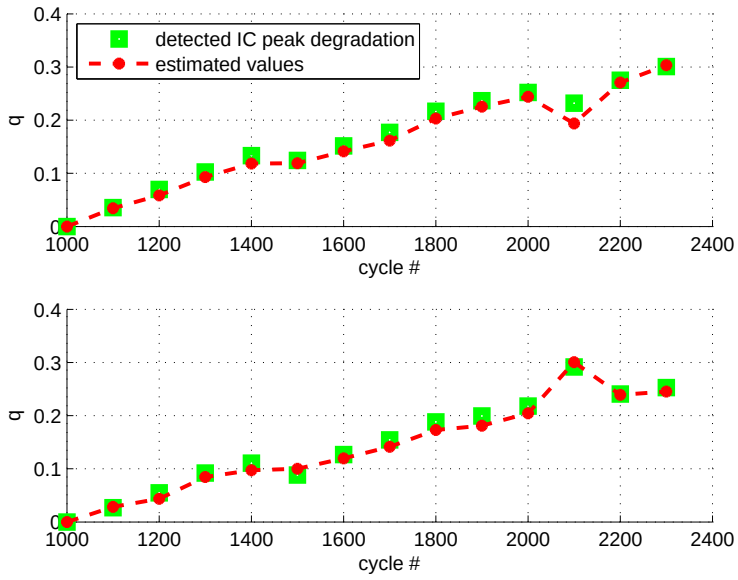

Figure 3.18: Verification of (3.8) using parameters $\theta_{1\sim3}$ identified from Fig. 3.17 with data from two other cells.

also be fitted accurately by applying $\theta_{1\sim3}$ without further identification effort. In other words, the IC peak values of different cells can be estimated/predicted based on the parameters $\theta_{1\sim3}$ identified from one reference cell. Therefore, it is possible to perform battery SOH monitoring directly using (3.8) without numerically deriving the IC curves.

As shown in Fig. 3.19, the results from Figs. 3.10 and 3.17 can be combined so that the battery capacity fading can be directly predicted using the parameters of the simplified OCV model. One can see that 50% reduction in IC peak value is equivalent to about 10% battery capacity loss.

To summarize, the simplified OCV model with reduced number of varying parameters is capable of capturing the battery aging features with fewer parameters, thereby improving the identification efficiency and making the model implementable in on-board BMS. With the established linear relationship between the IC peak values and the OCV model parameters in (3.8), the battery aging information can be revealed by only looking at the changing parameters in the OCV representation (3.7).

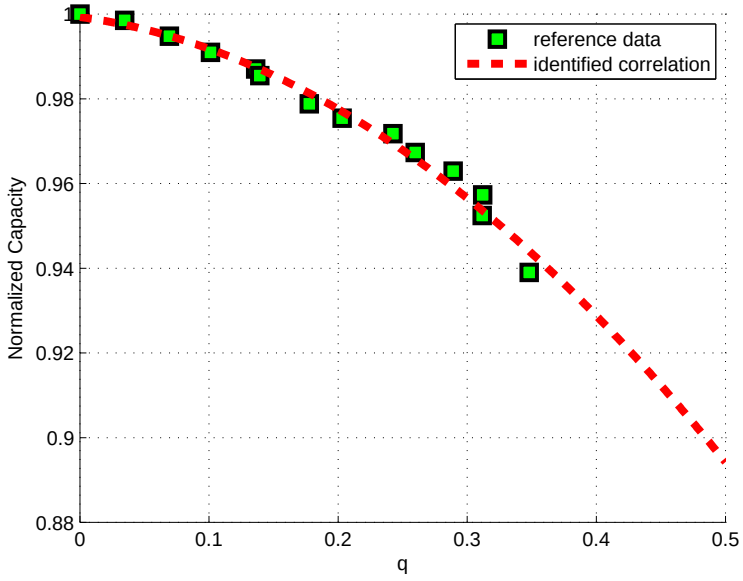

Figure 3.19: Correlation between capacity fading and IC peak reduction.

CHAPTER IV

Non-Parametric Approaches for Battery State-of-Health Monitoring

In this chapter, we explore the use of non-parametric approaches to process battery voltage data and apply incremental capacity analysis (ICA) on-board. Compared to parametric models, whose number of parameters are typically fixed, the number of parameters in a non-parametric model usually depends on the properties of the given data set. Among the several algorithms that are developed to extract the battery aging signature through ICA, the use of support vector regression (SVR) is shown to provide the most consistent identification results with moderate computational load. For battery cells tested, the SVR model built upon the data from one single cell is able to predict the capacity fading of 7 other cells within 1% error bound.

4.1 Incremental Capacity Analysis Results Using Conventional Data Processing and Curve Fitting Methods

As mentioned in previous chapters, the updated OCV curve is not available during real-life operation, the ICA has to therefore rely on the vehicle charging data, which gives the charging voltage (V-Q) curve. Applying numerical derivative directly to the data is the most intuitive approach, given the definition of IC. Because the mea-

surement noise has a rather big influence on the flat portion of the charging voltage curve, judicious data processing is required before numerical differentiation can be performed.

4.1.1 Numerical Differentiation with Smoothing

In this section, the raw data curve is fitted with a 3^{rd} order polynomial curve piecewisely with a moving window. The derivative of the middle point of each window is recorded. The resulting derivative curve is then smoothed by averaging. The results are shown in Fig. 4.1. There are three noticeable peaks in the plot, which agrees with the results shown in [35]. The peaks are associated with the staging process in the negative electrode as discussed in [32, 36, 72]. The peak at higher voltage gives a clearly decreasing trend as battery ages (shown in Fig. 4.2) and is thereby selected for further study.

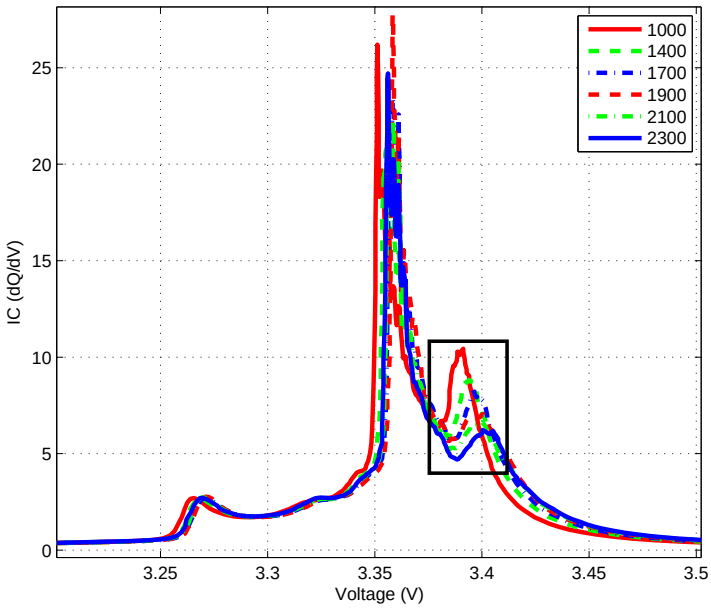

Figure 4.1: Comparison of IC curves obtained by numerical derivative.

Although the numerical derivative results do yield a clear monotonic change on the IC peaks, the resulting IC curves are not differentiable and therefore not suitable

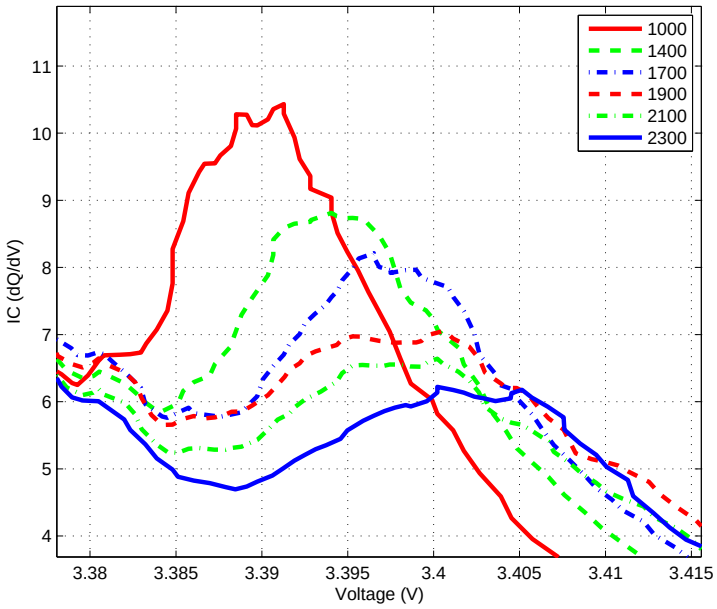

Figure 4.2: Zoom-in of the numerically derived IC curves.

for further quantitative analysis. In addition, the data processing procedure is time-consuming and thus not computationally efficient. Nonetheless, the numerical results identify the range where the relevant peaks appear and therefore a local polynomial curve can be fitted. The polynomial fitting results are discussed in the next subsection.

4.1.2 Polynomial Curve Fitting

The charging data around the main voltage plateaus (e.g., ranging from $0.45Ah$ to $0.85Ah$ for the battery of nominal capacity $1.1Ah$) is selected for the analysis. Because the selected data only contains two IC peaks at the higher voltage range as shown in the previous subsection and Fig. 4.1, a 5^{th} order polynomial (which can represent exactly two peaks) is chosen to be fitted with the charging data and then differentiated for ICA. Two ICA peaks can be observed on the IC curve. Same as before, the value of the peak at higher voltage is recorded for analysis. An illustration of this method is shown in Fig. 4.3 and a comparison of the curves involving aging effect is plotted in Fig. 4.4.

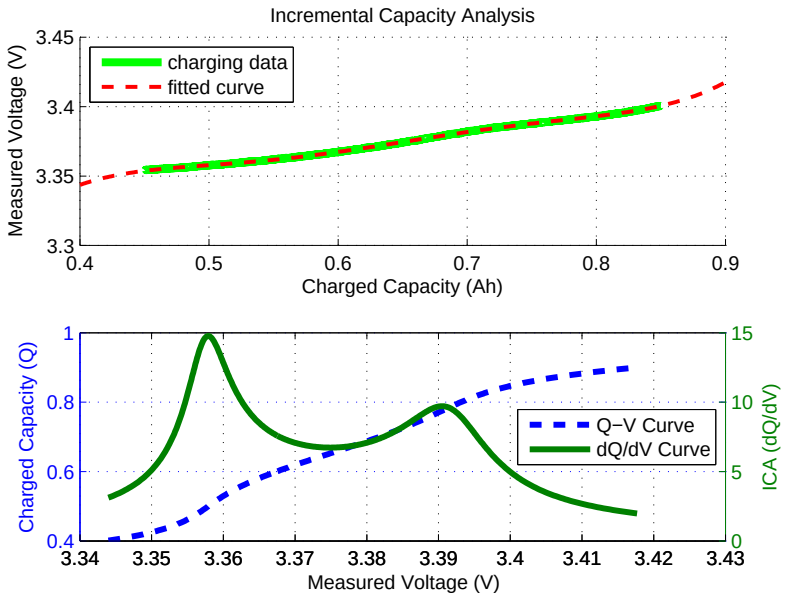

Figure 4.3: IC curve obtained by polynomial fitting.

Polynomial curve fitting gives much smoother IC curves compared to the ones by numerical differentiation. However, our analysis reveals an unacceptably high sensitivity of the results to the selected data range. As shown in Fig. 4.5, the shape of the IC curve may change significantly when a slightly different data range is used for the fitting. A more robust method for ICA is thus needed.

The correlation between faded battery capacity and IC peaks obtained from the above two methods are displayed in Fig. 4.6. Both methods lead to 2^{nd} order correlations between the faded capacity value and the corresponding IC peak value. Although quantitatively the two methods give different results, the qualitative relationships are the same.

4.2 Incremental Capacity Analysis Results Obtained by Support Vector Based Methods

The support vector algorithm is a nonlinear generalization of the Generalized Portrait algorithm developed by Vapnik et al. in the sixties [83]. SVR adopts the

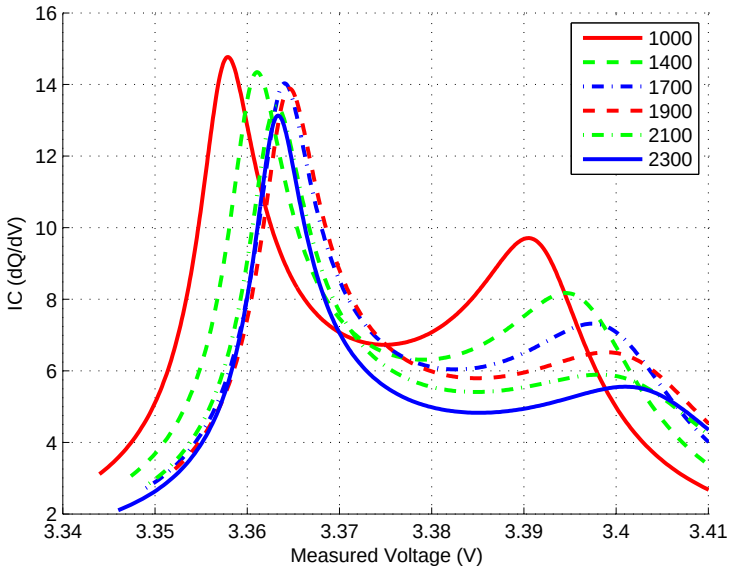

Figure 4.4: Comparison of polynomial fitted IC curves for different cycles.

original machine learning algorithm and applies it for non-parametric function estimation. Conventional SVR is formulated as a convex quadratic programming (QP) problem and has been successfully applied in identifying nonlinear dynamic systems [105]. However, the implementation of QP-SVR is computationally expensive and sufficient model sparsity cannot be guaranteed. A linear programming (LP) based SVR, that employs ℓ_1 norm as the regularizer, was then proposed to improve the model sparsity and computational efficiency [106, 107]. SVR is chosen for this study because of its excellent approximation and generalization capability, and its demonstrated potential in the realm of nonlinear system identification [105, 106, 108].

4.2.1 Incremental Capacity Analysis Results Obtained by Support Vector Regression

Since we are only interested in obtaining the IC (dQ/dV) curve, we decide to use SVR to fit the reverse of charging curve (Q-V). The kernel based Q-V model is

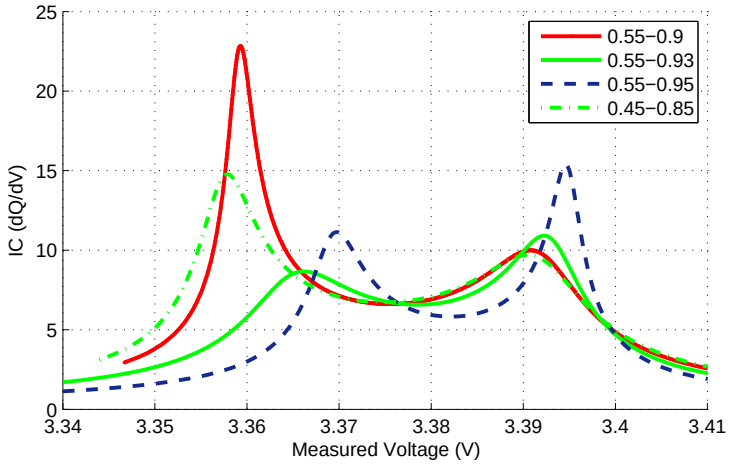

Figure 4.5: Comparison of polynomial fitted IC curves with different range of Q.

described by

$$\begin{aligned} y_n &= f(x_n) = \sum_{i=1}^{N} \beta_i k(x_i, x_n), \\ x_i &= v_i, \\ y_n &= q_n \end{aligned} \tag{4.1}$$

where x_n and y_n are model input and output, x_i is the base data point used for the kernel function, q is the battery charged capacity, v represents the measured voltage, N is the number of data points in the data set, β_i is the model parameters and $k(\cdot, \cdot)$ is the selected kernel. In this study, the Gaussian radial basis function (rbf) kernel is used and is expressed as

$$k(x, x') = \exp(\frac{-\|x - x'\|^2}{2\sigma^2}) \tag{4.2}$$

where σ is the adjustable parameter for the kernel function. The rbf kernel is the most generalizable kernel function for machine learning algorithms and it works very well with the IC curve identification. The parameters β_i in SVR are computed by an optimization algorithm.

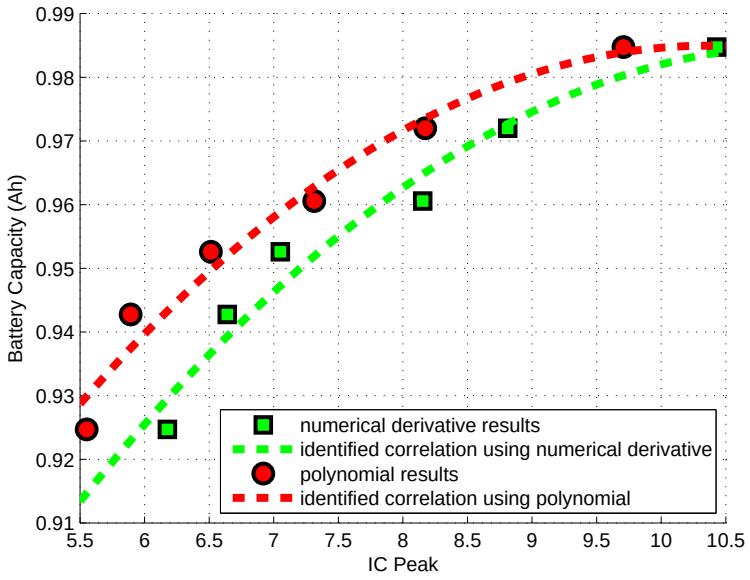

Figure 4.6: Correlation between faded capacity and IC peak by using V-Q data.

The SVR using ℓ_1 regularizer formulates the optimization problem as follows [106],

$$\min_{\boldsymbol{\beta},\, \mu,\, \boldsymbol{\xi}^+,\, \boldsymbol{\xi}^-} \quad \|\boldsymbol{\beta}\|_1 + w \sum_{n=1}^{N} \left(\xi_n^+ + \xi_n^-\right),$$
$$\text{subject to} \begin{cases} \sum_{i=1}^{N} \beta_i \mathcal{K}(x_i, x_n) + \mu - y_n \leq \varepsilon + \xi_n^+ \\ y_n - \sum_{i=1}^{N} \beta_i \mathcal{K}(x_i, x_n) - \mu \leq \varepsilon + \xi_n^- \\ \boldsymbol{\xi}^+, \boldsymbol{\xi}^- \geq 0 \end{cases} \tag{4.3}$$

where ξ_n^+ and ξ_n^- are the slack variables introduced to cope with the constraints in case they become over-constraining and make the optimization problem infeasible, w is the weighting factor, ε is the precision parameter, $\|\cdot\|_1$ denotes the ℓ_1 norm in coefficient space and $\boldsymbol{\beta}$ is defined as $\boldsymbol{\beta} = (\beta_1, ..., \beta_N)^T$. The optimal result usually gives zero value for most of the β_is, and the x_is corresponding to non-zero β_is are called support vectors (SVs) [83].

In this work, we used LP as the optimization engine to derive the SVR model. In order to establish the problem as an LP optimization, the coefficients β_is need to be

decomposed (using the property of linear piecewise convex function minimization) as [109],

$$\beta_i = \alpha_i^+ - \alpha_i^- \qquad |\beta_i| = \alpha_i^+ + \alpha_i^- \tag{4.4}$$

where α_i^+ and α_i^- are nonnegative and satisfy $\alpha_i^+ \cdot \alpha_i^- = 0$.

4.2.2 Formulation of Linear Programming Support Vector Regression

Following the derivation reported in [106], the SVR problem using ℓ_1 regularizer can be reformulated as an LP problem,

$$\begin{aligned} \min \quad & \mathbf{c}^T \begin{pmatrix} \boldsymbol{\alpha}^+ \\ \boldsymbol{\alpha}^- \\ \boldsymbol{\xi}^+ \\ \boldsymbol{\xi}^- \\ \mu \end{pmatrix}, \\ \text{subject to} \quad & \begin{cases} \begin{pmatrix} \mathbf{K} & \text{–}\mathbf{K} & \text{–}\mathbf{I} & \mathbf{0} & \mathbf{1} \\ \text{–}\mathbf{K} & \mathbf{K} & \mathbf{0} & \text{–}\mathbf{I} & \text{–}\mathbf{1} \end{pmatrix} \begin{pmatrix} \boldsymbol{\alpha}^+ \\ \boldsymbol{\alpha}^- \\ \boldsymbol{\xi}^+ \\ \boldsymbol{\xi}^- \\ \mu \end{pmatrix} \leq \begin{pmatrix} \varepsilon + \mathbf{y} \\ \varepsilon - \mathbf{y} \end{pmatrix} \\ \boldsymbol{\alpha}^+, \boldsymbol{\alpha}^-, \boldsymbol{\xi}^+, \boldsymbol{\xi}^- \geq 0 \end{cases} \end{aligned} \tag{4.5}$$

where

$$\begin{aligned}
\mathbf{c} &= (\underbrace{1,...,1}_{2N},\underbrace{w,...,w}_{2N},0)^T \ , \\
\mathbf{y} &= (y_1,...,y_N)^T, \\
\boldsymbol{\alpha}^+ &= (\alpha_1^+,...,\alpha_N^+)^T, \\
\boldsymbol{\alpha}^- &= (\alpha_1^-,...,\alpha_N^-)^T, \\
\boldsymbol{\xi}^+ &= (\xi_1^+,...,\xi_N^+)^T, \\
\boldsymbol{\xi}^- &= (\xi_1^-,...,\xi_N^-)^T
\end{aligned} \tag{4.6}$$

and $\mathbf{I}$ is an $N \times N$ identity matrix. $\mathbf{K}$ is the kernel matrix with entries defined as $K_{ij} = \mathcal{K}(x_i, x_j)$,

$$\mathbf{K} = \begin{pmatrix} \mathcal{K}(x_1,x_1) & \mathcal{K}(x_1,x_2) & \cdots & \mathcal{K}(x_1,x_N) \\ \mathcal{K}(x_2,x_1) & \mathcal{K}(x_2,x_2) & \cdots & \mathcal{K}(x_2,x_N) \\ \vdots & \vdots & \ddots & \vdots \\ \mathcal{K}(x_N,x_1) & \mathcal{K}(x_N,x_2) & \cdots & \mathcal{K}(x_N,x_N) \end{pmatrix}. \tag{4.7}$$

The LP problem (4.5) is bounded and feasible by default and can always be solved using standard algorithms such as the simplex method or the interior point method [109].

An example of the IC curve obtained through LP-SVR is shown in Fig. 4.7. Note that the SVR algorithm gives a robust and smooth result even though a shorter range of data ($0.6Ah$-$0.85Ah$) is used. The algorithm performed well in terms of both model sparsity and data approximation.

For on-board implementation, there are factors associated with the charged capacity data q (such as the variation in data ranges, or estimation errors) could potentially affect the SVR model and the corresponding ICA results. The influence of those factors is investigated. First, the insensitivity of the SVR model to data range variations

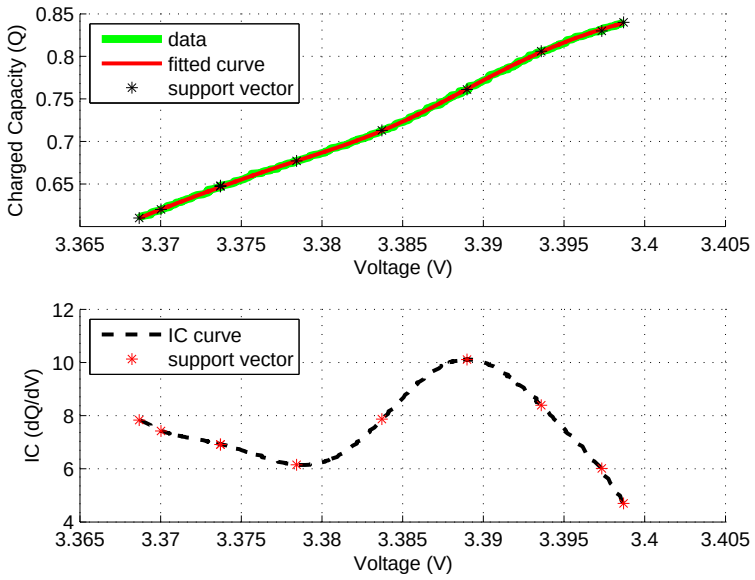

Figure 4.7: IC curve obtained by SVR.

is illustrated in Figs. 4.8 and 4.9, where the same results are obtained when a different data range is used (Fig. 4.8), and when only a sub-segment of data is used (Fig. 4.9). The IC peak values with respect to different data ranges are compared in Table 4.1. One can see that the maximum difference between the tabulated IC peak values is about 1%.

Table 4.1: Sensitivity of IC Peak Value to Different Data Range

$Q\ (Ah)$	0.55-0.90	0.55-0.93	0.55-0.95	0.35-0.85	0.45-0.85	0.60-0.85
IC Peak	10.17	10.18	10.18	10.05	10.17	10.14

The effects of estimation errors in q on the ICA results is also studied. Because of the data sampling scheme, the errors in q would only be reflected as a constant shift in the input data x. Assuming that $\mathbf{x}_{ref}$ is the set of accurate q and $\mathbf{x}_{err}$ is the set of q with a constant estimation error e (i.e., $\mathbf{x}_{err} = \mathbf{x}_{ref} + e$). With the use of the rbf

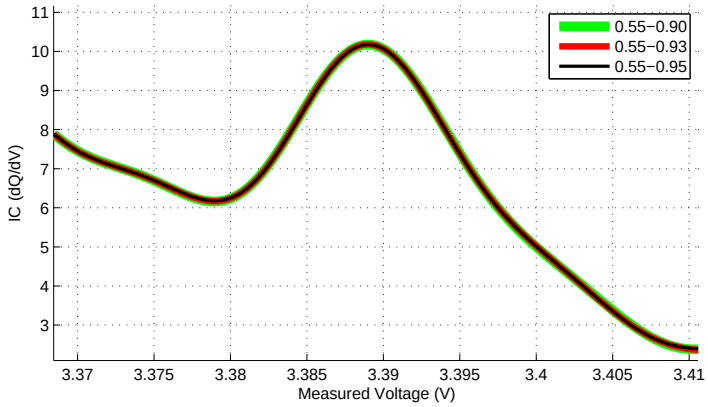

Figure 4.8: Sensitivity of SVR based IC curve to different range of Q.

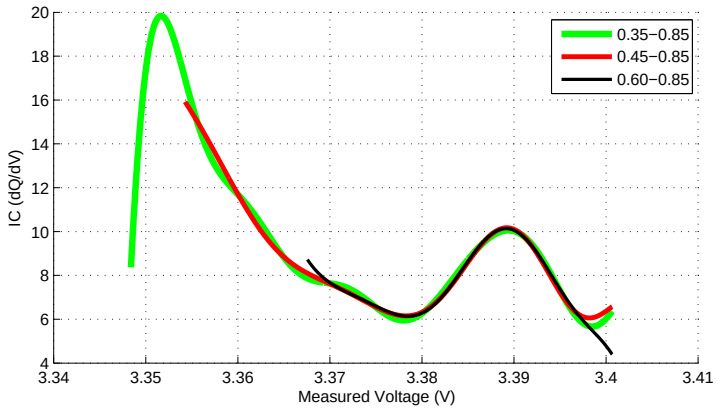

Figure 4.9: Sensitivity of SVR based IC curve to different data size.

kernel, the entries in the **K** matrix could be represented as,

$$\begin{aligned}\mathcal{K}(x_{err,i}, x_{err,j}) &= \exp(\frac{-\|x_{err,i} - x_{err,j}\|^2}{2\sigma^2}) \\ &= \exp(\frac{-\|(x_{ref,i} + e) - (x_{ref,j} + e)\|^2}{2\sigma^2}) \\ &= \exp(\frac{-\|x_{ref,i} - x_{ref,j} + e\|^2}{2\sigma^2}) \\ &= \mathcal{K}(x_{ref,i}, x_{ref,j})\end{aligned} \tag{4.8}$$

where the equality between $\mathcal{K}(x_{err,i}, x_{err,j})$ and $\mathcal{K}(x_{ref,i}, x_{ref,j})$ is referred as the translational invariant property. For any kernel functions that have the translational invariant properties, the **K** matrix would not be affected by a constant error in the

input $\mathbf{x}$. Therefore, in this particular problem, an estimation error in the data q would not change the final identification results or the ICA results.

There are also other environmental or operating factors including the temperature and charging current rate. Although those factors would not affect the application of the SVR method, they could change the ICA results due to their influence on the intercalation process. Consequently, it is preferred that the ICA-based SOH monitoring is performed under controlled temperature with a determined constant current rate.

4.2.3 Incremental Capacity Analysis Results Obtained by Support Vector Based Parameter Identification

Although the SVR method exhibits excellent capability of processing noisy data and performing accurate model regression, the algorithm involves a mathematical optimization process that depends on the entire data set and therefore requires non-trivial computational efforts to determine the parameters β_is. At the same time, for many applications such as an EV on-board battery management system, the on-line computational power is often limited. To improve the computational efficiency, and make it feasible for on-board implementation, we investigated the performance of the IC peak identification algorithm when the SVs are fixed from cycle to cycle (i.e., only apply LP-SVR to the initial data set to find SVs and favorable kernel functions, and then use the SVs and kernels as a parametric model for other aged battery data sets).

The LP-SVR problem in 4.5 is then reduced to an Support Vector Based Parameter Identification (SVPI) problem,

$$\begin{aligned} f(x_n) &= \sum_{i=1}^{N_{sv}} \beta_i k(sv_i, x_n) = \theta_{SV}^T \phi_{SV}, \\ \theta_{SV} &= [\beta_1, \beta_2, ..., \beta_{N_{sv}}]^T, \\ \phi_{SV} &= [k(sv_1, x_n), k(sv_2, x_n), ..., k(sv_{N_{sv}}, x_n)]^T \end{aligned} \tag{4.9}$$

where sv_i are the SVs identified previously by LP-SVR formulated in (4.5), N_{sv} is the total number of SVs, and the parameters β_is can be solved by parameter identification method such as least squares. Typically, $N_{sv} \ll N$. In this study, we have $N_{sv} = 9$ and $N = 200$.

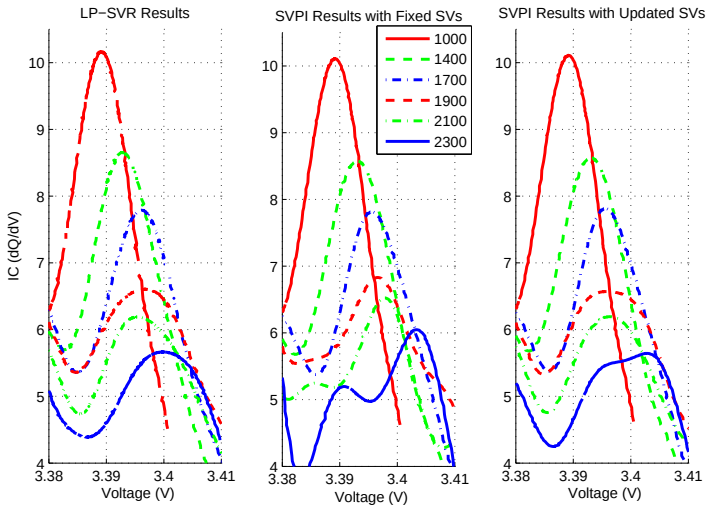

Figure 4.10: IC curves obtained by LP-SVR and SVPI.

Comparisons between the IC curves and corresponding peak values obtained by LP-SVR and by SVPI are displayed in Fig. 4.10. One can see that both methods give qualitatively the same results but the IC peak values from the two methods start to deviate from each other after 1900 cycles, which implies that the SVPI with a fixed set of SVs works well over a wide range of data and it is only necessary to update the SVs after a long period operation. Moreover, as plotted in Figs. 4.10 and 4.11, if the SVs are re-derived with the 1900 cycle data, we can obtain quantitatively the same results by both methods at all aging cycles.

We can establish a 2^{nd} order correlation between battery capacity and IC peak through the SVR results as well. The correlation curves identified by LP-SVR and SVPI are both plotted in Fig. 4.12. By updating the SVs at 1900 cycles, the two identified correlations are almost identical (the two curves overlap each other as shown in Fig. 4.12).

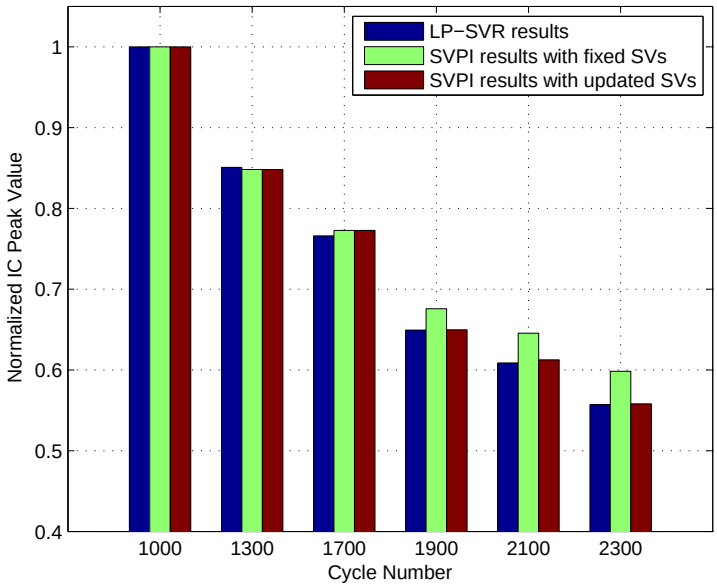

Figure 4.11: Normalized IC peak value obtained by LP-SVR and SVPI.

The correlation shown in Fig. 4.11, which is obtained for battery #7, will be used as the capacity fading prediction model. To validate the model, SVPI is also performed (with updated SVs) on the data sets of all other 7 battery cells at the chosen aging cycles. The signatures of decreasing IC peaks can be extracted clearly from all cells with partially charging data (about 60% to 85% SOC range). The normalized IC peaks and the capacities of all batteries are plotted in Fig. 4.13 with the correlation curve identified using data of battery #7. The maximum difference in the capacity is about 1% except the 5 outliers. Therefore, by normalizing both the capacities and IC peak values, the identified quantitative correlation can be used for effective on-board capacity estimation and SOH monitoring.

In terms of computational efficiency, because the major burden comes from the process of solving the LP problem, SVPI using least squares method for identification saves a significant amount of time compared to LP-SVR and is very promising for on-line applications. In the case of battery #7, the total processing times of LP-SVR

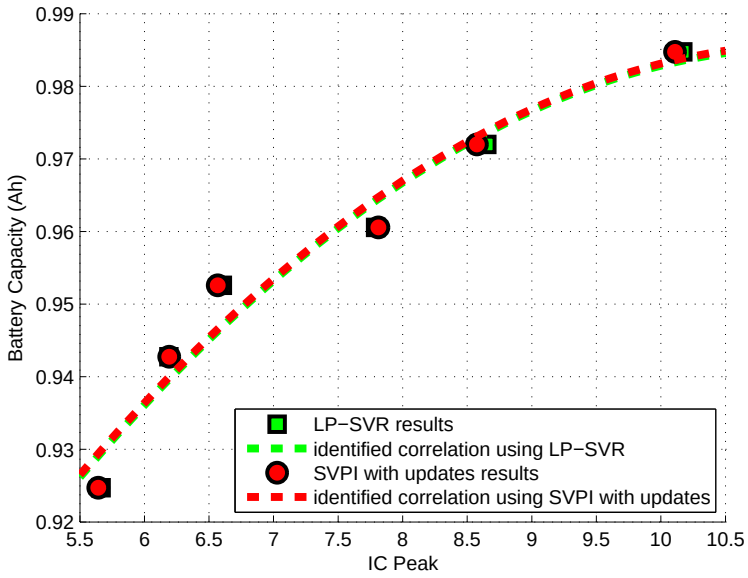

Figure 4.12: Correlation between faded capacity and IC peaks from SVR results.

and SVPI are 187 sec and 64 sec, respectively[1]. SVPI reduces 66% computational time compared to LP-SVR.

4.2.4 Development of State-of-Health Monitoring Framework Using Incremental Capacity Analysis Results

With the established quantitative correlation between the battery capacities and the IC peak values, an on-board SOH (mainly on battery capacity fading) monitoring framework is developed (Fig. 4.14). Different from conventional methods, our ICA based SOH monitoring framework uses partially charging data (about 60% to 85% SOC range), that are frequently available during real-life operations, to estimate the faded battery capacity on-board. Fully charging data is only needed for calibration after a long operation period. By using SVPI, the advantages of our framework in robustness and computational efficiency have both been demonstrated.

[1]Recorded on a computer with a 2.53GHz Intel Core 2 Duo CPU and 4.0 GB RAM.

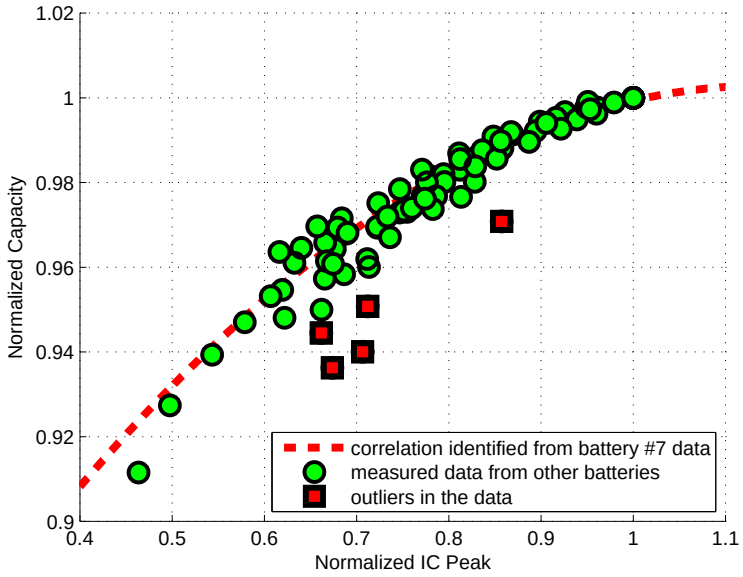

Figure 4.13: Normalized correlation between battery capacity and IC peak plotted with validation data.

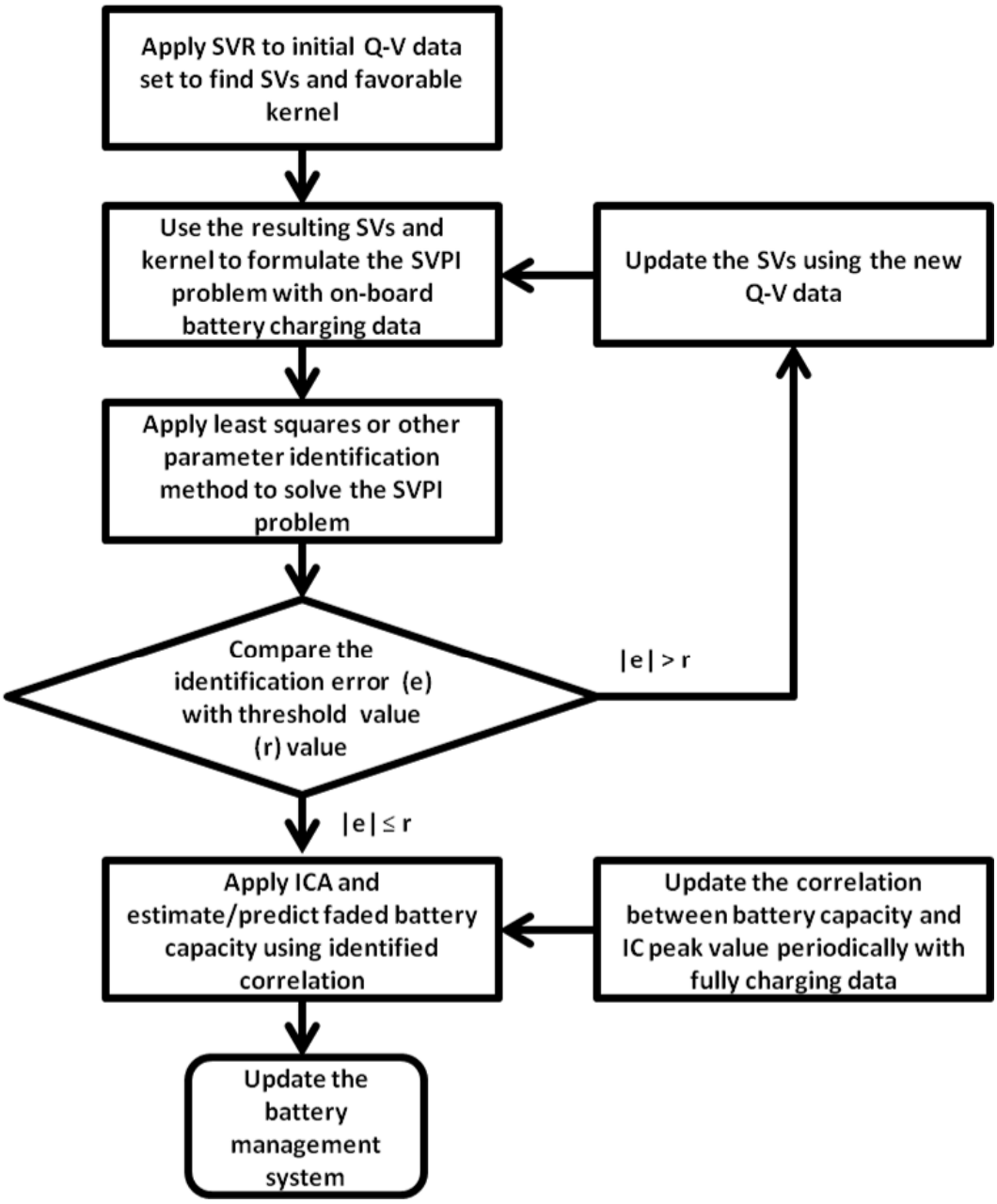

Figure 4.14: ICA based on-board SOH monitoring framework.

CHAPTER V

Model Parametrization and Adaptation Based on the Invariance of Support Vectors

To this end, both parametric and non-parametric approaches have been successfully developed and applied to monitor battery state-of-health (SOH) together with incremental capacity analysis (ICA) technique. The parametric model provides relevant physical insights and observable model structure but requires more efforts in development and parameter tuning. The support vector regression (SVR) algorithm involves an iterative optimization process, which is often computationally expensive and inefficient. For applications such as the battery SOH monitoring, where the identification algorithm needs to be applied repeatedly for multiple cells because of the variation in model dynamics (due to battery aging and cell-to-cell difference), the computational burden could pose difficulties for real-time or on-board implementation.

In this chapter, the battery V-Q curve identification problem for SOH monitoring is further studied so that the advantages of both parametric and non-parametric methods could be utilized. Based on experimental battery aging data, we establish a model parametrization and adaptation framework utilizing the simple structure of SVR representation with determined support vectors (SVs). The model parameters can then be estimated in real time. Under the formulation presented in Chapter IV,

the SVPI method requires an update for the SVs after the batteries are aged for a long period of time. The main reason why the invariance of SVs cannot be found is that the voltage data instead of the charged capacity date are used as input in the model. Since the voltage data do change over time, they might not have the invariant properties. On the other hand, because the voltage data are sampled within a determined range of charged capacity at fixed rate, using the charged capacity instead of the voltage data as the model inputs could help to establish the invariance of SVs. This different model formulation is then investigated in this chapter. Through mathematical analysis and simulations using mechanistic battery aging model, it is shown that, given a certain charged capacity (Q) range, the SVs of the battery models indeed stay invariant even when the batteries age or vary. The invariance of the SVs is verified using experimental aging data. Consequently, the resulting model for the battery V-Q curve can be directly incorporated in the battery management system and adapted on-line for SOH monitoring. Moreover, the general characteristics of the data that could maintain the SV invariance is identified. The proposed automated model parametrization process (via optimization algorithm) can be extended to nonlinear dynamic systems with the given properties.

5.1 Battery V-Q Curve and Support Vector Regression Model

5.1.1 Battery V-Q Curve Identification for Incremental Capacity Analysis

ICA has the advantage to detect a gradual change in cell behavior associated with its electrochemical properties during the aging process, with greater sensitivity than those based on conventional charge/discharge curves [12, 36]. As illustrated by Fig. 5.1, which shows the test data at different aging stage for a $LiFePO_4$ battery, the IC curve (Fig. 5.1(b)) has much identifiable aging signs than the V-Q curve (Fig. 5.1(a)). It is useful particularly for battery SOH monitoring as the extracted peak

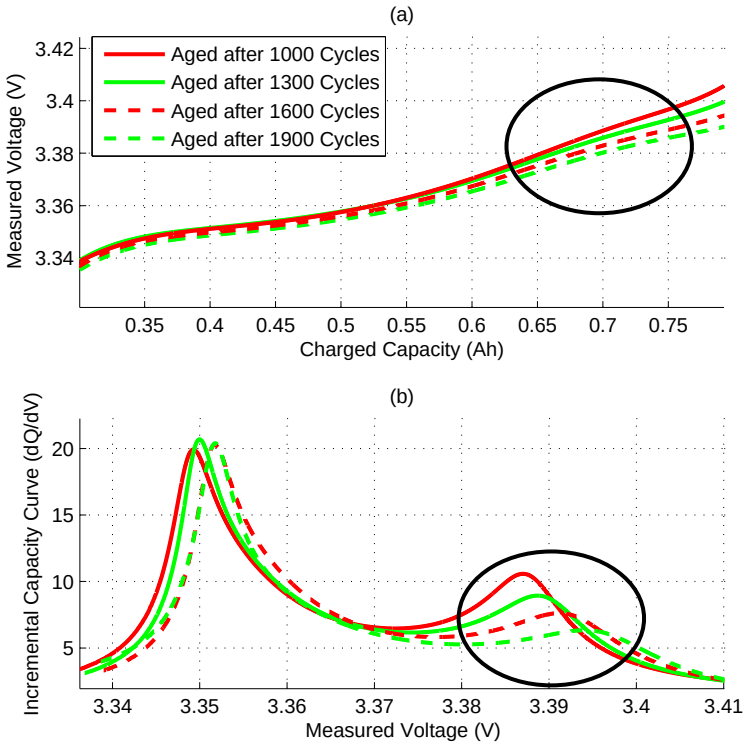

Figure 5.1: Aging signature extracted using ICA.

values and their change pattern on the IC curves are closely related to the battery capacity fading, and can be used for characterizing the aging mechanism.

In previous chapters, several numerical procedures are developed and evaluated for extracting the IC curves from battery V-Q data. While the ICA results are sensitive to the selection of curve fitting method, the support vector regression (SVR) approach with the Gaussian radial basis function (rbf) kernel is shown to be the most robust and effective method. The use of SVR to represent the V-Q relation and then using analytic derivative to obtain the IC curve provides the most consistent identification results with moderate computational load [16].

5.1.2 Support Vector Regression Model

As discussed above, the SVR was chosen for the battery V-Q curve identification because of its demonstrated potential in the realm of nonlinear system identification

[105, 106, 108]. Let $x = q$, $y = v$ be the input and output of the SVR model, where q represents the battery charged capacity, v is the measured voltage. The SVR model for the V-Q curve can thereby be represented as,

$$y = \sum_{i=1}^{N} \beta_i \mathcal{K}(x_i, x) + \mu, \tag{5.1}$$

where N is the number of data points in the data set, β_is and μ are the model parameters, whose values are determined based on the data set, and $\mathcal{K}(\cdot, \cdot)$ is the selected kernel. Again, the rbf kernel is used and is expressed as

$$\mathcal{K}(x, x') = \exp(\frac{-\|x - x'\|^2}{2\sigma^2}) \tag{5.2}$$

where σ is the adjustable parameter for the kernel function.

The parameters used in model (5.1) are identified by solving a convex quadratic programming (QP) problem. Through the QP-SVR and appropriate selected kernel, the flatness property is enforced in both the feature space and input space [83, 105]. Conventional QP-SVR has been successfully applied in identifying nonlinear dynamic systems[105, 108, 110]. However, the implementation of QP-SVR may not guarantee sufficient model sparsity. LP-SVR that employs ℓ_1 norm as regularizer was then proposed to improve the model sparsity and computational efficiency [106, 107, 111, 112]. As shown in previous chapters (Eqn. (4.5)), LP was used as the optimization engine to derive the SVR model [16].

Figure 5.2 shows how the LP-SVR algorithm is implemented for the identification of the battery V-Q curve. First the parameters in model (5.1) are determined, and the SVR model of the V-Q curve

$$f(x_n) = \sum_{i=1}^{N_{sv}} \beta_i \mathcal{K}(sv_i, x_n) + \mu \tag{5.3}$$

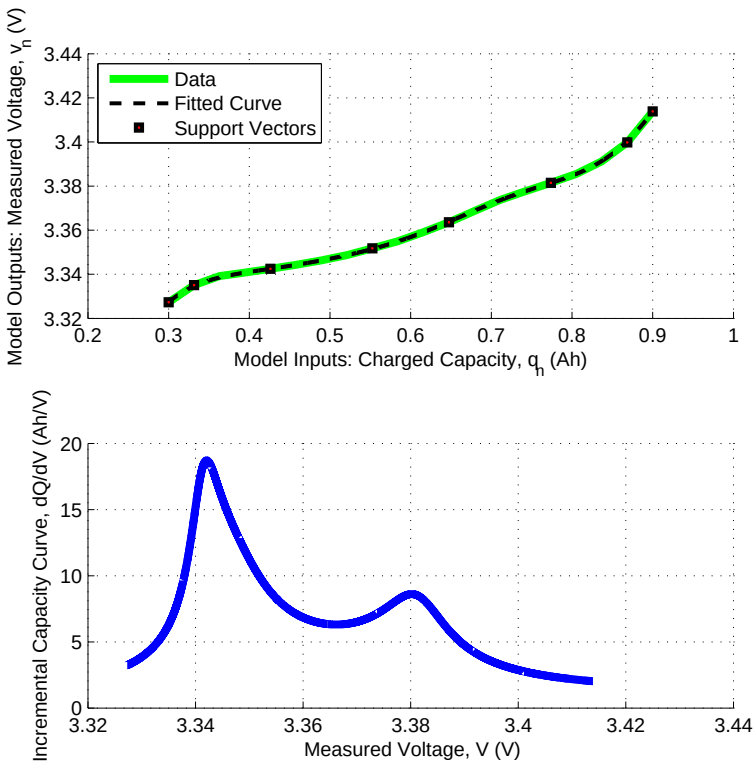

Figure 5.2: Implementation of LP-SVR for battery V-Q and IC curve identification.

is obtained, where sv_i $(i = 1, \cdots, N_{sv})$ are the SVs identified by the LP-SVR algorithm and N_{sv} is the total number of SVs ($N_{sv} \ll N$).

Then the IC curve can be computed from the fitted V-Q curve as follows,

$$\frac{dQ}{dV} = \frac{1}{f'(x_n)} = \frac{1}{\sum_{i=1}^{N_{sv}} \beta_i \mathcal{K}'(sv_i, x_n)} \tag{5.4}$$

Using the ICA technique, we can then extract battery aging information through the changes observed from the IC peaks. Please note that the correlation between battery capacity and IC peaks could be influenced by environmental temperature. Therefore, our SOH monitoring framework is designed based on battery charging data collected under constant temperature. We think it is a valid assumption since active thermal management systems are implemented on most commercial electric vehicles.

On the other hand, since the ICA is mainly based on the lithium intercalation process, it might not be directly applicable to battery chemistries such as Pb-Acid and Ni-MH. Nonetheless, because voltage data of any battery cells are associated with their fading and degradation, it is possible that one could extract aging signature (perhaps different from lithium ion batteries) using the $\mathrm{d}Q/\mathrm{d}V$ analysis from those chemistries as well.

Even though LP-SVR works well for retrieving the IC curve from battery voltage measurement, it has to be applied repeatedly to different cells at different ages. For applications such as electric vehicles, which usually contain hundreds or thousands of battery cells, the extensive computational effort required for solving the LP problems could not be satisfied on-board or in real-time.

If the simple structure produced by the LP-SVR, Eqn. (5.3), can be generalized as a parametric model with kernel functions as the basis and the SVs invariant, for all cells under all conditions, conventional parameter estimation methods such as the least squares can be directly used and the computational efficiency would be greatly improved. In this case, the LP-SVR algorithm is only used for the initial model identification and parametrization, while the parameter adaptation to fit individual cell data and aging status could be achieved through linear parameter identification that does not require iterative optimization.

5.2 Conditions for Support Vectors Invariance and Parametric Linear Programming

In order to investigate the possibility of using the SVR model as a parametric model with invariant support vectors, an LP sensitivity study is performed to understand the variations of the SVs with respect to the data variation. For the convenience of performing LP sensitivity study, we can transform problem (4.5) into a standard

LP formulation,

$$\begin{aligned} &\min_{\boldsymbol{\chi}} \quad \mathbf{c}^T\boldsymbol{\chi}, \\ &\text{subject to} \begin{cases} \mathbf{A}\boldsymbol{\chi} = \mathbf{b}, \\ \boldsymbol{\chi} \geq 0 \end{cases} \end{aligned} \tag{5.5}$$

where

$$\begin{aligned} \mathbf{c} = &\ (\underbrace{1,...,1}_{2N}, \underbrace{w,...,w}_{2N}, \underbrace{0,...,0}_{2N+2})^T \ , \\ \boldsymbol{\chi} = &\ (\boldsymbol{\alpha}^+; \boldsymbol{\alpha}^-; \boldsymbol{\xi}^+; \boldsymbol{\xi}^-; \mu^+; \mu^-; \mathbf{s}^+; \mathbf{s}^-), \\ \mathbf{A} = &\ \begin{pmatrix} \mathbf{K} & -\mathbf{K} & -\mathbf{I} & \mathbf{0} & \mathbf{1} & -\mathbf{1} & \mathbf{I} & \mathbf{0} \\ -\mathbf{K} & \mathbf{K} & \mathbf{0} & -\mathbf{I} & -\mathbf{1} & \mathbf{1} & \mathbf{0} & \mathbf{I} \end{pmatrix}, \\ \mathbf{b} = &\ \begin{pmatrix} \varepsilon + \mathbf{y} \\ \varepsilon - \mathbf{y} \end{pmatrix}, \\ \mu = &\ \mu^+ + \mu^-, \end{aligned} \tag{5.6}$$

μ^+ and μ^- are added to ensure nonnegativity on the decision variable, $\mathbf{s}^+$ and $\mathbf{s}^-$ are added to convert the inequality constraints into equality. This new formulation is equivalent to the original problem (4.5) [109].

5.2.1 Formulation of Parametric Linear Programming

Let us assume that we have found an optimal basis matrix $\mathbf{B}$ for the standard LP problem, where

$$\mathbf{B} = \begin{pmatrix} \mathbf{A}_{\Omega(1)} & \mathbf{A}_{\Omega(2)} & ... & \mathbf{A}_{\Omega(m)} \end{pmatrix} \tag{5.7}$$

and $\mathbf{A}_{\Omega(1)}$, ..., $\mathbf{A}_{\Omega(m)}$ are linear independent columns chosen as the optimal basis from the constraint matrix $\mathbf{A}$. Then $\mathbf{B}$ must satisfy the following conditions [109],

$$\begin{aligned} \mathbf{B}^{-1}\mathbf{b} &\geq 0 \\ \mathbf{c} - \mathbf{c_B}\mathbf{B}^{-1}\mathbf{A} &\geq 0 \end{aligned} \tag{5.8}$$

where $\mathbf{c_B}$ consists of the entries in the objective vector $\mathbf{c}$ corresponding to the optimal basis matrix $\mathbf{B}$,

$$\mathbf{c_B} = \begin{pmatrix} \mathbf{c}_{\Omega(1)} & \mathbf{c}_{\Omega(2)} & ... & \mathbf{c}_{\Omega(m)} \end{pmatrix}^T. \tag{5.9}$$

Now consider the different LP problem (5.5) for a different data set that is obtained either for a different cell or for the same cell at a different aging stage. In our study, the battery charging data are always sampled between the same range of charged capacity at the same sampling rate (that is, the variable $\mathbf{x}$ in problem (4.3) does not change from cell to cell and at different aging stage). Although this sampling scheme might appear to be a limitation of the technique for on-board implementation, those data samples should be available during normal operations, as the range of the charged capacity data we are using is within the typical operating range of electric vehicles. Because of the sampling scheme, the matrix $\mathbf{K}$ and the constraint matrix $\mathbf{A}$ in (5.5) do not vary as the data set changes. In addition, the objective vector $\mathbf{c}$ is always kept constant. The only term that is changed in the LP problem definition is $\mathbf{b}$ in the constraint. Therefore, the condition, $\mathbf{c} - \mathbf{c_B}\mathbf{B}^{-1}\mathbf{A} \geq 0$, is always satisfied even when data variation occurs. The optimal condition for the original optimal basis matrix $\mathbf{B}$ to be satisfied by the new data set can then be reduced to,

$$\mathbf{B}^{-1}\mathbf{b} \geq 0 \tag{5.10}$$

Since the optimal basis matrix $\mathbf{B}$ decides the values of the SVs, it can be concluded that the SVs for the battery V-Q model would not change if, given $\mathbf{B}$, the condition (5.10) is satisfied for the new data set. If (5.10) is satisfied for all data sets collected for different cells and at different aging stages, we call the SVs invariant, and the same SVs and basis functions can be used to represent different V-Q characteristics for different cells and at different aging stage.

Moreover, $\mathbf{b}$ only depends on the variable $\mathbf{y}$, which is the voltage measurement from the battery charging data. Hence the sensitivity analysis only needs be performed with respect to $\mathbf{y}$ in our work, and problem (5.5) can be rewritten as,

$$\begin{aligned} &\min \quad \mathbf{c}^T \boldsymbol{\chi}, \\ &\text{subject to} \begin{cases} \mathbf{A}\boldsymbol{\chi} = \mathbf{b}(\mathbf{y}), \\ \boldsymbol{\chi} \geq 0 \end{cases} . \end{aligned} \tag{5.11}$$

The formulation shown in problem (5.11) is typically referred as parametric linear programming [113]. In conventional parametric LP problems, the dependence of $\mathbf{b}$ on the varying parameters is usually linear. One can find the correspondence between all the optimal basis and the varying parameters by solving systems of linear equalities. However, in our battery V-Q identification problem, the data variation is nonlinear and a proper parametrization needs to be found for characterizing the variation.

5.2.2 Special Scenario: Constant Shift in the Battery Data

Before proceeding to more complex cases, let us first consider the special scenario: constant shift in the battery data. Let $\mathbf{y}_1$ be the reference data set, and $\mathbf{y}_2$ be the data set with a constant shift (i.e. $\mathbf{y}_2 = \mathbf{y}_1 + \rho$). We have the following proposition.

Proposition V.1. *A constant shift in the data does not change the SVs.*

Proof. Assume that the optimal solution of (5.11) corresponding to the data $\mathbf{y}_1$ is $\boldsymbol{\chi}_*$,

where

$$\boldsymbol{\chi}_* = (\boldsymbol{\alpha}_*^+; \boldsymbol{\alpha}_*^-; \boldsymbol{\xi}_*^+; \boldsymbol{\xi}_*^-; \mu_*^+; \mu_*^-; \mathbf{s}_*^+; \mathbf{s}_*^-). \tag{5.12}$$

Please note that the column vectors in $\mathbf{B}$ that correspond to μ^+ or μ^- are not related to the invariance of SVs, they can be treated independently from the rest of the basis vectors. For that reason, let $\hat{\boldsymbol{\chi}}_*$ and $\hat{\mathbf{A}}$ be the submatrices of $\boldsymbol{\chi}_*$ and $\mathbf{A}$ excluding the columns associated with μ^+ or μ^-, respectively. That is,

$$\begin{aligned} \hat{\mathbf{A}} &= \begin{pmatrix} \mathbf{K} & -\mathbf{K} & -\mathbf{I} & \mathbf{0} & \mathbf{I} & \mathbf{0} \\ -\mathbf{K} & \mathbf{K} & \mathbf{0} & -\mathbf{I} & \mathbf{0} & \mathbf{I} \end{pmatrix}, \\ \hat{\boldsymbol{\chi}}_* &= (\boldsymbol{\alpha}_*^+; \boldsymbol{\alpha}_*^-; \boldsymbol{\xi}_*^+; \boldsymbol{\xi}_*^-; \mathbf{s}_*^+; \mathbf{s}_*^-). \end{aligned} \tag{5.13}$$

We then have

$$\hat{\mathbf{A}}\hat{\boldsymbol{\chi}}_* + \begin{pmatrix} \mathbf{1} & -\mathbf{1} \\ -\mathbf{1} & \mathbf{1} \end{pmatrix} \begin{pmatrix} \mu_*^+ \\ \mu_*^- \end{pmatrix} = \mathbf{A}\boldsymbol{\chi}_* = \mathbf{b}(\mathbf{y_1}) = \begin{pmatrix} \varepsilon + \mathbf{y}_1 \\ \varepsilon - \mathbf{y}_1 \end{pmatrix}. \tag{5.14}$$

On the other hand, let

$$\begin{pmatrix} \mathbf{1} & -\mathbf{1} \\ -\mathbf{1} & \mathbf{1} \end{pmatrix} \begin{pmatrix} \mu^+ \\ \mu^- \end{pmatrix} = \begin{pmatrix} \mathbf{1} & -\mathbf{1} \\ -\mathbf{1} & \mathbf{1} \end{pmatrix} \begin{pmatrix} \mu_*^+ \\ \mu_*^- \end{pmatrix} + \begin{pmatrix} \mathbf{1} \\ -\mathbf{1} \end{pmatrix} \rho. \tag{5.15}$$

By substituting (5.15) into (5.14), the following equation is obtained,

$$\begin{aligned}
&\hat{\mathbf{A}}\hat{\boldsymbol{\chi}}_* + \begin{pmatrix} \mathbf{1} & -\mathbf{1} \\ -\mathbf{1} & \mathbf{1} \end{pmatrix} \begin{pmatrix} \mu^+ \\ \mu^- \end{pmatrix} \\
=&\hat{\mathbf{A}}\hat{\boldsymbol{\chi}}_* + \begin{pmatrix} \mathbf{1} & -\mathbf{1} \\ -\mathbf{1} & \mathbf{1} \end{pmatrix} \begin{pmatrix} \mu_*^+ \\ \mu_*^- \end{pmatrix} + \begin{pmatrix} \mathbf{1} \\ -\mathbf{1} \end{pmatrix} \rho \\
=& \begin{pmatrix} \varepsilon + \mathbf{y}_1 \\ \varepsilon - \mathbf{y}_1 \end{pmatrix} + \begin{pmatrix} \mathbf{1} \\ -\mathbf{1} \end{pmatrix} \rho = \begin{pmatrix} \varepsilon + \mathbf{y}_1 + \boldsymbol{\rho} \\ \varepsilon - \mathbf{y}_1 - \boldsymbol{\rho} \end{pmatrix} \\
=& \begin{pmatrix} \varepsilon + \mathbf{y}_2 \\ \varepsilon - \mathbf{y}_2 \end{pmatrix} = \mathbf{b}(\mathbf{y}_2)
\end{aligned} \tag{5.16}$$

where one should see that the change in ρ would be compensated by adjusting either μ^+ or μ^-, without affecting the value of $\hat{\boldsymbol{\chi}}_*$. The LP problems with $\mathbf{y}_1$ and that with $\mathbf{y}_2$ share the same $\hat{\boldsymbol{\chi}}_*$ as part of their optimal solutions. Therefore the variation in the constant term ρ does not change the SVs. □

5.3 Voltage Data Variation

As shown in (5.11), the variation of the constraints is determined by variation of battery voltage data collected during the charging process. The variation could be caused by several different mechanisms including loss of cyclable lithium, loss of active material and increase of internal resistance. Those performance degradations could be reflected as different changing patterns in the charging voltage data. In general, the voltage data tend to increase at a given charged capacity as the battery ages. The detailed variation characteristics is investigated in this section and the relationship between reference data and aged data,

$$V_{\text{aged}} = g(V_{\text{ref}}) \tag{5.17}$$

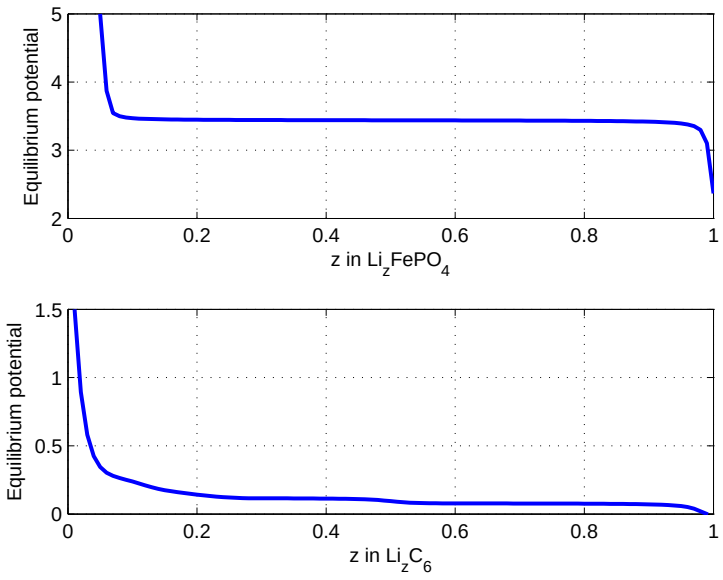

Figure 5.3: The equilibrium potentials of $LiFePO_4$ batteries.

is explored.

5.3.1 Characterization of Battery Data Variation Using Mechanistic Battery Aging Model Simulation

The variation in battery voltage measurement during aging are simulated using the mechanistic battery aging model developed in Ref. [114]. The battery model considers the aging mechanism of both the positive and negative electrodes, and could reflect the qualitative relationship between the equilibrium potentials and battery aging status. Figure 5.3 shows the equilibrium potentials of $LiFePO_4$ batteries. The analytic models for the equilibrium potentials can be found in literature [115, 116]. The overall equilibrium potential of the battery cell is the difference between the positive electrode and the negative electrode, $V_{\text{total}} = V_{\text{PE}} - V_{\text{NE}}$ (see Fig. 5.4).

As discussed in Ref. [76], the capacity fading in $LiFePO_4$ cells is mainly caused by the loss of cycable lithium at the early stages of aging. The loss of cycable lithium could be simulated by shifting the relative location of the two potential curves [114].

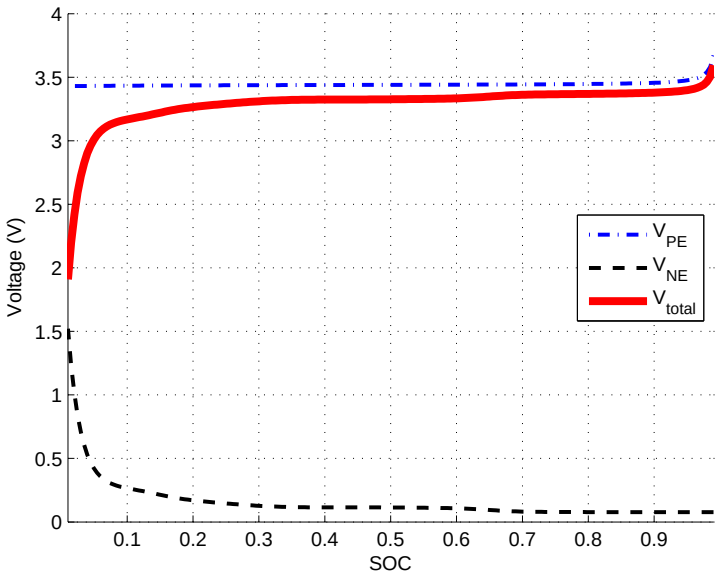

Figure 5.4: Open-circuit-voltage of $LiFePO_4$ batteries simulated using the mechanistic battery aging model.

The simulation results are shown in Fig. 5.5, where the voltage output of the model of the aged cells, V_{aged}, is plotted versus the output of the reference cell, V_{ref}, which represents a new battery.

It is observed that the relation between V_{aged} and V_{ref} could be approximated by a quadratic function,

$$\begin{aligned} \mathbf{y}(q) &= p_2 \mathbf{y}_*(q)^2 + p_1 \mathbf{y}_*(q) + p_0 \\ y &= V_{\text{aged}} \\ y_* &= V_{\text{ref}} \end{aligned} \tag{5.18}$$

where p_0, p_1 and p_2 are the parameters of the quadratic function and they vary as a function of aging status. y_* is the voltage of the fresh battery at a given charge capacity q.

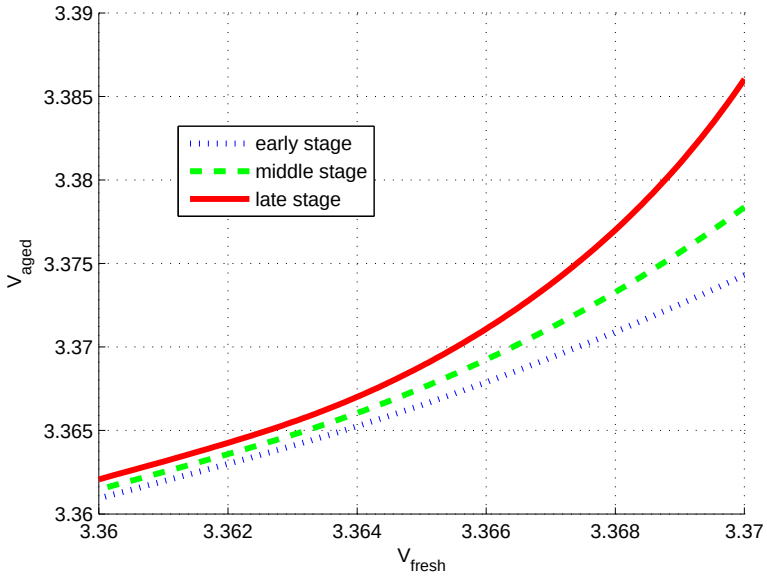

Figure 5.5: Simulated voltage variations of $LiFePO_4$ batteries at different aging stages.

5.3.2 Data Verification

The quadratic approximation (Eqn. (5.18)) found using the mechanistic battery aging model that relates the voltage response of the aged cell to that of a fresh new cell can be verified with the actual test data. As mentioned above, the data used in this study are collected from eight A123 APR18650 cells over a period of 18 months. Figure 5.6 shows two sets of data variation at different aging stages. The curves can be fitted with quadratic functions with good accuracy.

Hence, the quadratic function is indeed a good approximation and can be used for characterizing the voltage variation.

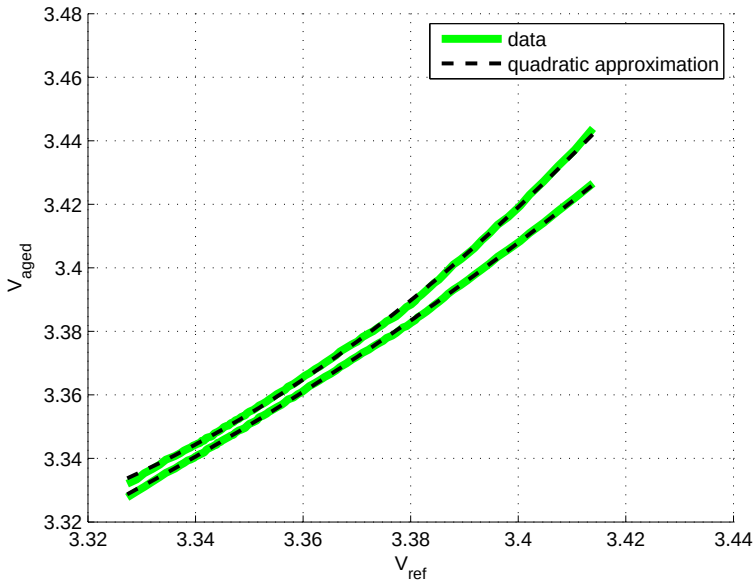

Figure 5.6: Voltage variation of $LiFePO_4$ batteries observed in the test data at $T = 35^oC$.

5.4 Invariance of the Support Vectors and Linear Parametric Model

5.4.1 Results from Monte Carlo Simulations

Since the characteristics of voltage variation are identified, we can then investigate under what conditions the optimal basis computed from the reference data stays invariant when the parameters of the quadratic function vary as the cell ages. In particular, we are interested in finding the following feasible region for SV invariance. Assuming that the following problem,

$$\begin{aligned} &\min \quad \mathbf{c}^T \boldsymbol{\chi}, \\ &\text{subject to} \begin{cases} \mathbf{A}\boldsymbol{\chi} = \mathbf{b}(\mathbf{y}_*), \\ \boldsymbol{\chi} \geq 0. \end{cases} \end{aligned} \tag{5.19}$$

has the optimal basis $\mathbf{B}$, then for any pair of p_1 and p_2, if the corresponding $\mathbf{b}(\mathbf{y})$ satisfies $\mathbf{B}^{-1}\mathbf{b}(\mathbf{y}) \geq 0$, the pair (p_1, p_2) is considered feasible. Otherwise the pair is infeasible.

As discussed above (see Prop. V.1), the variation in the constant term p_0 does not affect the invariance of the SVs, and it can be ignored in solving the parametric LP problems.

Different from the general approaches for solving the conventional parametric LP problems, the dependence of $\mathbf{b}$ on the varying parameters, p_1 and p_2, is nonlinear. Instead of solving systems of linear equalities, the determination of feasibility for each parameter pair (p_1, p_2) is done through Monte Carlo simulations. The results are shown in Fig. 5.7, where the green region highlights the feasible region.

On the other hand, we can find the region, where $\mathbf{y}$ and $\mathbf{y}_*$ have a monotonic increasing relation, by computing

$$\frac{\partial \mathbf{y}}{\partial \mathbf{y}_*} = 2p_2\mathbf{y}_* + p_1 \geq 0 \tag{5.20}$$

and therefore the region (marker by blue dashed lines in Fig. 5.7) is defined by the following two boundary functions,

$$\begin{aligned} p_1 &\geq -(2y_{*,\min})p_2, \\ p_1 &\geq -(2y_{*,\max})p_2. \end{aligned} \tag{5.21}$$

where $y_{*,\min}$ and $y_{*,\max}$ are the minimum and maximum values of V_{ref}, which is measured when the battery is fresh.

From the simulation results shown in Fig. 5.7, one can see that the feasible region computed by the Monte Carlo simulations coincides with the region where $\mathbf{y}$ is monotonically increasing. The results imply that the SVs for the battery V-Q curve model would stay invariant as long as the variation in the voltage data satisfies

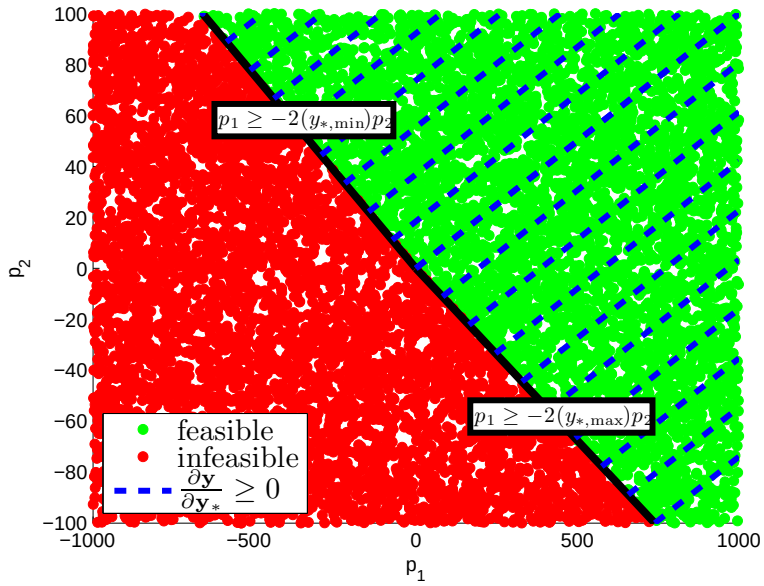

Figure 5.7: Monte Carlo simulations for determining feasible region of (p_1, p_2) corresponding to the optimal basis $\mathbf{B}$.

a quadratic and monotonic increasing relationship. As shown in Figs. 5.4 and 5.5, the monotonic quadratic relationship is consistent with our simulation results and observations from the battery data.

5.4.2 Model Parametrization

According to the analysis performed above, the SVs should not change even when battery ages or varies for our applications. Figure 5.8 show the LP-SVR results for the data of one cell at different ages. The invariance of the SVs can be clearly observed from the plot. Therefore, the structure obtained by the initial LP-SVR results can be used as a parametric model for the identification of battery V-Q curves. The model is parametrized as follows,

$$v = \sum_{i=1}^{N_{sv}} \beta_i \mathcal{K}(sv_i, q) + \mu \tag{5.22}$$

The main difference between the model (5.22) and the formulation in (4.1) and

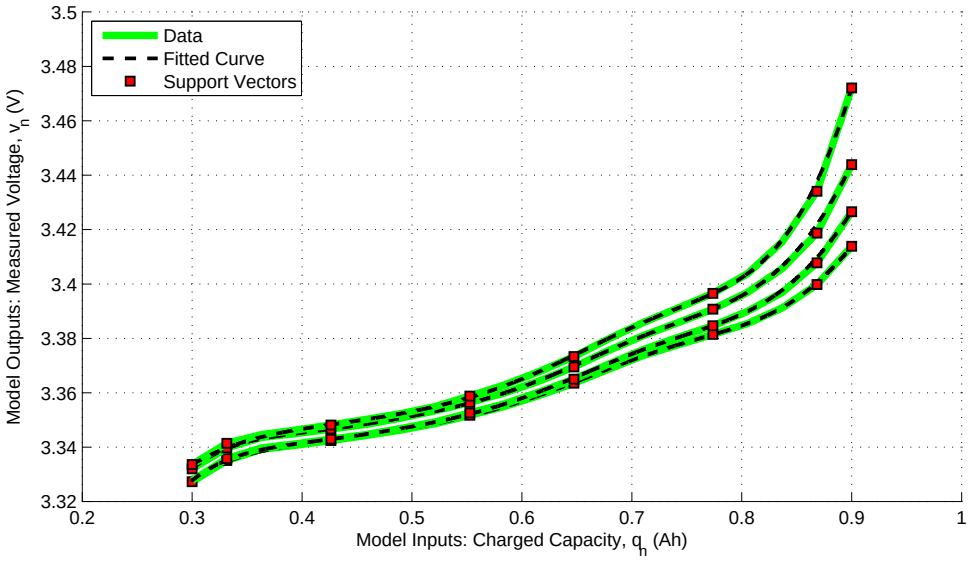

Figure 5.8: Invariance of SVs from LP-SVR results.

(4.9), the parametric model now has q as input and v as output, as well as a drift term μ. Those changes have helped to establish the invariant properties of the SVs.

For on-board implementation, the estimation problem of the model parameters $\boldsymbol{\beta}$ and μ can be formulated as the following,

$$v_j = \boldsymbol{\theta}^T \boldsymbol{\phi}_j \tag{5.23}$$

where

$$\begin{aligned} \boldsymbol{\theta} &= [\boldsymbol{\beta}^T, \mu]^T, \\ \boldsymbol{\phi}_j &= [\mathcal{K}(sv_1, q_j), ..., \mathcal{K}(sv_{N_{sv}}, q_j), 1]^T, \\ \boldsymbol{\beta} &= [\beta_1, ..., \beta_{N_{sv}}]^T \end{aligned} \tag{5.24}$$

and the parameters could be solved by the standard least squares method (LSM),

$$\boldsymbol{\theta} = (\boldsymbol{\Phi}^T \boldsymbol{\Phi})^{-1} \boldsymbol{\Phi}^T \mathbf{V}, \tag{5.25}$$

where

$$\begin{aligned} \mathbf{V} &= [v_1, ..., v_N]^T, \\ \mathbf{\Phi} &= [\boldsymbol{\phi}_1, ..., \boldsymbol{\phi}_N]^T. \end{aligned} \tag{5.26}$$

Given that the battery (V, Q) data are collected at fixed sample of Q points, $\mathbf{\Phi}$ in (5.25) is a constant matrix for all time. Therefore, the parameter $\boldsymbol{\theta}$ can be simply calculated as,

$$\boldsymbol{\theta} = \mathbf{h}^T \mathbf{V}, \tag{5.27}$$

where

$$\mathbf{h} = \mathbf{\Phi}(\mathbf{\Phi}^T \mathbf{\Phi})^{-1} \tag{5.28}$$

is a constant matrix and can be computed offline.

Table 5.1: Computational Time and Estimation Error Comparison

Data Points	LP-SVR		LSM	
	Time (sec.)	RMS (V)	Time (sec.)	RMS (V)
20	0.4733	7.64×10^{-4}	1.1×10^{-5}	2.57×10^{-4}
50	4.201	4.18×10^{-4}	1.1×10^{-5}	2.53×10^{-4}
100	30.01	3.83×10^{-4}	1.1×10^{-5}	2.42×10^{-4}
200	211.5	3.40×10^{-4}	1.6×10^{-5}	2.54×10^{-4}

†The assessment summarized in Table 5.1 was performed on a laptop computer with a 32-bit Intel Core2 Duo CPU @ 2.53GHz and 4.0 GB RAM

The computational time of using the LP-SVR and the LSM for the V-Q curve identification are compared in Table 5.1. The four groups of data are sampled within the same range of charged capacity but with different sampling rate, so the results of different sizes of data could also be compared. One can see that the computational time of the LSM is several order of magnitude less than that of the LP-SVR, and

insensitive to the dimension of sampled data. The parametric battery V-Q curve model provides a more robust and computationally efficient way to obtain the IC curves from raw data measurement, without sacrificing any estimation accuracy.

5.4.3 Model Sensitivity with Respect to Estimation Error in Charged Capacity

The data sampling scheme proposed in this study is subject to the error in the estimation of charged capacity data q. Therefore the model robustness with respect to the estimation error in q needs to be verified. In this case, a similar parametric linear programming problem could be be considered since $\mathbf{b}$ in (5.5) is again the only varying component. Fig. 5.9 shows that when 0.05 Ah error (about 5% in SOC) in the data q would only lead to a difference of 0.5 in the IC peak value (equivalent to less than 1% in capacity estimation). Therefore it could be concluded that the proposed model is insensitive to the estimation error in charged capacity.

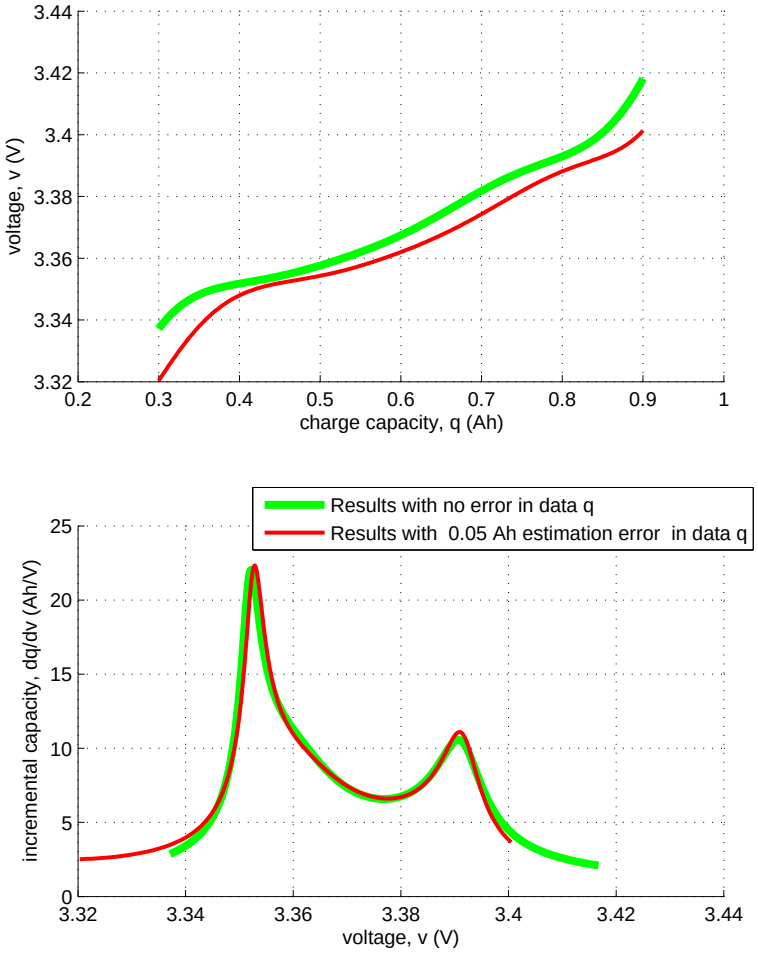

Figure 5.9: ICA results comparison with estimation error in charged capacity data q.

CHAPTER VI

State-of-Health Monitoring Applied to Multi-cell Battery Modules

The effectiveness and robustness of incremental capacity analysis (ICA) for single cell diagnostics have been demonstrated in previous chapters. In this chapter, we extend the ICA based battery state-of-health (SOH) monitoring framework from single cells to multi-cell battery modules, which consist of battery cells with various aging conditions. Results show that the framework developed for single cell capacity estimation can also be used for battery packs. Analysis through both simulations and experimental results are presented.

The main difference between single cell and parallel-connected battery pack, when applying the ICA, is the uneven current distribution due to the cell non-uniformity. Consequently, the current going through each cell in the pack could be time varying even when the pack is charged at a constant current. Since ICA typically requires constant charging/discharging data, the uneven distribution could affect the applicability of ICA to a battery pack. Therefore the SOH monitoring for batteries in a pack is even more challenging than the monitoring of single cells. The study reported in this chapter aims to extend the ICA based battery SOH monitoring framework developed for single cells to battery packs. The applicability of the framework is investigated using both simulations and experimental results.

6.1 Multi-Cell SOH Monitoring and Cell Non-Uniformity

For single battery cells, the effectiveness of ICA based SOH monitoring is built on the fact that the IC peaks are quantitatively correlated to cell capacity and therefore could be used to identify capacity degradation [16]. For cells connected If the correlation between capacity and IC peak value still holds for a pack, the ICA based capacity estimation approach could be extended from cells to packs. Most popular battery pack configurations connect cells in parallel first to form small modules, and then connect the modules in series to form the pack. For instance, the Chevrolet Volt's pack divided its 288 cells into 96 modules with 3 cells connected in parallel, and Nissan Leaf has battery modules, each contains two 2-cell strings that are connected in parallel. The parallel connected cells can self-balance their SOC throughout the operations. The configuration also improves the overall robustness of the battery pack in case of cell failure. However, in such design, the currents going through individual cells are usually not monitored [117]. As the individual cell measurements are no longer available, the ICA based battery capacity estimation framework has to be performed using the data measured at model terminal. Moreover, cell-to-cell variation is inevitable in battery productions [118]. During operations, the variation might grow larger, as the aging rate of each cell could be different. The existence of cell non-uniformity could lead to uneven current distribution among the parallel-connected cells, thereby making SOH monitoring more challenging compared to the single cell case. In this chapter, battery module refers to several parallel-connected cells and we focus our investigation on the applicability of ICA to the module with terminal measurements, and how cell non-uniformity in the module could affect the application.

Toward this end, an inventory of 30 test cells at different aging stage is established. The batteries available for this study are $LiFePO_4$ cells from A123 with the specifications listed in Table 2.1. The battery cells have different degrees of degradation after

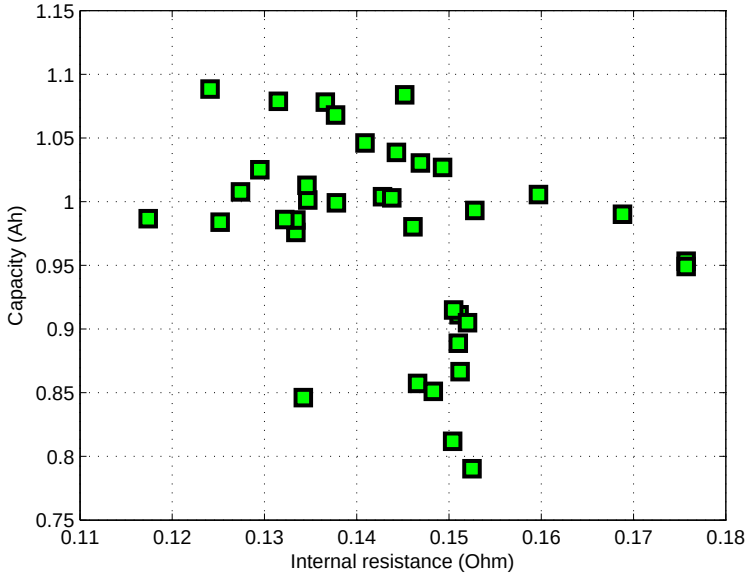

Figure 6.1: Capacity and resistance distribution of the test cells.

hundreds of cycles of aging tests, as described in Chapter II. The distribution of the cell capacity and resistance of the inventory is plotted in Fig. 6.1. One can see that the cells have capacities varying from 1.1Ah to 0.8Ah, and internal resistance varying from 0.12Ohm to 0.17Ohm. Battery modules with distinctive cell combinations are built from this inventory for the study. The values of the physical parameters are used as a reference to the model simulation analysis in 6.2.

6.1.1 Influence of Cell Non-uniformity in Applying ICA to Battery Modules

The applicability of ICA to battery modules is first explored using a quick analytical analysis. To simplify the analysis, let's consider the simple model,

$$\begin{aligned} V_k &= OCV_k + R_0 I_k, \\ Q_{k+1} &= Q_k + I_k \Delta t \end{aligned} \tag{6.1}$$

where V_k, I_k, Q_k are the voltage, current, and the charged capacity at sample time k respectively. R_0 is the battery internal resistance and Δt is the time step. Then for an individual battery cell, the IC curve can be computed as the following when constant charging current is applied,

$$IC_k = \frac{\Delta Q_k}{\Delta OCV_k} = \frac{\Delta Q_k}{\Delta OCV_k + R_0 \Delta I_k} = \frac{\Delta Q_k}{\Delta V_k} \tag{6.2}$$

where $\Delta I_k = 0$ when I_k is a constant current. The IC curve calculated using terminal measurement data ($\frac{\Delta Q_k}{\Delta V_k}$) could well represent the battery characteristics reflected by the OCV-SOC function.

On the other hand, for a battery module with 2 parallel-connected cells, we have,

$$\begin{aligned} \frac{\Delta Q_k}{\Delta V_k} &= \frac{\Delta Q_{1k} + \Delta Q_{2k}}{\Delta V_k} = \frac{\Delta Q_{1k}}{\Delta V_{1k}} + \frac{\Delta Q_{2k}}{\Delta V_{2k}} \\ &= \frac{\Delta Q_{1k}}{\Delta OCV_{1k} + R_{0,1} \Delta I_{1k}} + \frac{\Delta Q_{1k}}{\Delta OCV_{2k} + R_{0,2} \Delta I_{2k}} \\ &\neq \frac{\Delta Q_{1k}}{\Delta OCV_{1k}} + \frac{\Delta Q_{1k}}{\Delta OCV_{2k}} \end{aligned} \tag{6.3}$$

where 1 and 2 in the subscript indicate the cell #1 and #2 in the battery module respectively. I_{1k} and I_{2k} would vary with time even when a constant current is applied to charge the module, due to the uneven current distribution caused by the cell-to-cell variation. In this case, ΔI_{1k} and ΔI_{2k} are no longer zero in the battery module. The $\frac{\Delta Q_k}{\Delta V_k}$ calculation may not capture the aging signature embedded in the battery OCV value. Moreover, because of the uneven charge, the IC peaks for the two cells would appear at different time during the charging process. This could further distort the correlation between the module IC peak value identified from the the measurements of terminal variables of the module, and thereby affecting the estimation of the actual battery module capacity.

The applicability of ICA for module SOH monitoring, therefore, critically relies

on the cell uniformity. In order to understand how the variations in cell current affect the ICA based SOH monitoring framework, simulation analysis are performed using a battery module model in the following section.

6.2 ICA for Battery Module SOH Characterization: Simulation Analysis

The objective of the simulation analysis is to explore how the IC curve of a battery module change with different module capacity and cell non-uniformity. The cell capacity and resistance values would be set to emulate different degree of variation in a battery module.

6.2.1 Battery Module Model

The battery module model is constructed based on the approach proposed in [119], where the modeling method follows the Kirchhoff's circuit laws, as shown in Fig. 6.2 for a 3-cell[1] module system. The single cell behavior is simulated using an equivalent circuit model (ECM). A first-order ECM with one RC circuit can be described as follows [104],

$$V_k = OCV(z_k) - V_{RC,k} + R_0 I_k, \tag{6.4}$$

where

$$\begin{aligned} z_{k+1} &= z_k + (\frac{\eta_i \Delta t}{Q}) I_k, \\ V_{RC,k+1} &= \exp(\frac{-\Delta t}{R_1 C}) V_{RC,k} - R_1[1 - \exp(\frac{-\Delta t}{R_1 C})] I_k, \end{aligned} \tag{6.5}$$

[1]The 3-cell module system is built to emulate the module design of the Chevy Volt.

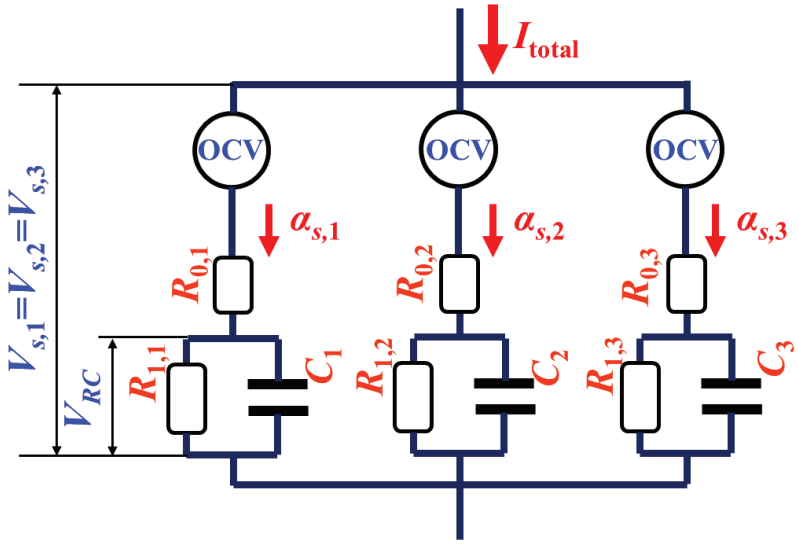

Figure 6.2: Battery module model used for simulations.

z_k is the state of charge (SOC), η_i is the charging/discharging efficiency, Δt is the time step, Q is the battery capacity, I_k is the current, V_k is the terminal voltage, $V_{RC,k}$ is the voltage of the RC circuit, R_0, R_1 and C are battery internal resistance and capacitance.

The OCV function that incorporates the battery aging effects is simulated using the mechanistic battery aging model proposed in [120] . The battery model considers the aging mechanism of both the positive and negative electrodes, and could reflect the qualitative relationship between the equilibrium potentials and battery aging status [114]. The analytic models for the equilibrium potentials of $LiFePO_4$ batteries can be found in literature [115, 116]. The overall equilibrium potential of the battery cell is the difference between the positive electrode and the negative electrode, $V_{\text{total}} = V_{\text{PE}} - V_{\text{NE}}$ (see Fig. 6.3).

As reported in [121, 122], the capacity fading of $LiFePO_4$ cells is dominated by the loss of active lithium. While the degradation of the carbon negative could be observed using destructive structural analysis, it does not affect the cell capacity [121]. Therefore, loss of active lithium is simulated as the main capacity degradation mechanism in our aging analysis.

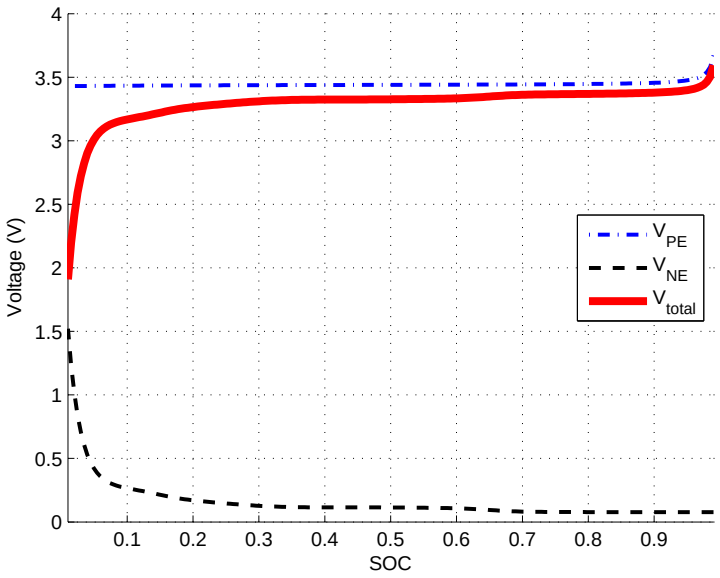

Figure 6.3: Open-circuit-voltage of $LiFePO_4$ batteries simulated using the mechanistic battery aging model.

For a 3-cell module, following the Kirchhoff's laws, the voltages and currents of the parallel connected circuits satisfy:

$$\begin{aligned} V_{s,1} &= V_{s,2} = V_{s,3} \\ \alpha_{s,1} + \alpha_{s,2} + \alpha_{s,3} &= I_{\text{total}} \end{aligned} \tag{6.6}$$

where $V_{s,1}$, $V_{s,2}$, $V_{s,3}$ are the string terminal voltage measurements, and $\alpha_{s,1}$, $\alpha_{s,2}$, $\alpha_{s,3}$ are string currents. I_{total} is the total module current.

The voltage response and current distribution are thereby computed as a solution

Table 6.1: Cell Parameters in Battery Module Simulations

Battery Module	Total Capacity (Ah)	Individual Cell Capacity (Ah), Resistance (Ω)		
#S1	2.85	0.97, 0.13	0.95, 0.13	0.93, 0.13
#S2	2.70	0.92, 0.13	0.90, 0.13	0.88, 0.13
#S3	2.55	0.87, 0.13	0.85, 0.13	0.83, 0.13
#S4	2.85	0.97, 0.12	0.95, 0.13	0.93, 0.14
#S5	2.85	0.97, 0.11	0.95, 0.13	0.93, 0.15

†S represents simulation

of a set of linear equations [119]. The system of linear equations can be described by,

$$\begin{pmatrix} \alpha_{s,1} \\ \alpha_{s,2} \\ \alpha_{s,3} \end{pmatrix} = \begin{pmatrix} R_{0,1} & -R_{0,1} & 0 \\ 0 & R_{0,2} & -R_{0,3} \\ 1 & 1 & 1 \end{pmatrix}^{-1} \begin{pmatrix} \Pi_{s,2} - \Pi_{s,1} \\ \Pi_{s,3} - \Pi_{s,2} \\ I_{\text{total}} \end{pmatrix} \tag{6.7}$$

where

$$\Pi_{s,i} = OCV_{s,i} - V_{RC[s,i]}.$$

where V_{RC} is defined in Eqn. 6.4.

6.2.2 ICA Results of Battery Modules with Parallel Connected Cells

Battery modules with different total capacity and cell non-uniformity (in both capacity and resistance) are simulated using the model described above. The results of five battery modules with different cell combinations are presented here. The three cells in each module are assumed to be connected in parallel as shown in Fig. 6.2. The cell capacities and resistance used in the module simulations are listed in Table 6.1. The internal resistance value represents the sum of R_0 and R_1 for each cell. The range of the capacity and resistance variation is selected based on the parameter values of the test cells (see Fig. 6.1). The correlation between the IC peak values and the capacity of the simulated battery modules are compared as shown in Figs. 6.4 and 6.5.

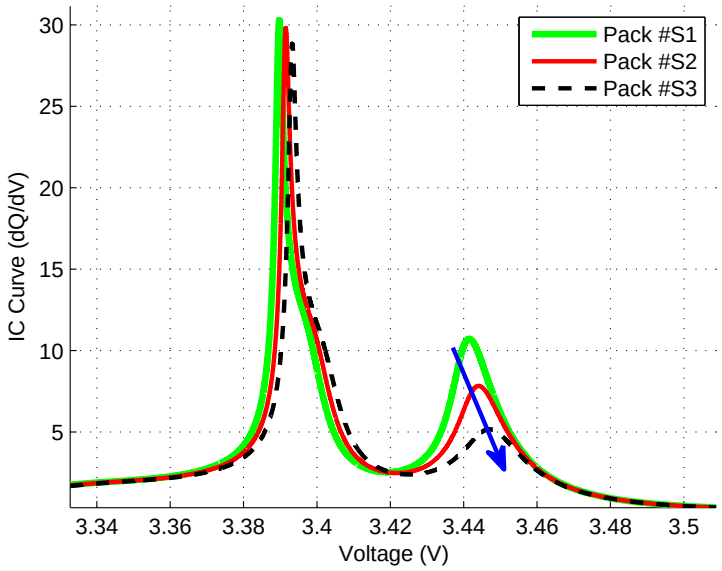

Figure 6.4: ICA results of battery modules simulated (#S1, #S2, #S3) with variation in cell and total capacity.

The ICA results of battery modules #S1, #S2 and #S3 are shown in Fig. 6.4. The three simulated modules have variation in both cell and total capacities but not in resistance. As marked by the arrow in Fig. 6.4, the value of second IC peak reduces as the module capacity degrades, which is consistent with the single cell results. The influence of cell non-uniformity in cell capacity is rather small and inconsequential. Therefore, without resistance variation, the ICA based capacity estimation is directly applicable to battery modules.

The sensitivity of the module IC peak values to cell non-uniformity in resistance is also investigated. Although the resistance change does not affect the ICA results for single cells, the difference between cells could be large and might affect the module ICA results because they could affect the current distribution. For the case studies, variations of 0.01Ω (Module #S4) and 0.02Ω (Module #S5) are simulated and the results are shown in Fig. 6.5. It is observed that, when the variation of internal resistance increases, the IC peaks tend to decrease.

To better understand the quantitative relationship between the cell variation and

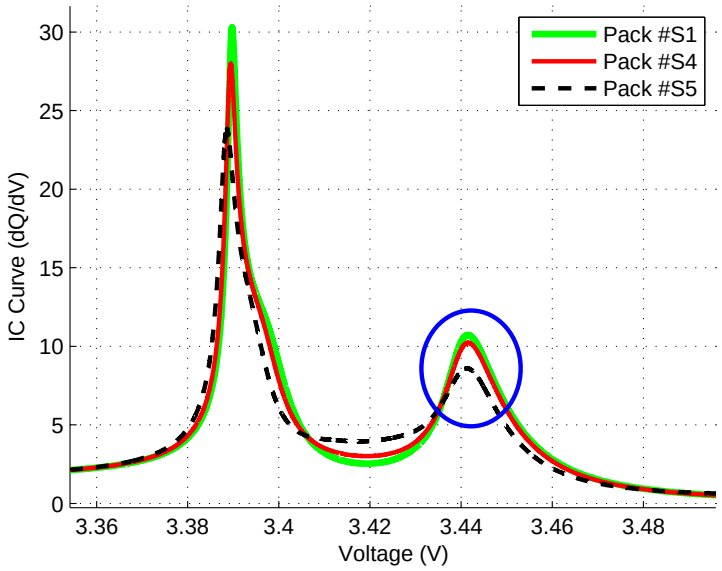

Figure 6.5: ICA results of battery modules (#S1, #S4, #S5) simulated with variation in cell resistance.

the deviations in the IC peak values, extensive simulations are performed with battery modules that have parallel-connected cells. For the convenience of visualization, 2 instead of 3 cells are included in each simulated module. Regardless of the cell numbers, the simulation results should reflect the relationship between the accuracy of ICA with respect to cell capacity and resistance variation in a module. In this part of the study, the reference module which has two identical cells is used as the benchmark, whereas the modules made up of two cells with varied capacity and resistance are used to reflect the non-uniformity. The simulated modules have the same total capacity as the reference module.

We consider the variation in the IC peak by comparing,

$$\Delta IC = \frac{IC_{ref} - IC_{var}}{IC_{ref}} \tag{6.8}$$

where IC_{ref} and IC_{var} are the IC peak values of the reference module and the modules with varied cell non-uniformity respectively.

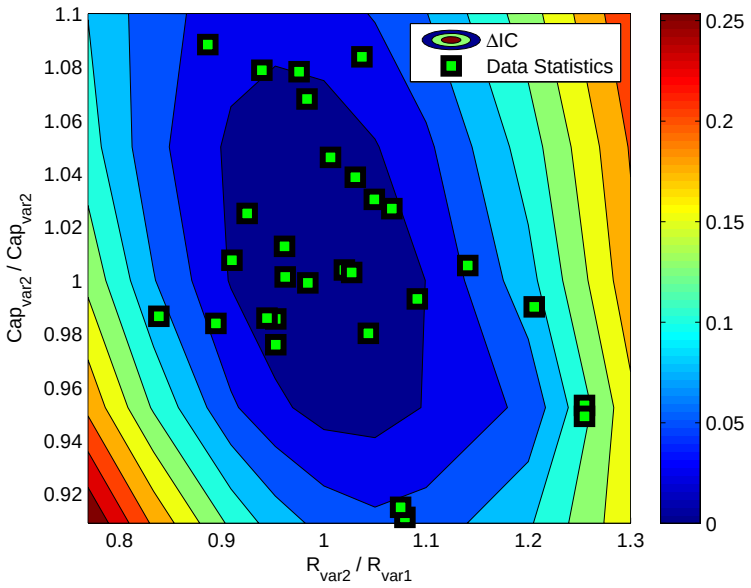

Figure 6.6: ICA results simulated using a 2-cell battery module with capacity and resistance variation.

The results are shown in Fig. 6.6, where Cap_{var} and R_{var} are the capacities and resistance of the cells in the modules with variation. The color code corresponds to the value of ΔIC as specified by the side bar in the figure. The x and y axes represent the variations in resistance ($\pm 30\%$) and capacity ($\pm 10\%$) respectively among the two cells in the module. The contour map shows that the deviation in IC peak value could be up to 25% in the worst case. However, most of the changes in the battery module follow the pattern that increase in resistance is accompanied by the decrease in capacity. Therefore most of non-uniform distributions are expected to fall within the neighborhood of the the diagonal stripe (from the upper-left to the lower-right), and unlikely to fall into the two corners (upper-right and lower-left) of Fig. 7, where the value of ΔIC is high. This is confirmed by experimental results. By plotting our actual battery data onto the map, one can see that the range of deviation could be reduced to 10%, which is equivalent to 2% error in capacity estimation.

The simulation results imply that the ICA based SOH monitoring framework developed for single cells could also be used for battery modules. The design of the

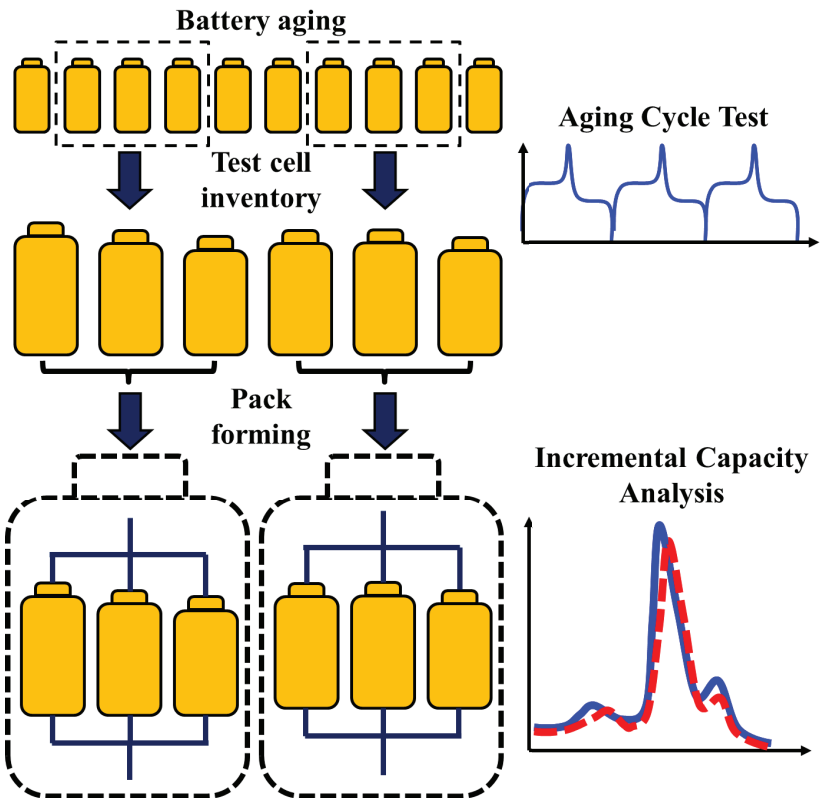

Figure 6.7: Design of the experimental battery module test.

validation test is presented in the next section.

6.3 Experimental Setup

The test data used for this study are acquired through the battery test bench set up in [81], which includes an Arbin BT2000 tester, a thermal chamber for environment control, a computer for user-machine interface and data storage, a switch board for cable connection, and battery cells. The data acquisition system has a sampling frequency of 10Hz.

Battery modules in experiment are formed by selecting aged cells from our test cell inventory and connecting them in parallel (see Fig. 6.7, for the case of 3-cell modules). In this work, total of about 30 modules were tested with most of the modules having 3 cells and others having 7. The characteristics of the 3-cell modules

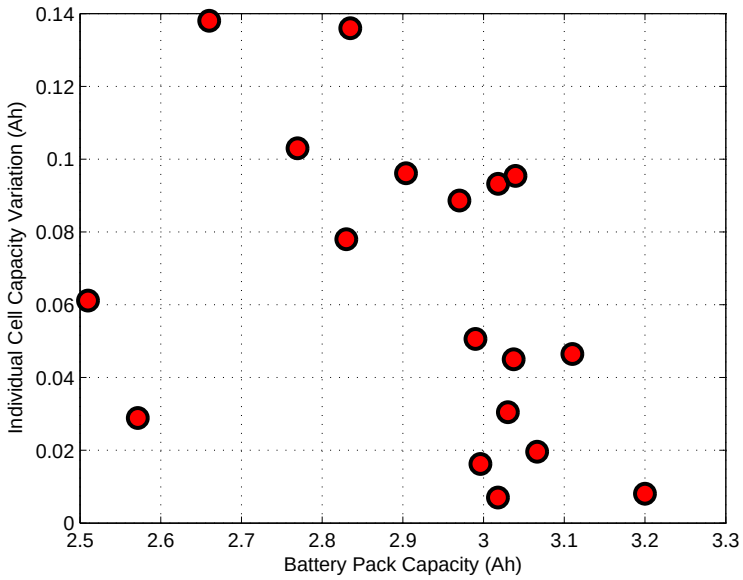

Figure 6.8: Characteristics of tested battery modules with 3 cells.

are shown in Fig. 6.8, where the variation of individual cell capacity in a module is quantified using the standard deviation. One can see that the modules cover a wide range of capacity variations (2.5Ah to 3.2Ah) and have different uniformity. Some modules are made up of cells with similar aging status, while others have capacity variation up to 0.14Ah (more than 10% of the nominal capacity).

All tests are conducted at 24^{o}C. ICA is performed on the data to obtain the relationship between the IC curve and the battery degradation.

6.4 ICA for Battery Module SOH Monitoring with Experimental Results

The IC curves of the battery modules cannot be computed directly from numerical derivative or parametric curve fitting due to the measurement noise. Instead, the IC curves are computed using partial charging data with specialized processing algorithm such as the support vector regression (SVR) algorithm [16, 123].

Take each charging data set with current and voltage measurements, let $x = q$,

$y = v$ be the input and output of the SVR model (q represents the battery charged capacity, v is the measured voltage). The SVR model for the V-Q curve can be expressed as,

$$y = \sum_{i=1}^{N} \beta_i \mathcal{K}(x_i, x) + \mu, \tag{6.9}$$

where N is the number of data points in the data set, β_is and μ are the model parameters, whose values are determined based on the data set, and $\mathcal{K}(\cdot, \cdot)$ is the selected kernel. In this study, the Gaussian radial basis function (rbf) kernel is used and is expressed as

$$\mathcal{K}(x, x') = \exp(\frac{-\|x - x'\|^2}{2\sigma^2}) \tag{6.10}$$

where σ is the adjustable parameter for the kernel function.

By solving a linear programming based optimization problem, the parameters in model (6.9) can be determined and the model can be reduced to

$$f(x) = \sum_{i=1}^{N_{sv}} \beta_i \mathcal{K}(sv_i, x) + \mu, \tag{6.11}$$

where sv is the support vector (SV) and N_{sv} is the total number of SVs ($N_{sv} \ll N$). Then, the IC curve can be computed from the fitted V-Q curve as follows:

$$\frac{dQ}{dV} = \frac{1}{f'(x)} = \frac{1}{\sum_{i=1}^{N_{sv}} \beta_i \mathcal{K}'(sv_i, x)}. \tag{6.12}$$

As an example, Fig. 6.9 shows the IC curve of a 3-cell module identified through the SVR algorithm. More detailed discussion on the SVR approach for IC curve identification can be found in [123].

Fig. 6.10 shows the ICA results of three 3-cell battery modules. The specifications

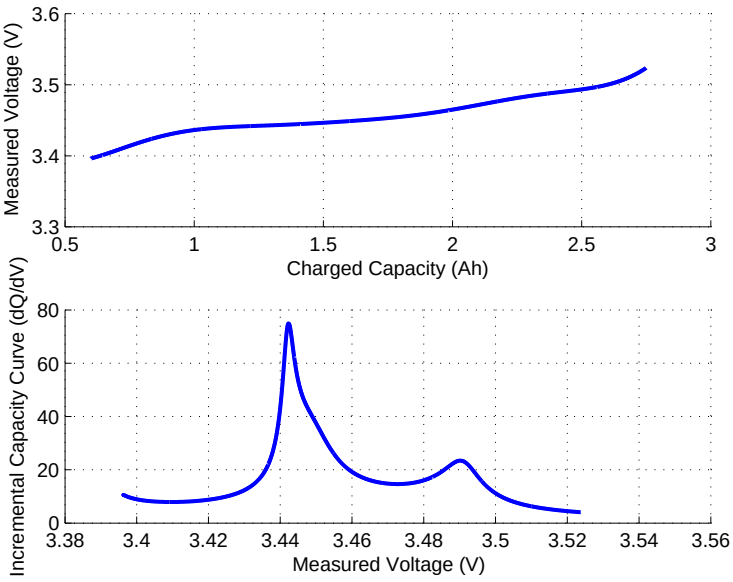

Figure 6.9: Computing IC curves from battery charging data using SVR algorithm.

Table 6.2: Cell Parameters in Battery Module Tests

Battery Module	Total Capacity (Ah)	Individual Cell Capacity (Ah)			Cell Variation (Ah)
#T1	3.2005	1.0838	1.068	1.0788	0.008
#T2	3.1030	0.9866	1.0782	1.0461	0.046
#T3	3.0179	1.0039	0.9991	0.9901	0.007
#T4	3.0373	1.0251	1.0059	1.0076	0.011
#T5	3.0396	1.0838	1.0680	0.9112	0.095

[†]T represents test

of those modules with 3 aged cells are listed in Table 6.2. As expected, the IC curves extracted from the test data show a clear aging trend. The second IC peak (circled in Fig. 6.10) values decreases as module capacity reduces.

6.4.1 Results of Module ICA Study

As in the single cell case [16], we may record the value of the second IC peak and use that as a signature of battery capacity fading. In order to see the robustness of the ICA based capacity estimation method, two battery modules with same total capacity but different individual cell capacities are compared in Fig. 6.11. The characteristics

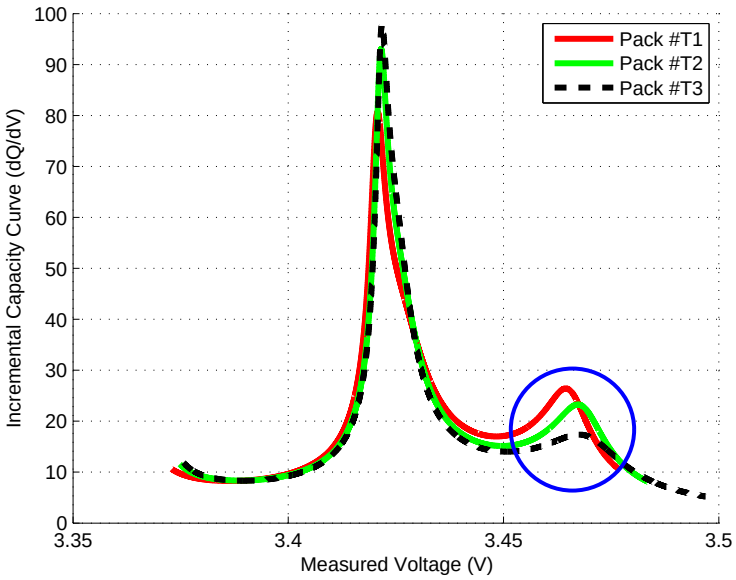

Figure 6.10: ICA results of 3-cell battery modules.

of the two modules are listed in Table 6.2. The collective capacity is the total module capacity measured through Coulomb counting. One might notice that the collective module capacity does not equal to the algebraic sum of the individual capacities. This can be caused by two reasons. First, there is a time gap between the cell tests and module tests so that the individual cell properties could have changed. Second, the current distribution during charging/discharging would be uneven in the module when cell non-uniformity exists, thereby affecting the usable capacity of the module. For the module capacity estimation, we use the value of the collective capacity.

As shown in Fig. 6.11, although the IC peak locations are different due to the difference in resistance, the second IC peak values of the two packs are almost identical. Therefore the second IC peak value seems to be a robust aging signature for $LiFePO_4$ battery modules.

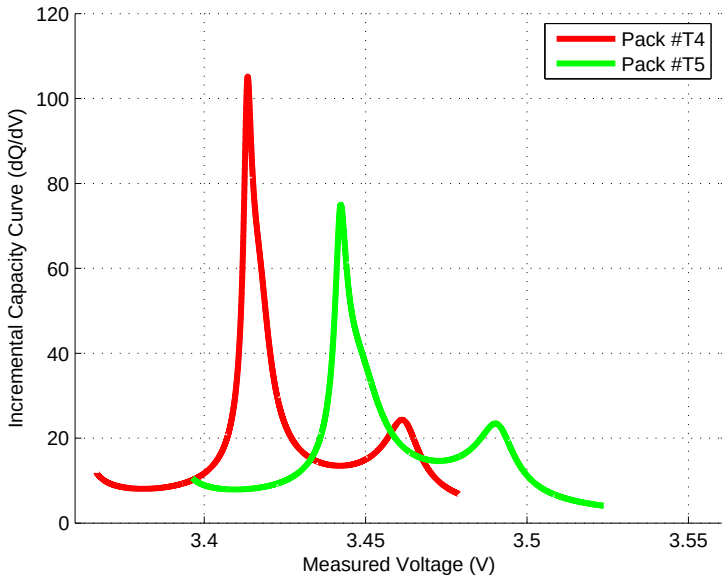

Figure 6.11: IC curves of battery modules with same total capacity but different cell capacities.

Table 6.3: Battery Capacity Estimation

# of Cells	1	3	7
RMSE (%)	1.62	1.28	1.55

6.4.2 Battery Module Capacity Estimation Model

To quantify the correlation between capacity and the corresponding IC peak values, a fitted curve (dashed line in Fig. 6.12) is obtained using only the single cell test data. The quantitative correlation could provide us a tool to estimate the battery capacity based on the IC peak values identified from the test data. To validate this estimation method with battery module data, normalization is performed first. Both capacity and IC peak values obtained from the data are divided by the nominal capacity values (e.g., 3-cell module data are divided by 3.3Ah, the total capacity of three fresh normal cells). After normalization, we could plot the ICA results of single cells and modules on the same figure, as shown in Fig. 6.12. The maximum deviation between fitted correlation and the battery module data is about 2%. The accuracy of the battery capacity estimation is shown in Table 6.3. One can see that, although

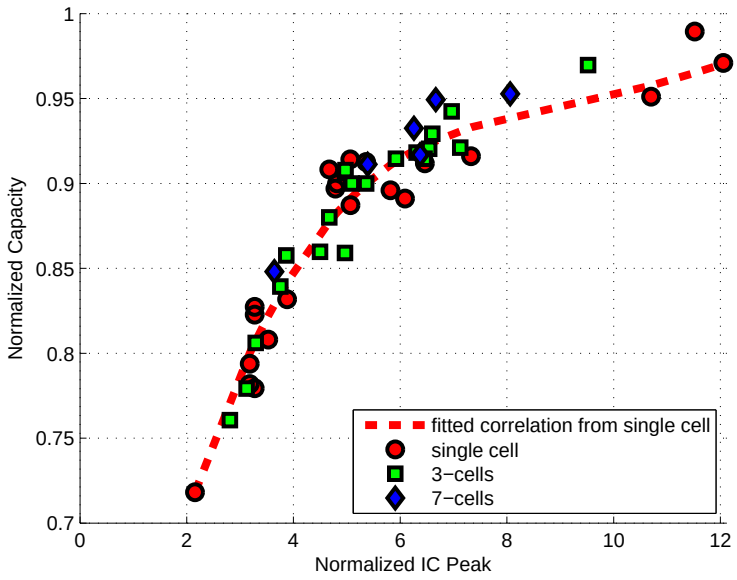

Figure 6.12: ICA based battery capacity estimation.

the estimation model is built based on the single cell data, the estimation error does not increase when the it is applied to 3-cell and 7-cell module data. This result implies that, the correlation identified using single cell data is generalizable to battery modules with various number of cells, and could be used as a battery degradation model for capacity estimation.

CHAPTER VII

Conclusions and Future Work

7.1 Conclusions

The main results of the dissertation can be summarized as follows:

- A new OCV parametric model is proposed for on-board battery energy management. The special parametrization considers the staging phenomenon during the lithium intercalation/deintercalation process for lithium-ion batteries, therefore leading to a much better fitting accuracy when applied to experimental battery OCV data. The new parametric model is applied, together with an EKF, to SOC estimation and its effectiveness is demonstrated on FUDS cycle data. We also show that the parametric model can be applied for ICA based SOH monitoring. Through comparisons of IC curves, the model is shown to be capable of reflecting battery cell's electrochemical properties at different operating temperature conditions and aging stages. Moreover, through parametric analysis, we are able to simplify the model structure and develop a function that characterizes the relations between the model parameters and the degradation of battery performance, which enables us to monitor battery SOH and estimate capacity fading only based on the model parameters.

- The battery SOH monitoring problem with a specific emphasis on using partial

vehicle charging data for on-board implementation is studied. ICA is used to correlate capacity fading with the IC curve peaks, thereby rendering the latter as the robust signature for SOH monitoring. Several algorithms are developed to extract this signature from normal vehicle charging data. Using SVR, an SOH monitoring framework is developed to provide a definite and quantitative correlation between IC peaks and faded battery capacity. The capacity loss can thereby be estimated/predicted through normal charging data during real-life operation. For data collected on 8 $LiFePO_4$ cells, the model developed with the SVR approach using one cell data is able to predict the capacity fading of other cells with less than 1% absolute error except a few outliers.

- The parametric model structure identified by the SVR algorithm is exploited for real-time battery system characterization, and a framework for lithium ion battery SOH monitoring is proposed. In order to investigate the sensitivity of the parametric structure to battery voltage data variation, a parametric LP problem is formulated. The voltage variation is characterized through simulations using mechanistic battery aging model and verified using battery test data. The parametric LP is solved by Monte Carlo simulations. Because of the data characteristics, the SVs in the V-Q curve model of $LiFePO_4$ battery do not change even when the battery cells age or vary. A model parametrization based on the SV invariance is thereby established. The resulting linear parametric model can be directly implemented in on-board BMS for SOH monitoring.

- The ICA based SOH monitoring framework is further extended from single cells to battery packs. The applicability of the framework to battery pack is first investigated through model simulation and then validated using experimental data. A battery inventory that consists of 24 $LiFePO_4$ cells with various aging conditions is established, and the test cells are combined into battery packs

for the study. The results show that, the total capacity loss of a battery pack could also be correlated with the IC curve peaks, and the correlation is the same as the single cell case. The findings suggest that the ICA based SOH monitoring framework developed for single cells can be applied to battery packs with various series-parallel configurations.

7.2 Future Work

The work presented in this dissertation motivates many new research opportunities and could be mainly extended in two directions: generalization of the model parametrization and adaptation framework, and development of optimal energy management strategies for applications that involve energy storage systems.

Since most of my efforts have been dedicated to developing effective and robust system identification algorithms for battery state monitoring, the research on developing optimal energy management strategies could be focused on the following topics:

- **Develop simulation tools that integrate battery degradation model with the main system model for SOH management:** the objective of optimal energy management strategies is usually to maximize system energy efficiency. However, in the long term operation, the cost of battery maintenance or replacement could also affect the economic performance of the system. By integrating the battery SOH information identified on-board with a validated degradation model, both the system operations and the battery health conditions could be considered in the problem formulation. Adaptive load control strategies could thereby be developed to not only optimize the overall system efficiency, but also to mitigate aging effects and extend battery life.

- **Study effects of the electrical loads generated by the optimized battery management strategies on the grid:** the collective effects of the charg-

ing/discharging strategies could affect the electric grid significantly. An appropriate mathematical optimization problem could be formulated to coordinate those charging operations with the objective of maximizing system performance while maintaining reliable and safe grid operation.

- **Design model-based predictive energy management strategies with real-time system identification for off-grid operations:** the system identification algorithms previously designed for the battery systems could be extended to other components in the applications. By updating the system status in real-time, the on-board energy management strategies could be further optimized to achieve better performance. For instance, in the case of model predictive control based optimal energy management design, the model parameters could be constantly updated to ensure prediction accuracy.

On the other hand, the model parametrization and adaptation could be further explored in the following ways:

- **Investigate the general conditions for the invariance of SVs in SVM based learning or regression problems that have varying data characteristics:** The invariant properties of the SVs shown in the battery SOH monitoring allows to eliminate the iterative optimization process from the SVR problem. The conditions for invariance was found for the battery aging data using a Monte Carlo simulation based approach, but general conditions has not been established. Future work may be devoted to finding such conditions through solving a parametric programming problem.

- **Apply the modeling framework to other systems or applications that share similar properties to the battery SOH monitoring problem:** The simple SVR representation provides a natural choice of parametric model for on-board adaptation. By exploring existing engineering applications that have

similar aging or time varying characteristics as the batteries, the effectiveness and capability of generalization of the developed modeling framework could be verified.

BIBLIOGRAPHY

BIBLIOGRAPHY

[1] S. Chu and A. Majumdar. Opportunities and challenges for a sustainable energy future. *Nature*, 488(7411):294–303, 2012.

[2] World Energy Outlook 2014. Technical report, Internation Energ Agency, Paris, France, 2014.

[3] M. Safari and C. Delacourt. Modeling of a commercial graphite/$LiFePO_4$ cell. *J. Electrochem. Soc.*, 158(5):A562–A571, 2011.

[4] M. Armand and J.-M. Tarascon. Building better batteries. *Nature*, 451:652–657, 2008.

[5] M. S. Dresselhaus and I. L. Thomas. Alternative energy technologies. *Nature*, 414(6861):332–337, 2001.

[6] S. M. Schoenung and W. V. Hassenzahl. Long- vs. short-term energy storage technologies analysis: A life-cycle cost study. Technical Report SAND2003-2783, Sandia National Labortories, Albuquerque, NM and Livermore, CA, August 2003.

[7] B. Dunn, H. Kamath, and J.-M. Tarascon. Electrical energy storage for the grid: A battery of choices. *Science*, 6058:928–935, November 2011.

[8] M. Grünig, M. Witte, D. Marcellino, J. Selig, and H. van Essen. An overview of electric vehicles on the market and in development. Technical report, Delft, CE Delft, April 2011.

[9] P. Mock, S. A. Schmid, and H. E. Friedrich. Market prospects of electric passenger vehicles. In Gianfranco Pistoia, editor, *Electric and Hybrid Vehicles: Power Sources, Models, Sustainability, Infrastructure and the Market*. Elsevier, 2010.

[10] H. D. Abruña, Y. Kiya, and J. C. Henderson. Batteries and electrochemical capacitors. *Phys. Today*, 61(12):43–47, 2008.

[11] C. D. Rahn and C.-Y. Wang. *Battery Systems Engineering*. John Wiley & Sons Ltd, Oxford, UK, 2013.

[12] B. Y. Liaw and M. Dubarry. A roadmap to understand battery performance in electric and hybrid vehicle operation. In Gianfranco Pistoia, editor, *Electric and Hybrid Vehicles: Power Sources, Models, Sustainability, Infrastructure and the Market*. Elsevier, 2010.

[13] N. A. Chaturvedi, R. Klein, J. Christensen, J. Ahmed, and A. Kojic. Algorithms for advanced battery-management systems. *IEEE Control Syst. Mag.*, 30(3):49–68, June 2010.

[14] W. Waag, C. Fleischer, and D. U. Sauer. Critical review of the methods for monitoring of lithium-ion batteries in electric and hybrid vehicles. *J. Power Sources*, 258:321–339, 2014.

[15] V. Pop, H. Jan Bergveld, D. Danilov, P. P. L. Regtien, and P. H. L. Notten. *Battery Management Systems: Accurate State-of-Charge Indication for Battery-Powered Applications*. Springer, 1st edition, 2008.

[16] C. Weng, Y. Cui, J. Sun, and H. Peng. On-board state of health monitoring of lithium-ion batteries using incremental capacity analysis with support vector regression. *J. Power Sources*, 235:36–44, 2013.

[17] J. Vetter, P. Novák, M.R. Wagner, C. Veit, K.-C. Möller, J.O. Besenhard, M. Winter, M. Wohlfahrt-Mehrens, C. Vogler, and A. Hammouched. Ageing mechanisms in lithium-ion batteries. *J. Power Sources*, 147:269–281, 2005.

[18] S. J. Moura. *Techniques for battery health conscious power management via electrochemical modeling and optimal control*. PhD thesis, University of Michigan, 2011.

[19] S. Piller, M. Perrin, and A. Jossen. Methods for state-of-charge determination and their applications. *J. Power Sources*, 96:113–120, 2001.

[20] S. Santhanagopalan and R. E. White. Online estimation of the state of charge of a lithium ion cell. *J. Power Sources*, 161:1346–1355, 2006.

[21] M. Verbrugge and E. Tate. Adaptive state of charge algorithm for nickel metal hydride batteries including hysteresis phenomena. *J. Power Sources*, 126:236–249, 2004.

[22] G. L. Plett. Extended kalman filtering for battery management systems of LiPB-based hev battery packs, part 1. background. *J. Power Sources*, 134:252–261, 2004.

[23] G. L. Plett. Extended kalman filtering for battery management systems of LiPB-based hev battery packs, part 2. modeling and identification. *J. Power Sources*, 134:262–276, 2004.

[24] G. L. Plett. Extended kalman filtering for battery management systems of LiPB-based hev battery packs, part 3. state and parameter estimation. *J. Power Sources*, 134:277–292, 2004.

[25] U. Tröltzsch, O. Kanoun, and H.-R. Tränkler. Characterizing aging effects of lithium ion batteries by impedance spectroscopy. *Electrochim. Acta*, 51:1664–1672, 2006.

[26] A. Eddahech, O. Briat, N. Bertrand, J.-Y. Delútage, and J.-M. Vinassa. Behavior and state-of-health monitoring of li-ion batteries using impedance spectroscopy and recurrent neural networks. *Int. J. Elec. Power*, 42:487–494, 2012.

[27] M. A. Roscher, O. S. Bohlen, and D. U. Sauer. Reliable state estimation of multicell lithium-ion battery systems. *IEEE Trans. Energy Convers.*, 26(3):737–743, Sept 2011.

[28] J. Kim and B. H. Cho. State-of-charge estimation and state-of-health prediction of a Li-ion degraded battery based on an ekf combined with a per-unit system. *IEEE Trans. Veh. Technol.*, 60(9):4249–4260, 2011.

[29] J. Remmlinger, M. Buchholz, M. Meiler, P. Bernreuter, and K. Dietmayer. State-of-health monitoring of lithium-ion batteries in electric vehicles by on-board internal resistance estimation. *J. Power Sources*, 196:5357–5363, 2011.

[30] X. Hu, F. Sun, Y. Zou, and H. Peng. Online estimation of an electric vehicle lithium-ion battery using recursive least squares with forgetting. In *Proc. Am. Control Conf. 2011*, San Francisco, CA, June 2011.

[31] M. A. Roscher, J. Assfalg, and O. S. Bohlen. Detection of utilizable capacity deterioration in battery systems. *IEEE Trans. Veh. Technol.*, 60(1):98–103, 2011.

[32] J. Groot. State-of-health estimation of li-ion batteries: Cycle life test methods. Master's thesis, Chalmers University of Technology, 2012.

[33] M. A. Roscher and D. U. Sauer. Dynamic electric behavior and open-circuit-voltage modeling of $LiFePO_4$-based lithium ion secondary batteries. *J. Power Sources*, 196(1):331–336, 2011.

[34] A. Farmann, W. Waag, A. Marongiu, and D. U. Sauer. Critical review of on-board capacity estimation techniques for lithium-ion batteries in electric and hybrid electric vehicles. *J. Power Sources*, 281:114–130, 2015.

[35] M. Dubarry, V. Svoboda, R. Hwu, and B. Y. Liaw. Incremental capacity analysis and close-to-equilibrium OCV measurements to quantify capacity fade in commercial rechargeable lithium batteries. *Electrochem. Solid St.*, 9(10):A454–A457, 2006.

[36] M. Dubarry and B. Y. Liaw. Identify capacity fading mechanism in a commercial lifepo$_4$ cell. *J. Power Sources*, 194:541–549, 2009.

[37] K. Honkuraa, H. Honboa, Y. Koishikawab, and T. Horibab. State analysis of lithium-ion batteries using discharge curves. *ECS Tran.*, 13(19):61–73, 2008.

[38] K. Honkuraa, K. Takahashia, and T. Horibab. Capacity-fading prediction of lithium-ion batteries based on discharge curves analysis. *J. Power Sources*, 196(23):10141–10147, 2011.

[39] A. Smith. *A High Precision Study of Li-ion Batteries*. PhD thesis, Dalhousie University, 2012.

[40] M. Dubarry, B. Y. Liaw, M.-S. Chen, S.-S. Chyan, K.-C. Han, W.-T. Sie, and S.-H. Wu. Identifying battery aging mechanisms in large format li ion cells. *J. Power Sources*, 196(7):3420–3425, 2011.

[41] A. Barré, B. Deguilhem, S. Grolleau, M. Gérard, F. Suard, and D. Riu. A review on lithium-ion battery ageing mechanisms and estimations for automotive applications. *J. Power Sources*, 241:680–689, 2013.

[42] M. B. Pinson and M. Z. Bazant. Theory of sei formation in rechargeable batteries: capacity fade, accelerated aging and lifetime prediction. *J. Electrochem. Soc.*, 160(2):A243–A250, 2013.

[43] M. Broussely, Ph. Biensan, F. Bonhomme, Ph. Blanchard, S. Herreyre, K. Nechev, and R. J. Staniewicz. Main aging mechanisms in li ion batteries. *J. Power Sources*, 146(1):90–96, 2005.

[44] P. Arora, R. E. White, and M. Doyle. Capacity fade mechanisms and side reactions in lithium-ion batteries. *J. Electrochem. Soc.*, 145(10):3647–3667, 1998.

[45] L. S. Kanevskii and V. S. Dubasova. Degradation of lithium-ion batteries and how to fight it: A review. *Russ. J. Electrochem.*, 41(1):1–16, 2005.

[46] P. Verma, P. Maire, and P. Novákk. A review of the features and analyses of the solid electrolyte interphase in Li-ion batteries. *Electrochim. Acta*, 55(22):6332–6341, 2010.

[47] J. Christensen and J. Newman. A mathematical model for the lithium-ion negative electrode solid electrolyte interphase. *J. Electrochem. Soc.*, 151(11):A1977–A1988, 2004.

[48] S. J. Harris, E. Kabiri Rahani, and V. B. Shenoy. Direct in situ observation and numerical simulations of non-shrinking-core behavior in an mcmb graphite composite electrode. *J. Electrochem. Soc.*, 159(9):A1501–A1507, 2012.

[49] A. H. Zimmerman and M. V. Quinzio. Lithium plating in lithium-ion cells. In *Presented at the NASA Battery Workshop, Huntsville, AL*, 2010.

[50] J. H. Seo, J. Park, G. Plett, and A. M. Sastry. Gas-evolution induced volume fraction changes and their effect on the performance degradation of Li-ion batteries. *Electrochem. Solid. St.*, 13(0):A135–A137, 2010.

[51] M. Ebner, F. Marone, M. Stampanoni, and V. Wood. Visualization and quantification of electrochemical and mechanical degradation in li ion batteries. *Science*, 342(6159):716–720, 2013.

[52] D. Wang, X. Wu, Z. Wang, and L. Chen. Cracking causing cyclic instability of $LiFePO_4$ cathode material. *J. Power Sources*, 140(1):125128, 2005.

[53] P. Barai and P. P. Mukherjee. Characterization of mechanical degradation in lithium ion battery electrodes. In *ECS Meeting Abstracts*. The Electrochemical Society, 2014.

[54] Y. Hu, X. Zhao, and Z. Suo. Averting cracks caused by insertion reaction in lithiumion batteries. *J. Mater. Res.*, 25(6):1007–1010, 2010.

[55] M. Doyle, T. F. Fuller, and J. Newman. Modeling of galvanostatic charge and discharge of the lithium/polymer/insertion cell. *J. Electrochem. Soc.*, 140(6):1526–1533, 1993.

[56] P. Ramadass, B. Haran, P. M. Gomadam, R. White, and B. N. Popov. Development of first principles capacity fade model for li-ion cells. *J. Electrochem. Soc.*, 151(2):A196–A203, 2004.

[57] E. Meissner and G. Richter. Battery monitoring and electrical energy management precondition for future vehicle electric power systems. *J. Power Sources*, 116:79–98, 2003.

[58] F. Sun, X. Hu, Y. Zou, and S. Li. Adaptive unscented kalman filtering for state of charge estimation of a lithium-ion battery for electric vehicles. *Energ.*, 36(5):3531–3540, 2011.

[59] M. Sheikhan, R. Pardis, and D. Gharavian. State of charge neural computational models for high energy density batteries in electric vehicles. *Neural Comput. and Appl.*, 22(6):1171–1180, 2013.

[60] W.X. Shen, K.T. Chau, C.C. Chan, and E.W.C. Lo. Neural network-based residual capacity indicator for nickel-metal hydride batteries in electric vehicles. *IEEE Trans. Veh. Technol.*, 54(5):1705–1712, 2005.

[61] P. Singh, R. Vinjamuri, X. Wang, and D. Reisner. Design and implementation of a fuzzy logic-based state-of-charge meter for li-ion batteries used in portable defibrillators. *J. Power Sources*, 162(2):829–836, 2006.

[62] A. J Salkind, C. Fennie, P. Singh, T. Atwater, and D. E. Reisner. Determination of state-of-charge and state-of-health of batteries by fuzzy logic methodology. *J. Power Sources*, 80(12):293–300, 1999.

[63] S. M. Rezvanizaniani, Z. Liu, Y. Chen, and J. Lee. Review and recent advances in battery health monitoring and prognostics technologies for electric vehicle (ev) safety and mobility. *J. Power Sources*, 256:110–124, 2014.

[64] S. T. Revankar and P. Majumdar. *Fuel Cells: Principles, Design, and Analysis*. Mechanical and Aerospace Engineering Series. Taylor & Francis, 2014.

[65] P. Ioannou and J. Sun. *Robust adaptive control*. Prentice Hall, 1996.

[66] A. Sciarretta and L. Guzzella. Control of hybrid electric vehicles. *IEEE Control Syst. Mag.*, 30(2):60–70, 2007.

[67] A. Sciarretta, M. Back, , and L. Guzzella. Optimal control of parallel hybrid electric vehicles. *IEEE Trans. Veh. Technol.*, 12:352–363, 2004.

[68] C.-C. Lin, H. Peng, J. Grizzle, and J.-M. Kang. Power management strategy for a parallel hybrid electric truck. *IEEE Trans. Control Syst. Technol.*, 11:839–849, 2003.

[69] C.-C. Lin, H. Peng, , and J. W. Grizzle. A stochastic control strategy for hybrid electric vehicle. In *Proc. Am. Control Conf. 2004*, pages 4710–4715, Boston, MA, 2004.

[70] H. A. Borhan, A. Vahidi, A. M. Phillips, M. L. Kuang, and I. V. Kolmanovsky. Predictive energy management of a power-split hybrid electric vehicle. In *Proc. Am. Control Conf. 2009*, St. Louis, MO, 2009.

[71] C. Weng, Y. Wang, V. Tsourapas, C. Patil, and J. Sun. Optimal control of hybrid electric vehicles with power split and torque split strategies: A comparative case study. In *Proc. Am. Control Conf. 2011*, pages 2131–2136, San Francisco, CA, 2011.

[72] R. Yazami and Ph. Touzain. A reversible graphite-lithium negative electrode for electrochemical generators. *J. Power Sources*, 9:365–371, 1983.

[73] J. R. Dahn. Phase diagram of Li_xC_6. *Phys. Rev.*, B44:9170–9177, 1991.

[74] R. Yazami and Y. Reynier. Thermodynamics and crystal structure anomalies in lithium-intercalated graphite. *J. Power Sources*, 153:312–318, 2006.

[75] X. Feng, J. Li, M. Ouyang, L. Lu, J. Li, and X. He. Using probability density function to evaluate the state of health of lithium-ion batteries. *J. Power Sources*, 232:209–218, 2013.

[76] X. Han, M. Ouyang, L. Lu, J. Li, Y. Zheng, and Z. Li. A comparative study of commercial lithium ion battery cycle life in electrical vehicle: Aging mechanism identification. *J. Power Sources*, 251:38–54, 2014.

[77] A. J. Smith and J. R. Dahn. Delta differential capacity analysis. *J. Electrochem. Soc.*, 159(3):A290–A293, 2012.

[78] I. Bloom, A. N. Jansen, D.P. Abraham, J. Knuth, S. A. Jones, V. S. Battaglia, and G. L. Henriksen. Differential voltage analyses of high-power, lithium-ion cells 1. technique and application. *J. Power Sources*, 139:295–303, 2005.

[79] C. Weng, J. Sun, and H. Peng. A unified open-circuit-voltage model of lithium-ion batteries for state-of-charge estimation and state-of-health monitoring. *J. Power Sources*, 258:228–237, 2014.

[80] C. Weng, J. Sun, and H. Peng. An open-circuit-voltage model of lithium-ion batteries for effective incremental capacity analysis. In *Proc. ASME Dyn. Syst. Control Conf. 2013*, Palo Alto, CA, Oct. 2013.

[81] X. Hu, S. Li, and H. Peng. A comparative study of equivalent circuit models for li-ion batteries. *J. Power Sources*, 198:359–367, 2012.

[82] M. Safari and C. Delacourt. Mathematical modeling of lithium iron phosphate electrode: Galvanostatic charge/discharge and path dependence. *J. Electrochem. Soc.*, 158(2):A63–A73, 2011.

[83] A. J. Smola and B. Schölkopf. A tutorial on support vector regression. *Stat. Comput.*, 14:199–222, 2004.

[84] H. Drucker, C. J. C. Burges, L. Kaufman, A. Smola, and V. Vapnik. Support vector regression machines. *Adv. Neural Inf. Process. Syst.*, pages 155–161, 1997.

[85] C. Cortes and V. Vapnik. Support-vector networks. *Mach. Learn.*, 20(3):273–297, 1995.

[86] B. E. Boser, I. M. Guyon, and V. N. Vapnik. A training algorithm for optimal margin classifiers. In *Proc. 5th Annu. ACM Workshop on Comput. Learn. Theory*, pages 144–152. ACM Press, 1992.

[87] Y.-J. Lee and O. L. Mangasarian. RSVM: Reduced support vector machines. Technical Report 00-07, Data Mining Inst. Comp. Sci. Dept., Univ. Wisconsin, Madison, WI, July 2000.

[88] B. Schölkopf and A. J. Smola. *Learning with Kernels: Support Vector Machines, Regularization, Optimization, and Beyond*. MIT Press, 1st edition, December 2001.

[89] T. Hofmann, B. Schölkopf, and A. J. Smola. Kernel methods in machine learning. *Ann. Statist.*, 36(4):1171–1220, 2008.

[90] N. Cristianini and J. Shawe-Taylor. *An Introduction to Support Vector Machines and Other Kernel-based Learning Methods*. Cambridge University Press, 1st edition, March 2000.

[91] V. Vapnik and A. Lerner. Pattern recognition using generalized portrait method. *Autom. and Remote Control*, 24:774–780, 1963.

[92] V. N. Vapnik. *The Nature of Statistical Learning Theory*. Springer, NY, 1st edition, 1995.

[93] V. Cherkassky and Y. Ma. Practical selection of SVM parameters and noise estimation for SVM regression. *Neural Networks*, 17(1):113–126, 2004.

[94] A. J. Smola, T. T. Frieß, and B. Schölkopf. Semiparametric support vector and linear programming machines. Technical Report NC2-TR-1998-024, Neural and Computational Learning II, NeuroCOLT2 27150, August 1998.

[95] J. Faust, J. Sun, K. Butts, Z. Lu, and S. Tanaka. Parametrization and adaptation of gasoline engine air system model via linear programming support vector regression. In *Proc. Am. Control Conf. 2012*, pages 1290–1295, 2012.

[96] A. H. Thompson. Electrochemical potential spectroscopy: a new electrochemical measurement. *J. Electrochem. Soc.*, 126(4):608–616, 1979.

[97] J. Barker, M. Y. Saidi, and R. Koksbang. Differential capacity as a spectroscopic probe for the investigation of alkali metal insertion reactions. *Electrochim. Acta*, 41(16):2639–2646, 1996.

[98] Walter Van Schalkwijk and Bruno Scrosati. *Advances in lithium-ion batteries*. Springer Science & Business Media, 1st edition, June 2002.

[99] X. Hu, S. Li, and H. Peng. A comparative study of equivalent circuit models for Li-ion batteries. *J. Power Sources*, 198:359–367, 2012.

[100] Y. Hu, S. Yurkovich, Y. Guezennec, and B.J. Yurkovich. Electro-thermal battery model identification for automotive applications. *J. Power Sources*, 196:449–457, 2011.

[101] D. E. Neumann and S. Lichte. A multi-dimensional battery discharge model with thermal feedback applied to a lithium- ion battery pack. In *NDIA Ground Vehicle Systems Engineering and Technology Symposium*, 2011.

[102] M. Chen and G. A. Rincón-Mora. Accurate electrical battery model capable of predicting runtime and I-V performance. *IEEE Trans. Veh. Technol.*, 21(2):504–511, 2008.

[103] A. Szumanowski and Y. Chang. Battery management system based on battery nonlinear dynamics modeling. *IEEE Trans. Veh. Technol.*, 57(3):1425–1432, 2008.

[104] M. Dubarry, N. Vuillaume, and B. Y. Liaw. From single cell model to battery pack simulation for Li-ion batteries. *J. Power Sources*, 186:500–507, 2009.

[105] Z. Lu, J. Sun, and K. Butts. Linear programming SVR-ARMA$_{2k}$ with application in engine system identification. *IEEE Trans. Autom. Sci. Eng.*, 8(4):846–854, 2011.

[106] Z. Lu, J. Sun, and K. Butts. Linear programming support vector regression with wavelet kernel: A new approach to nonlinear dynamical system identification. *Math. Comput. Simulat.*, 79:2051–2063, 2009.

[107] O. L. Mangasarian and D. R. Musicant. Large scale kernel regression via linear programming. *Mach. Learn.*, 46(1-3):255–269, 2002.

[108] G. Bloch, F. Lauer, G. Colin, and Y. Chamaillard. Support vector regression from simulation data and few experimental samples. *Inform. Sciences*, 178(20):3813–3827, 2008.

[109] D. Bertsimas and J. N. Tsitsiklis. *Introduction to linear optimization*. Athena Scientific, 1997.

[110] A. Gretton, A. Doucet, R. Herbrich, P.J.W. Rayner, and B. Schölkopf. Support vector regression for black-box system identification. In *Proc. 11th IEEE Workshop on Stat. Signal Process.*, pages 341 –344, Singapore, August 2001.

[111] A. Smola, B. Schölkopf, and G. Ratsch. Linear programs for automatic accuracy control in regression. In *Proc. 9th Int. Conf. Artif. Neural Networks*, volume 2, pages 575–580, Edinburgh, UK, September 1999.

[112] J. Bi, K. Bennett, M. Embrechts, C. Breneman, and M. Song. Dimensionality reduction via sparse support vector machines. *J. Mach. Learn. Res.*, 3:1229–1243, March 2003.

[113] I. Adler and R. D. C. Monteiro. A geometric view of parametric linear programming. *Algorithmica*, 8(1-6):161–176, 1992.

[114] M. Dubarry, C. Truchot, and B. Y. Liaw. Synthesize battery degradation modes via a diagnostic and prognostic model. *J. Power Sources*, 219:204–216, 2012.

[115] E. Prada, D. Di Domenico, Y. Creff, J. Bernard, V. Sauvant-Moynot, and F. Huet. A simplified electrochemical and thermal aging model of $LiFePO_4$-graphite Li-ion batteries: Power and capacity fade simulations. *J. Electrochem. Soc.*, 160(4):A616–A628, 2013.

[116] P. Albertus, J. Couts, V. Srinivasan, and J. Newman. A combined model for determining capacity usage and battery size for hybrid and plug-in hybrid electric vehicles. *J. Power Sources*, 183:771–782, 2008.

[117] R. Gogoana, M. B. Pinson, M. Z. Bazant, and S. E. Sarma. Internal resistance matching for parallel-connected lithium-ion cells and impacts on battery pack cycle life. *J. Power Sources*, 252:8–13, 2014.

[118] Y. Zheng, M. Ouyang, L. Lu, J. Li, X. Han, L. Xu, H. Ma, T. A. Dollmeyer, and V. Freyermuth. Cell state-of-charge inconsistency estimation for $LiFePO_4$ battery pack in hybrid electric vehicles using mean-difference model. *Appl. Energ.*, 111(0):571–580, 2013.

[119] B. J. Yurkovich and Y. Guezennec. Lithium ion dynamic battery pack model and simulation for automotive applications. In *Proc. ASME 2009 Dyn. Syst. Control Conf.*, Hollywood, CA, Oct. 2009.

[120] J. Christensen and J. Newman. Cyclable lithium and capacity loss in Li-ion cells. *J. Electrochem. Soc.*, 152:A818–A829, 2005.

[121] P. Liu, J. Wang, J. Hicks-Garner, E. Sherman, S. Soukiazian, M. Verbrugge, H. Tataria, J. Musser, and P. Finamore. Aging mechanisms of $LiFePO_4$ batteries deduced by electrochemical and structural analyses. *J. Electrochem. Soc.*, 157:A499–A507, 2010.

[122] K. Striebel, J. Shim, A. Sierra, H. Yang, X. Song, R. Kostecki, and K. McCarthy. The development of low cost $LiFePO_4$-based high power lithium-ion batteries. *J. Power Sources*, 146:33–38, 2005.

[123] C. Weng, J. Sun, and H. Peng. Model parametrization and adaptation based on the invariance of support vectors with applications to battery state-of-health monitoring. *IEEE Trans. Veh. Technol.*, 64(9):3908–3917, 2015.